Semiclassical approximations beyond the leading order in $\hbar$

Theoretical studies of higher-order $\hbar$ contributions and their influence on experimental transport properties of mesoscopic systems

Dissertation
zur Erlangung des Doktorgrades der Naturwissenschaften
(Dr. rer. nat.)
der naturwissenschaftlichen Fakultät II – Physik
der Universität Regensburg

vorgelegt von
Joachim Blaschke
aus Hof

September 1999

Die Arbeit wurde von Prof. Dr. M. Brack angeleitet.
Das Promotionsgesuch wurde am 27. 9. 1999 eingereicht.
das Kolloquium fand am 12. 11. 1999 statt.

Prüfungsausschuß:	Vorsitzender:	Prof. Dr. W. Wegscheider
	1. Gutachter:	Prof. Dr. M. Brack
	2. Gutachter:	Prof. Dr. U. Rößler
	weiterer Prüfer:	Prof. Dr. V. Braun

Version 1.1 vom 26. 11. 1999
published under http://www.joachim-blaschke.de

Contents

Chapter 1

Introduction

Mesoscopic systems, a rapidly progressing field of physical research in the last two decades, are of increasing technological and commercial interest. Semiclassical approximations, i. e. expansions of quantum mechanical equations to leading order in $\hbar$, are appropriate tools for the theoretical description of these systems in between the microscopic and the macroscopic regime. The validity of these approximations requires higher-order $\hbar$ corrections to be negligible. The influence of higher-order corrections is studied theoretically using model systems, and their contributions are traced down in experimental data on magnetoconductance.

Since the early days of quantum mechanics the question how the wave approach is related to the classical description has not been satisfactorily settled. For nearly one century now physicists work with either the classical or the quantum approach, 'well knowing' in which cases the one or the other theoretical description is appropriate. Although the general belief is that quantum mechanics is the basic theory and that classical behavior corresponds to the limit for large systems[1], this relation has not been rigorously established. The open questions concern on the one hand the properties of the transition region between quantum mechanical and classical behavior, the so-called *mesoscopic* regime. On the other hand the nature of the classical and the quantum measurement process is not completely clear by now.

In the present work, only the first question is considered. Readers interested in more fundamental questions concerning alternative interpretations of quantum mechanics [109], consistent formulations of the measurement process [116, 102], and the problems which arise when the interpretation of the Copenhagen School is applied to macroscopic systems [108, 115] are referred to the literature. In the context of this thesis the standard quantum mechanical description following the Copenhagen interpretation is assumed to be exact for arbitrary system sizes, even on classical length scales.

In recent years the rapid development in nanostructure technology has triggered increasing interests in mesoscopic systems. The most remarkable progress has been achieved in the technology of growing and processing semiconductor heterostructures. These build the basis of two-dimensional electron gases (2DEG). Using advanced lithographic techniques on high-mobility samples it has become feasible to laterally confine the 2DEG on size scales smaller than the phase coherence lengths. In these experiments, quantum interference

[1] Large means in this context large quantum numbers.

effects become relevant. For natural quantum systems like atoms, nuclei or clusters only a few (if any) parameters can be controlled experimentally. The semiconductor nanostructures, in contrast, can be tailored to very specific needs and prepared in virtually arbitrary shapes. This new experimental freedom led to the discovery of a variety of novel, often surprising effects emerging from quantum interference. Among the most prominent are weak localization [88, 94, 90], quantized conductance [99], universal conductance fluctuations [93] and commensurability oscillations [83, 55, 84, 63, 41]. The rapid development in this area and the continued interest from a large community of both theoretical and experimental research groups promises exciting new effects within the next years.

Mesoscopic systems, however, are not only challenging for people in basic research, but they also attract huge commercial interest. This is mainly evoked by the fact that the structures on today's highly integrated semiconductor devices have reached a scale where quantum interference effects are no longer negligible. Future development of memory components and logic devices – which includes further miniaturization – can be achieved following two strategies: The first approach is to choose a geometric design of circuits that strongly suppresses quantum interference effects. This approach allows the vast existing knowledge about conventional chip design to be transferred – at least partially – to the quantum regime. Another, more innovative strategy exploits quantum effects explicitly by the development of a new kind of electronics based on interference. The success of both strategies obviously relies on a detailed understanding of mesoscopic physics.

Therefore, an appropriate theoretical description of mesoscopic systems is strongly desired for basic research as well as for commercial applications. Mesoscopic systems generically include a large number of electrons, so that according to the Pauli principle a huge number of eigenstates of the system have to be determined in a quantum calculation. For this reason quantum calculations are often prohibitive due to the numerical effort involved. Much of the detailed interference information, however, is lost in the experimental realization. This is mainly due to finite temperature and impurity effects which broaden the line widths. Semiclassical methods provide an alternative approach. In the form applied in this dissertation, they naturally introduce a hierarchy of energy resolutions. This makes semiclassical approximations a well adapted tool for the description of systems which are subject to finite temperature and impurity effects (see Sec. 3 for details on this point). The semiclassical ansatz considerably reduces the numerical effort involved in the theoretical description of mesoscopic systems.

Formally, semiclassical approximations are approximations of quantum mechanical equations in leading order in $\hbar$. They yield asymptotically correct descriptions for states with high quantum numbers. In practice, however, even the ground state is usually well reproduced. For integrable systems the basic ideas for an expansion of quantum mechanics in orders of $\hbar$ were set up by Wetzel, Kramers and Brillouin [85, 51, 20] soon after the formulation of wave mechanics. Completely chaotic systems, in contrast, could not be treated with this approach. For those, it took until the late 60's to derive an appropriate formulation, the famous Gutzwiller *trace formula*. This Fourier-like sum has classical periodic orbits as individual Fourier components, so that this theory is also termed *periodic orbit theory* (POT). This new ansatz led to a revival of semiclassical approximations, which attracted more and more interest. The trace formula was extended to a large variety of systems, including systems with continuous symmetries or mixed phase space. Analogous formulae were developed for other observables than the level density, e. g. conductance and susceptibility.

An appealing feature of the trace formula is that it can be expressed in terms of the classical properties of the system. It establishes as such a connection between the quantum oscillations and the classical dynamics of the system. The POT is therefore not only a convenient tool calculating the properties of mesoscopic systems. It additionally opens up the possibility of an intuitive interpretation of the observed quantum interference effects in terms of classical periodic orbits. This often underestimated feature removes the 'black box' character of quantum calculations. An intuitive understanding of the origin of the interference effects provides a powerful guideline for designing devices with certain desired properties.

A central problem for all semiclassical approximations is the question of the range of applicability. Under which conditions does the leading order in $\hbar$ contain the essential physics, and when are higher-order contributions to be included? A possible approach to this question is to consider higher-order expansions in $\hbar$. There are attempts following this ansatz [30], but they are both analytically and numerically extremely involved. The aim of the present work is to examine higher-order $\hbar$ corrections without loosing the main advantages of semiclassical approximations, namely their numerical and conceptual simplicity. This work therefore considers some prominent corrections in higher order of $\hbar$, calculates their influence and gives an intuitive explanation of their origin and strength. The goal is to provide rules based on easily accessible data whether certain $\hbar$ corrections have to be taken into account. This knowledge is finally used to describe the experimentally observed features of the magnetoconductance of a mesoscopic device.

This thesis is structured as follows: The first part (chapter 4) is dedicated to the examination of a model system, the circular disk. Its simplicity will allow quite detailed investigations, since $\hbar$ corrections can be included analytically. The applicability to experiment is limited, so that the results are only compared to the corresponding quantum data. The second part of this work applies the semiclassical approach to experiments on magnetoconductance. First the free electron gas is considered as a simple example (chapter 6). Later in chapter 7 the channel with central antidots is treated exemplarily for realistic, and thus more complicated situations. The merits and limitations of the semiclassical approximation are considered, and higher order $\hbar$ effects are examined both theoretically and in the experimental data.

Each of these two parts is preceded by a chapter providing an overview of the applied methods. They give a summary of the relevant literature and present the techniques developed in this thesis.

The last chapter is both a summary and an outlook, collecting the main results and pointing out open questions which seem worth further investigations.

Please note that, apart from the short section on the integer hall effect in chapter 6 this thesis only contains information published[2] in refereed journals. Whenever possible, please cite the original publications instead of this work.

[2] Chapter 4 on the disk billiard, including the work on the correct implementation of smoothing presented in Sec. 3.4 and Sec. 3.2, is contained in Refs. [4, 5]. The relation between dislocations and bifurcations of the channel with antidots of chapter 7 is submitted and available as preprint [6], the remaining part of chapter 7 is presently prepared for publication [7].

Before starting out I want to apologize sincerely for all the errors on the following pages. They somehow found a way to escape my notice. All readers willing to contribute to the collection of misprints are invited to communicate their findings to `mail@joachim-blaschke.de`. Thanks for your kind cooperation.

Chapter 2

Semiclassical approximations

Semiclassics are usually defined as approximations of the quantum mechanical equations to leading order in $\hbar$. This definition is accurate, short, and self-contained — but by no means self-explaining. This chapter first provides the necessary context by giving a short overview of the history of semiclassical approximations before presenting the modern form used in the subsequent chapters.

Contents

The classification of semiclassical approximations in theories for integrable, purely chaotic and mixed systems follows roughly the historical development of the discipline. This chapter introduces the central ideas of semiclassical approximations for the different situations following more or less this chronological order. It does not attempt, however, to review the whole variety of different approaches developed so far, but will concentrate on key ideas and methods relevant for the present work.

2.1 Integrable systems

The first attempts that – from a modern point of view – would be called semiclassical date back prior to the development of wave mechanics. The empirical Bohr-Sommerfeld quantization rule

$$S = \oint \boldsymbol{p}\, d\boldsymbol{q} = 2\pi\hbar \cdot n \quad (n \in \mathbb{N}) \tag{2.1}$$

successfully explained the spectrum of hydrogen and ionized helium. Despite huge efforts, however, it completely failed for neutral helium. When in 1926 the wave mechanical approach successfully explained this long-considered problem, it superseded the Bohr-Sommerfeld scheme, and the role closed orbits play for quantization was ignored for nearly half a century.

Soon after, an expansion of the new wave mechanical quantum theory in powers of $\hbar$ was given by Wentzel, Kramers and Brillouin [85, 51, 20]. It is usually called *WKB-approximation*. The two key ideas are

1. Separate the wave function in a real amplitude and a (unit) phase factor according to

$$\Psi(\boldsymbol{r},t) \;=\; A(\boldsymbol{r},t)e^{iR(\boldsymbol{r},t)/\hbar}\;. \tag{2.2}$$

The quantum momentum of the particle

$$\langle\ \Psi\ |\ -i\hbar\nabla\ |\ \Psi\ \rangle\ = \nabla R A^2 - i\hbar A\nabla A \tag{2.3}$$

is well defined and finite in the *semiclassical limit* $\hbar \to 0$. Inserting this ansatz in the Schrödinger equation yields two equations for A and R, equivalent to the time evolution of the real and the complex part of the wave function. For a Hamiltonian $H = \boldsymbol{p}^2/2m + V(\boldsymbol{r})$ this results in

$$\frac{\partial R}{\partial t} + \frac{(\nabla R)^2}{2m} + V(\boldsymbol{r}) - \frac{\hbar^2}{2m}\frac{\nabla A}{A} \;=\; 0\;, \tag{2.4}$$

and

$$\frac{\partial A}{\partial t} + \frac{\nabla R \nabla A}{m} + \frac{A\nabla R}{2m} \;=\; 0\;. \tag{2.5}$$

These equations are the starting point of Madelung's *hydrodynamic picture* of quantum mechanics [56]. The naming was motivated by the fact that with $\rho := A^2$ and $\boldsymbol{v} := \nabla R/m$ Eq. (2.5) takes the form of a continuity equation $\dot{\rho} + \nabla(\rho\boldsymbol{v}) = 0$.

2. The semiclassical approximation corresponds to the limit $\hbar \to 0$, which is well defined for Eqs. (2.4) and (2.5). In this limit the last term in Eq. 2.4, the so-called *quantum potential*, vanishes[1]. This equation then takes the form of a classical Hamilton-Jacobi equation $\dot{R} + H(\boldsymbol{r}, \nabla R) = 0$. Using this analogy it can be shown that R is in fact given by Hamilton's principal function along a classical path.

For one-dimensional (or separable) systems the Hamilton-Jacobi equation can be solved in general. The condition of the simple-valuedness of the wave function leads to quantization conditions. These can be written down explicitly,[2] taking exactly the form of the Bohr-Sommerfeld rule Eq. (2.1).

The classical turning points, however, introduce additional subtleties.[3] This was first realized by Kramers [51], who derived additional phase factors $\mu\pi/2$ using his *connection formulas*. These factors correspond to phase shifts at reflections. In Sec. 4.3.2 this point will be considered in some more detail. The quantization condition is modified by the additional phases according to

$$S = \oint \boldsymbol{p}\, d\boldsymbol{q} = 2\pi\hbar \left(n + \frac{\mu}{4}\right) \quad (n \in \mathbb{N}) \,. \tag{2.6}$$

The additional phases from the classical turning points shift the energy spectrum. As such, they are responsible for the quantum mechanical zero point energy.

The WKB approach can be generalized to *integrable systems*, i. e. systems with as many constants of motion as degrees of freedom. In these systems the phase-space motion is confined to a torus.[4] The closed paths along which the quantization in analogy to Eq. (2.6) has to be performed are the topological invariant closed paths on this torus. In this form, it is usually named *EBK* after Einstein, Brillouin and Keller [45]. Whereas for (effectively) one-dimensional systems the classical turning points lead to additional phases, in higher dimensions their role is taken by focusing points of trajectories in configuration space, the so-called *caustics*. These correspond to foldings in phase space, where the orientation of the configuration-space surface changes. The additional phases, which are nowadays called *Maslov indices*[5], only depend on the topology of the classical path.

The Maslov indices are one ingredient necessary for a successful semiclassical quantization of the neutral helium which was missed by Heisenberg and coworkers in their attempts prior to 1926. The second problem they did not take into account is that Helium, a three-body problem, is not integrable, but chaotic. The role of classical orbits for the quantization of chaotic problems remained unclear for another decade.

2.2 Chaotic systems

The methods presented above result in an energy quantization rule which depends on individual, characteristic orbits of the system. The general hope was that the close con-

[1] The alternative interpretation of quantum mechanics presented by Bohm [109] preserves the quantum potential. It solves the Hamilton-Jacobi equation including this amplitude-dependent term. A recent work shows that this ansatz might be helpful in the interpretation of the quantum measurement process [102].

[2] For explicit examples, see, e. g., section 2.4 of Ref. [100].

[3] The formal reason is that at classical turning points the quantum potential is not negligible.

[4] This holds for bounded systems, to be precise.

[5] The definition of the Maslov index is not consistent in the literature. In this work, the term is laxly used for all additional phases in multiples of $\pi/2$.

nection between single orbits of the system and individual quantum states established for integrable systems would also hold in the non-integrable case. This belief turned out to be wrong, and obscured for a long time the way to a semiclassical treatment of chaotic systems. In a series of papers [36, 37, 38, 39, 40] starting in 1967, Gutzwiller established the long-searched bridge between classical chaotic dynamics and quantum properties of the system. This work constitutes the foundation of modern semiclassical theories. The central result, the famous *trace formula* for the level density of a completely chaotic system, has by now been re-derived using various alternative approaches. Whereas the original work of Gutzwiller started out with the Feynman path integral, Bogomolny uses a description of the Schrödinger equation in terms of a semiclassical transfer operator acting on the Poincaré map [16], and Smilansky employs a scattering approach [106]. Citanović and coworkers [101] calculate the quantum mechanical propagator K using the fact that K itself solves the Schrödinger equation. The corresponding wave function is approximated by a very nice generalization of the multidimensional WKB scheme to non-integrable systems. Readers interested in details on these derivations are referred to the original literature or to the recent reviews Refs. [100, 105]. Here, only the main ideas leading to the Gutzwiller trace formula will be sketched.

2.2.1 The semiclassical Propagator

The quantum mechanical propagator K is the operator that propagates a wave function Ψ through time :

$$\Psi(\boldsymbol{r},t) = K(\boldsymbol{r},\boldsymbol{r'};t)\,\Psi(\boldsymbol{r'},0)\ . \tag{2.7}$$

A semiclassical approximation can be derived starting out with the Feynman path integral expression of the propagator

$$K(\boldsymbol{r},\boldsymbol{r'};t) = \int \mathcal{D}\boldsymbol{r}\ \exp\left(\frac{i}{\hbar}R(\boldsymbol{r},\boldsymbol{r'};t)\right)\ , \tag{2.8}$$

where R is Hamilton's principal function. $\int \mathcal{D}\boldsymbol{r}$ denotes an infinite-dimensional integration. It extends over all paths from $\boldsymbol{r'}$ to $\boldsymbol{r}$ in time t. The integrand is rapidly oscillating, so that most of the contributions to K cancel. This type of integrals can be well approximated using the *stationary phase approximation*, one of the central techniques in semiclassics. In one dimension, it is given by

$$\begin{aligned}\int_{\gamma_1}^{\gamma_2} e^{\frac{i}{\hbar}R(\gamma)}\,d\gamma &= \int_{\gamma_1}^{\gamma_2} e^{\frac{i}{\hbar}(R_0+R_2(\gamma-\gamma_0)^2+R_3(\gamma-\gamma_0)^3+\dots)}\,d\gamma \\ &\approx \int_{-\infty}^{\infty} e^{\frac{i}{\hbar}(R_0+R_2(\gamma-\gamma_0)^2)}\,d\gamma \;=\; e^{\frac{i}{\hbar}R_0}\sqrt{\frac{\pi}{|R_2|}}\;e^{i\,\mathrm{sign}(R_2)\pi/4}\ .\end{aligned} \tag{2.9}$$

If more stationary points exists, their contributions have to be summed up. The generalization to more dimensions is straight forward. The stationary points of the exponent of Eq. (2.8) correspond to the classical paths. Therefore the stationary phase approximation of K consists of the replacement of the integral over *all* paths from $\boldsymbol{r'}$ to $\boldsymbol{r}$ by the appropriately weighted *classical* ones.

The resulting approximation of the propagator was – apart from the indices ν, which again stem from caustic points[6] – already proposed by Van Vleck [86] back in 1928:

$$K_{\mathrm{sc}}(\boldsymbol{r},\boldsymbol{r'};t) = \left(\frac{1}{2\pi i\hbar}\right)^{D/2} \sum_{\Gamma(\boldsymbol{r},\boldsymbol{r'};t)} \sqrt{\det\left|\frac{\partial^2 R}{\partial \boldsymbol{r}\partial \boldsymbol{r'}}\right|} \quad \exp\left(\frac{i}{\hbar}R(\boldsymbol{r},\boldsymbol{r'};t) - i\nu\frac{\pi}{2}\right) . \tag{2.10}$$

Here $\Gamma(\boldsymbol{r},\boldsymbol{r'};t)$ denotes the sum over all classical paths connecting $\boldsymbol{r}$ and $\boldsymbol{r'}$ in time t, and D is the system dimension. Eq. (2.10) is one of the key formulas to modern semiclassical theories.

2.2.2 The semiclassical Green's function

More convenient than the propagator is the Green's function, its (half-sided) Fourier transform with respect to time

$$G(\boldsymbol{r},\boldsymbol{r'};E) = -\frac{i}{\hbar}\lim_{\varepsilon\to 0}\int_0^\infty K(\boldsymbol{r},\boldsymbol{r'};t)\ \exp\left(\frac{i}{\hbar}(E-i\varepsilon)t\right)\ dt\ . \tag{2.11}$$

Gutzwiller treated the case where all classical orbits are *isolated* in phase space, i. e. have no neighbor with the same energy and action at infinitesimal distance. If additionally the actions S of the classical trajectories are much larger than $\hbar$, the integrations perpendicular to the classical paths can be performed in stationary phase approximation. This leads to the semiclassical approximation of the Green's function according to

$$G_{\mathrm{sc}}(\boldsymbol{r},\boldsymbol{r'};E) = \frac{2\pi}{(2\pi i\hbar)^{\frac{D+1}{2}}} \sum_{\Gamma(\boldsymbol{r},\boldsymbol{r'};E)} \sqrt{\det\begin{vmatrix} S_{\boldsymbol{r'}\boldsymbol{r}} & S_{\boldsymbol{r'}E} \\ S_{E\boldsymbol{r}} & S_{EE}\end{vmatrix}}\ \exp\left(\frac{i}{\hbar}S(\boldsymbol{r},\boldsymbol{r'};E) - i\mu\frac{\pi}{2}\right)\ , \tag{2.12}$$

where S_{kl} denotes the partial derivatives $\partial^2 S/(\partial k\,\partial l)$. The summation extends over all classical paths Γ with fixed energy E connecting $\boldsymbol{r'}$ and $\boldsymbol{r}$.

The general strategy for semiclassical approximations is to find an exact expression of the desired quantity in terms of Green's functions. Replacing the Green's functions by their semiclassical approximations yields a semiclassical formula for the desired observable. This procedure will be used in the following section to derive a semiclassical formula for the level density. In chapter 5 the same approach will lead to a semiclassical expression for the conductivity.

2.2.3 The semiclassical level density

The level density can be expressed in terms of Green's function as

$$g(E) = -\frac{1}{\pi}\lim_{\varepsilon\to 0}\mathcal{I}m\left[\mathrm{Tr}(G(\boldsymbol{r},\boldsymbol{r},E+i\varepsilon))\right]\ . \tag{2.13}$$

The classical paths from $\boldsymbol{r}$ to $\boldsymbol{r}$, i. e. the closed paths, fall into two groups: The orbits with zero length, and finite length orbits returning to $\boldsymbol{r}$. The contribution of the zero length orbits has to be evaluated separately, since they violate the condition $S \gg \hbar$,

[6] These *Morse indices* slightly differ from the Maslov indices μ.

which is required for the validity of the stationary phase approximation. These orbits lead to the average density of states $\tilde{g}(E)$, which alternatively can be calculated using the familiar Thomas-Fermi relation. From now on, only the contributions of finite-length orbits will be considered. These are responsible for the oscillatory deviations $\delta g(E)$ from the smooth part $\tilde{g}(E)$. Performing another stationary phase approximation to evaluate the trace integral yields the famous Gutzwiller *trace formula*

$$\delta g(E) \approx \frac{1}{\pi\hbar} \sum_{\mathrm{po}} \underbrace{\frac{T_{\mathrm{PPO}}}{\sqrt{|\det(\widetilde{M} - \mathbb{1})|}}}_{:= A_{\mathrm{po}}} \cos\left(\frac{S}{\hbar} - \mu\frac{\pi}{2}\right) . \tag{2.14}$$

The summation extends over all classical *periodic* orbits po of the system. T_{PPO} is the period of the *primitive* orbit, i. e. the part of the orbit until it first closes in phase space. The *stability matrix* $\widetilde{M}$ is given by the non-trivial part of the *Monodromy matrix* M. It is related to the stability of an orbit. This quantity is explained in detail in appendix A.1.2. The factors in front of the cos-term are usually collectively called *semiclassical amplitude* A_{po} of an orbit. Formula Eq. (2.14) is often given in an analog form which separates the sum over the different orbits from the sum over their repetitions. In this thesis the sum over the repetitions should always be included in the sum over all orbits.

Please note that the trace formula for the semiclassical quantization of chaotic systems has a completely different structure than the quantization conditions for the integrable case. Whereas for the latter individual paths in the system are related to single quantum states, in chaotic systems each periodic orbit contributes to all energy levels.

The Gutzwiller trace formula provided the basis for a successful semiclassical treatment of neutral helium, which was finally accomplished in 1991 [28]. 65 years after the same problem had set an end to the empirical quantization rules, this was a great success for the growing semiclassical community. In the following years searching for traces of classical orbits in quantum spectra as well as superposing classical trajectories to approximate shell structures or even individual quantum levels have been recognized as powerful theoretical tools.

For the purpose of this work, two generalizations of the trace formula are needed, namely the extension to continuous symmetries and to systems with mixed phase space. These will be presented in the following sections.

2.3 Continuous symmetries

For systems with continuous symmetries the Fourier integral Eq. (2.11) can not be evaluated as sketched above. A suitable adaption of the procedure has been proposed by Strutinsky and Magner [76] and, in a more general form, by Creagh and Littlejohn [23]. The main idea of the latter generalization is a separation into a symmetry-free system which is treated in analogy to the Gutzwiller case, and the symmetry degrees of freedom, over which the integrations are performed exactly. The structure of the trace formula Eq. (2.14) remains essentially unchanged by this procedure, but the definition of the amplitudes is different, reflecting the different structure of the underlying classical dynamics:

$$\delta g(E) \quad \approx \quad -\frac{1}{\pi}\mathcal{I}m\left[\frac{1}{i\hbar}\frac{1}{(2\pi i\hbar)^{k/2}}\sum_{po}\int_{po} dt\; d\boldsymbol{\mu}(\boldsymbol{g})\; |K_{po}|^{-1/2} e^{i\frac{S_{po}}{\hbar} - i\sigma_{po}\frac{\pi}{2}}\right] =$$

$$=: \quad -\left(\frac{1}{\pi\hbar}\right)^{\frac{k+2}{2}} \mathcal{I}m \left[\sum_{po} A_{po} e^{i\frac{S_{po}}{\hbar} - i\sigma_{po}\frac{\pi}{2}}\right] . \tag{2.15}$$

The dimensionality of the symmetry is denoted by k. The integral over t replaces the period of the primitive orbit T_{PPO} in the Gutzwiller case. $\int_{po} d\boldsymbol{\mu}(\boldsymbol{g})$ is the integration over the symmetry, where $\boldsymbol{\mu}(\boldsymbol{g})$ denotes the measure of the symmetry group. The stability term of the Gutzwiller formula is replaced by $|K|^{1/2}$, where

$$K = Q \det(W) \det(\widetilde{M} - I) . \tag{2.16}$$

Here $\widetilde{M}$ is the stability matrix of the symmetry-reduced system. Q depends only on the type of symmetry. For Abelian symmetries $Q = 1$, and for three-dimensional rotational symmetry $Q = J^{-2}$, where J denotes the total angular momentum. Trajectories which are periodic in the symmetry-reduced system do not necessarily close in complete phase space. This leads to the additional factor $\det(W)$, where

$$W_{ij} = \frac{\partial \Theta_i}{\partial J_j} . \tag{2.17}$$

The Θ_i are the operators of the symmetry and the J_i are the corresponding conserved quantities. The topological index σ is given by $\sigma = \mu - \delta$, where δ is the number of negative eigenvalues of W. The Maslov index μ is the same as in the original Gutzwiller formula.

This approach can deal with continuous symmetries of arbitrary dimensionality. Each symmetry dimension corresponds to one constant of motion J_i. Eq. (2.15) applies even to integrable systems, where the number of J_i equals the degrees of freedom. The trace formula of Creagh and Littlejohn therefore provides a unified description of integrable and chaotic systems. Although it can also be applied to systems with mixed phase space, it cannot deal with the transition from regular motion to chaos. This problem will be dealt with in the following section.

The power in $\hbar$ of the contributions of the classical periodic orbits depends on the dimension of the symmetry. This implies that the amplitude of the oscillating part of the level density is larger for highly symmetric systems. In systems where different orbits have different dimensions of symmetry, their power in $\hbar$ is different. The leading-order contribution in $\hbar$ stems from the orbits with the highest continuous symmetry, whereas the other orbits give rise to $\hbar$ corrections. In chapter 4 this point will be discussed in more detail for the example of the disk billiard.

2.4 Mixed phase space

The semiclassical methods described above apply either to the integrable or to the completely chaotic situation. Many realistic physical systems, however, show a mixed phase-space structure. This introduces additional complications for semiclassic approximations, which are not completely settled by now. Only the ansatz of Bogomolny [16] does not explicitly assume regular or chaotic motion, so that it can deal with mixed phase space as well – but unfortunately only on a numerical level. The standard Gutzwiller approach cannot cope with the transition from regular to chaotic behavior. The extensions which

have been worked out to overcome this limitation will be introduced in this section. They build the basis for the considerations in the following chapters.

As pointed out above, the phase-space motion of an integrable system is confined to a torus. The periodic orbits of those systems are given by the repetitions of the elementary loops of the Bohr-Sommerfeld quantization. There are only a few such orbits up to a given maximum period T_m. Their number increases as a power law with T_m. In completely chaotic[7] systems, however, the number of periodic orbits increases exponentially with the period according to $N \propto 1/(hT_m)\exp(hT_m)$, where h is the topological entropy.

This implies that a system on its way from regular to chaotic motion creates new classical periodic orbits. These creation points are called *orbit bifurcations*. The underlying mechanism is visualized in Fig. 2.1. There, the situation prior to the integration of Eq. (2.13) is illustrated. The solid line gives the action in dependence of $\boldsymbol{r}$, and the arrows indicate the stationary points, i. e. the classical *periodic* paths. Varying an external parameter of

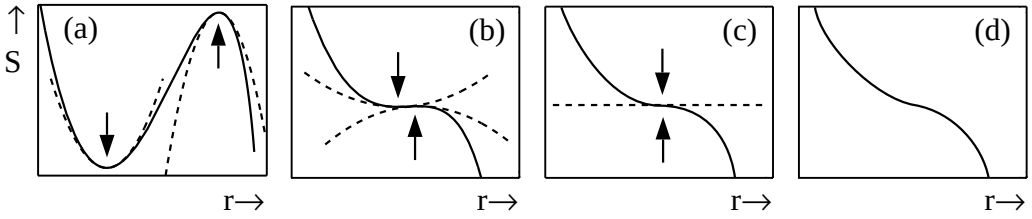

Figure 2.1: *The classical action $S(\boldsymbol{r}, \boldsymbol{r}; E)$ of a one-dimensional system in dependence of an external parameter. The parabolas give the local quadratic approximations at the stationary points.*

the system changes the functional dependence of S on $\boldsymbol{r}$. The two extrema, i. e., the two periodic orbits in (a) approach (b), fall together (c) and finally disappear (d). From right to left, these pictures illustrate the birth of two periodic orbits. This is the simplest type of bifurcation, called tangent bifurcation.

In Gutzwiller's derivation, the integration of Eq. (2.13) is performed in stationary phase approximation. According to Eq. (2.9), this means to replace the integral over $\boldsymbol{r}$ by the integrals over the parabolas approximating $S(\boldsymbol{r}, \boldsymbol{r}; E)$ at the stationary points. These second-order approximations are given by the dotted lines in Fig. 2.1. Obviously the stationary phase approximation gets inaccurate for orbits in close vicinity. At the point where the orbits coincide the fit parabolas have zero curvature. Since the amplitude of the orbits is in this approximation proportional the inverse curvature of these parabolas, the Gutzwiller approximation diverges at bifurcation points.

To overcome this problem, a local expansion to higher order in the action has been proposed by de Almeida and Hannay [8] or Kus *et al.* [53]. Such a local approximation, however, does not reproduce the Gutzwiller limit of well separated orbits. Retaining both the correct asymptotic and local behavior is possible using *uniform approximations*, which interpolate smoothly between the limiting cases. These have been developed most systematically by Schomerus and Sieber [72, 70, 73]. Bifurcations can be classified according to their normal form, and the authors give explicit formulas for all generic bifurcations in terms of the amplitudes, actions and Maslov indices of the orbits engaged. Non-generic cases, e. g. systems with discrete symmetries, are not directly covered by these formulas and need special care. The expressions for the two types of bifurcations relevant for this

[7] This holds for ergodic systems, to be precise.

thesis are given in appendix B. Eqs. (B.7) and (B.8) apply to the tangent bifurcation, and Eq. (B.15) to the period doubling bifurcation.

The Gutzwiller approximation only contains information about the classical phase-space structure. At first sight, the uniform approximations of Schomerus and Sieber are expressed in dependence of the same terms. They include, however, also contributions of *ghost orbits*, i. e., analytic continuations of orbits beyond the regime where they classically exist. This exceeds the purely classical phase space properties. In systems where the periodic orbits are known analytically, this additional information is readily available. If the equations of motion are solved numerically, however, this information can hardly be accessed. This problem will be examined in more detail in chapter 7.

As can be deduced from the analytical local form of the bifurcation, the contributions of the orbits engaged in a bifurcation are increased by a factor $\hbar^{-\delta}$ [70]. δ is positive; its value depends on the type of the bifurcation. The negative exponent shows that the bifurcations are of leading order in $\hbar$. Thus, these points dominate in the semiclassical limit $\hbar/S \to 0$ (with S being the action of a typical periodic orbit in the system). This gives a more formal explanation for the divergence of the standard Gutzwiller-like approximation at these points. The problems related with bifurcations will be examined in detail for the level density of the disk billiard in chapter 4 and for the magnetoconductance of a channel with antidots in chapter 7.

Systems with mixed phase space may exhibit even more complicated structures in the classical dynamics than the bifurcations discussed above. Just as bifurcations occur when in dependence of an external parameter two (or more) orbits approach and finally coincide, also two bifurcations can approach and fall together. This is called a bifurcation of codimension 2.[8] Treating those requires normal forms of even higher order in the action. The bifurcations of codimension 2 have recently been classified by Schomerus [69, 71]. He also presented formulas for their uniform approximation. For bifurcations of higher codimension, however, a general treatment is still lacking. The analytic complexity of the corresponding uniform formulae would anyway make them useless for practical applications. For the context of this work, the consideration of the 'ordinary' bifurcations of codimension 1 will be sufficient.

With the extension to systems with continuous symmetries of Sec. 2.3 and including the bifurcations by uniform approximations, integrable and chaotic systems as well as systems with mixed phase space can be described semiclassically. This generalized trace formula constitutes the main tool for the present work.

Prior to the application of this semiclassical trace formula to the disk billiard, some technical details have to be worked out. This will be done in chapter 3, where the convergence properties of the orbit sum are examined in the necessary detail. Readers mainly interested in physics are invited to page 27 immediately.

[8] This is not the exact definition of a bifurcation of codimension 2, since some "bifurcations of bifurcations" can still be described in a one-dimensional parameter space. This distinction, however, is irrelevant in the context of this work.

Chapter 3

Smoothing quantum oscillations

This chapter is devoted to the inclusion of finite temperature and impurity scattering in semiclassical approximations. The common microscopic approach is outlined, and another, more mathematically oriented ansatz is presented. The comparison of the two procedures allows an extension of the smoothing formalism to higher-order contributions in $\hbar$. This section provides some of the technical details which will be important when considering $\hbar$ corrections in the subsequent chapters.

Contents

The quantum mechanical level density of pure systems is given by a sum of δ-functions centered at the eigenenergies. Experiments on mesoscopic systems, however, are performed at finite temperatures. Furthermore, the samples are not ideally clean, but incorporate impurities (contaminations, lattice defects, etc.). These effects broaden the levels to a finite width, thus *smoothing* the level density. If the line width is smaller than the mean level spacing, the individual quantum states can still be observed. This situation will be referred to as *full quantization*. For larger smoothing widths, i. e. line widths larger that the mean level spacing, the individual levels cannot be resolved. This is called the *coarse-grained* level density in the following.

Only for very peculiar systems, like the harmonic oscillator, are the levels regularly distributed in energy. The generic situation for finite fermion systems are groups of levels, separated by gaps larger than the mean level spacing. These groups are called *shells* according to the canonical example of the electronic s-, p-, d-, ... shells in atoms. This *shell structure* survives even for strong broadening of the lines. It is therefore often the only experimentally observable reminiscence of the quantum nature of a sample. Those shell effects are a typical feature of finite fermion systems. Prominent examples include the abundance spectra of alkali clusters [50, 26] or the stability of nuclei [117].

This chapter deals with techniques that include the effects which lead to finite line widths in the semiclassical trace formula. The common ansatz starts with including the microscopic effects on a quantum mechanical level and re-derives the semiclassical approximation along the same line as calculating the original trace formula. The resulting expression differs from the simple trace formula Eq. (2.14) by additional terms that damp the amplitudes of the periodic orbit contributions.

In Sec. 3.2, an alternative ansatz is derived. The essential idea is to establish a formal relation between line shapes and amplitude damping schemes. Provided the knowledge of the correct line shape, this method can also be used for the calculation of the corresponding amplitude damping factors.

In leading order of $\hbar$, these two approaches lead of course to equivalent results. The second technique, however, can be generalized to higher-order contributions. The idea exploited in Sec. 3.3 is to replace the microscopic ansatz by the second approach if higher orders in $\hbar$ are to be included. This will be of great importance for the examination of higher-order contributions in $\hbar$ to the trace sum in the subsequent chapters.

A couple of nice side results from the inclusion of finite line widths in the trace formula are discussed in Sec. 3.4.

3.1 The microscopic approach to smoothing

The general scheme how to include finite temperatures, impurity scattering, and related effects on a microscopic level necessitates the re-derivation of the trace formula. After incorporating the effect in the quantum mechanical calculation, e. g. by including weak disorder or finite temperature by the appropriate ensemble averages, the Green's functions are replaced by their semiclassical approximations. Subsequent stationary phase approximations lead to trace formulae similar to Eq. (2.14). This approach opens up the possibility of a semiclassical calculation of line shapes and line widths. Note, however, that despite recent progress [60] the quantum mechanical calculation of line shapes and

line widths is still a mostly unsettled problem.[1] Since the semiclassical approximation starts from the quantum formalism, this is equally true for for semiclassics. This work is not intended to contribute to questions related to line shapes and relative amplitudes, so that temperature and scattering will only be included along the simple lines outlined below.

For the very low temperatures used in the measurement of mesoscopic semiconductor devices, phonons (and their interaction with charge carriers) can be neglected. The only relevant temperature-related effect concerning the level density stems from the Fermi distribution. For this situation, the inclusion of finite temperature on the oscillating part of the level density is simply given by

$$\delta g(\mu, T) = \int_0^\infty dE\, \delta g(E, T=0)\, f'(E-\mu)\ , \tag{3.1}$$

with the Fermi distribution function

$$f(E-\mu) = \frac{1}{1+\exp\left(\frac{E-\mu}{k_B T}\right)}\ . \tag{3.2}$$

The derivative of the Fermi distribution is strongly peaked around the Fermi energy μ, so that Eq. (3.1) mainly introduces an energy average over a typical width of $k_B T$. Performing this integration leads to an additional temperature-dependent factor R in the trace formula

$$R(T_{\mathrm{po}}) = \frac{T_{\mathrm{po}}/\tau_T}{\sinh(T_{\mathrm{po}}/\tau_T)}\ . \tag{3.3}$$

Here T_{po} is the period of the orbit and $\tau_T = \hbar k_B T/\pi$ defines the thermal cutoff time τ_T. For a detailed derivation, see for example Refs. [96, 105, 100, 17].

The inclusion of impurities in semiclassical formulae is, even on an elementary level, much more elaborate than including finite temperature. In the semiclassical picture, scattering enters via three distinct effects:

1. The amplitudes of the periodic orbits are reduced due to the finite probability of scattering out of the trajectory. This effect is relevant even for small impurity concentrations.

2. New orbits which include scattering events (i. e. closed 'hopping' orbits from scattering center to scattering center) occur. These orbits are for example responsible for universal conductance fluctuations (UCF) and weak localization. This effect is only relevant for sufficiently high concentrations of scatterers.

3. Scattering may introduce interference between otherwise coherent orbits (like in degenerate orbit families).

In ballistic systems, the first of these effects dominates. Since scattering will only be considered with respect to transport properties in later sections, the discussion about the inclusion of the effects is postponed until then. Here only the main result of this analysis

[1] This applies especially to transport properties. So for example not even the amplitude of the Shubnikov-de-Haas oscillations of the free 2DEG is understood theoretically [125].

should be stated, namely that for ballistic systems the procedure is very similar to the inclusion of finite temperatures. The effect of the scatterers can be approximated by a damping factor F depending exponentially on the orbit length

$$F(L_{\mathrm{po}}) = e^{-L_{\mathrm{po}}/(2\ell)} \; . \tag{3.4}$$

Here ℓ is the elastic mean-free path of the system and L_{po} denotes the orbit length. For billiards, where $L_{\mathrm{po}} = v_F T_{\mathrm{po}}$, this damping can also be expressed in terms of the scattering time τ_s by

$$F(T_{\mathrm{po}}) = e^{-T_{\mathrm{po}}/(2\tau_s)} \; , \tag{3.5}$$

where the scattering time is related to the mobility μ by $\tau_s = m^\star \mu / e$.

These two results establish a first connection between smoothing and amplitude damping, a relation that will be examined more deeply in the following section. Please note that the semiclassical inclusion of finite temperature and mean-free path is – just as the trace formula itself – only correct up to leading order in $\hbar$. Therefore this approach is not appropriate for the inclusion of higher-order $\hbar$ terms. For those contributions, a modified smoothing scheme needs to be developed.

3.2 The relation between smoothing and amplitude damping

Finite temperature and scattering lead to finite widths of the individual energy levels. The effect is equivalent to a convolution of the δ-functions constituting the level density with the line shape induced by temperature and impurity effects. This section discusses from a more mathematical point of view how this convolution integral can be implemented in the trace formula. The main result is Eq. (3.18), which states a one-to-one relation between line shapes and amplitude damping functions.

The general form of a trace formula is given by

$$\delta g \;=\; \sum_{\Gamma} A_\Gamma(E)\, e^{i\frac{S_\Gamma(E)}{\hbar} - i\sigma_\Gamma \frac{\pi}{2}} \; , \tag{3.6}$$

where Γ is a one-dimensional classification of the classical periodic orbits. If there is a generalized energy $e(E)$, and functions $G(\Gamma, E)$ and $\tilde{\sigma}(G)$, which fulfill

$$\frac{S_\Gamma(E)}{\hbar} - \sigma_\Gamma \frac{\pi}{2} = eG - \tilde{\sigma}(G) \; , \tag{3.7}$$

the trace formula can be rewritten as

$$\delta g \;=\; \sum_{G} A_2(e, G)\, e^{ieG} \; . \tag{3.8}$$

For the last step it was assumed that every orbit is uniquely determined by its value of G. By rescaling, $G \in \mathbb{N}$ can always be obtained; the rescaling factors should be included in

$A_2(e, G)$. The most simple situation is that A_2 factorizes in terms depending only on the generalized energy e and the classification variable G:

$$A_2(e, G) = A_G(G)\, A_e(e)\ . \tag{3.9}$$

Approximating Eq. (3.8) by an integral

$$\delta g \ \approx\ A_e(e) \int A_G(G)\, e^{ieG}\, dG\ . \tag{3.10}$$

gives (apart from normalization constants) the oscillating part of the level density δg as the Fourier transform of $A_G(G)$:

$$\delta g(e) \approx \sqrt{2\pi}\ A_e(e)\ \mathcal{F}[A_G(G)]\ . \tag{3.11}$$

The Fourier transform is denoted by

$$\mathcal{F}[A_G(G)] := \frac{1}{\sqrt{2\pi}} \int A_G(G) e^{ieG}\, dG\ . \tag{3.12}$$

Using the well-known folding theorem, an arbitrary *window function* $F(G)$ leads to

$$\int F(G)\, A_2(e, G)\, e^{ieG}\, dG \ \approx\ \delta g(e) * f(e)\ . \tag{3.13}$$

Here $f(e) = \mathcal{F}[F(G)]$ denotes the Fourier transform of $F(G)$ and "$*$" stands for the convolution integral. Therefore

$$\delta g^F := \sum_\Gamma F(G)\, A_\Gamma(E)\, e^{i\frac{S_\Gamma(E)}{\hbar} - i\sigma_\Gamma \frac{\pi}{2}} \ \approx\ \delta g(e) * f(e)\ , \tag{3.14}$$

where δg^F denotes the trace formula with damped amplitudes. This relation shows that folding the semiclassical level density with a *smoothing function* $f(e)$ is equivalent to a multiplication of the amplitudes with a *window function* $F(G)$. Unfortunately the restrictions of Eqs. (3.7) and (3.9) are quite severe and often prevent the application of Eq. (3.14). With two additional approximations these restrictions can be relaxed.
In the generic situation Eq. (3.9) is violated and only the common dependence of the amplitudes on e can be separated out:

$$A_2(e, G) = A_G(e, G)\ A_e(e)\ . \tag{3.15}$$

In this case Eq. (3.14) is still a good approximation if the variation of $A_G(e, G)$ in e is sufficiently slow. Denoting the characteristic width of $f(e)$ with γ, this means that $A_G(e, G)$ has to be nearly constant over a region γ in e.
If, on the other hand, there are no functions $e(E)$ and $G(E, \Gamma)$ that fulfill Eq. (3.7), a local expansion of the action S in powers of e can be used:

$$\frac{S}{\hbar} = \frac{S(e_0)}{\hbar} + G(e_0)\ (e - e_0) + \mathcal{O}(e - e_0)^2\ . \tag{3.16}$$

If this approximation is valid in a region in e that is wider than the typical width γ of the smoothing function, Eq. (3.14) still holds. In the general case G is therefore given by the first derivative of the classical action with respect to e:

$$G(E) = \frac{1}{\hbar}\frac{\mathrm{d}S}{\mathrm{d}e}\bigg|_E \ . \tag{3.17}$$

With $e = E$, $\hbar G$ is the period T of the orbit, so that $\hbar G$ is referred to as the *quasiperiod*. For systems with constant absolute velocity along the orbit (this holds especially for billiards), the choice $e = k$ leads to

$$\frac{\mathrm{d}S}{\mathrm{d}e} = \frac{\mathrm{d}S}{\mathrm{d}E}\frac{\mathrm{d}E}{\mathrm{d}k} = T \cdot \frac{k\hbar^2}{m} = \hbar L \ ,$$

where L is the geometrical orbit length.

Putting all approximations together, it was shown that damping the amplitudes in the trace formula with a window function $F(G)$ results in an approximation for the level density folded with the Fourier transform of $F(G)$:

$$\delta g^F \approx f(e) * \delta g \ . \tag{3.18}$$

This is the main result of this section. Eq. (3.18) holds if the conditions

$$S \approx S(e_0) + G(e_0)\ (e - e_0) \tag{3.19}$$

and

$$A_2(e, G) \approx \text{const} \tag{3.20}$$

are fulfilled in a region wider than the typical width γ of the smoothing function. These conditions depend mainly on the behavior of the actions and amplitudes of the orbits. In order to match them, a well-adapted choice of the generalized energy is essential. Note that for narrow smoothing functions (small γ), the conditions are less restrictive. Therefore, using Eq. (3.18) is often justified for a full quantization, whereas for the calculation of the gross-shell structure the conditions Eqs. (3.19) and (3.20) put tight limits on the use of the amplitude damping ansatz – which might seem counter-intuitive at first sight. Since every orbit is uniquely determined by its value of G, and G should be sufficiently smooth in practical applications, the amplitude damping scheme may not depend explicitly on the repetition number of the orbit. For most of the the applications of Eq. (3.18) in the present work this limitation will be irrelevant. Note, however, that for the damping scheme commonly used for the free 2DEG (compare to chapter 6), Eq. (3.18) does not apply.

A simple example might be helpful to illustrate the result. Pure billiard systems are those where the the action along the orbits scales with the wave number: $S = \hbar k \cdot L$, and L, the geometric orbit length, is independent of the energy. Setting

$$e(E) = k = \sqrt{\frac{2mE}{\hbar^2}} \quad \text{and} \quad G(\Gamma) = L \ , \tag{3.21}$$

Eq. (3.19) is fulfilled trivially. If Eq. (3.20) is also matched, then the use of a window function F depending on the orbit length L is equivalent to a folding of the level density

in k. Evaluating the trace formula with a Gaussian depending on the orbit length L as window function yields the level density folded with a Gaussian in k. This is the technique commonly practiced for the computation of trace formulas for billiard systems. Eq. (3.18) is somewhat more general, since it is not restricted to billiard systems nor to special window functions.

The use of Eq. (3.18) is very convenient. Its range of validity can easily be checked using Eqs. (3.19) and (3.20). Furthermore, there is no general limitation of its applicability to the leading order in $\hbar$. In the following section Eq. (3.18) will be modified so that it can deal with two $\hbar$ corrections which occur in the disk billiard.

3.3 Smoothing beyond the leading order in $\hbar$

The microscopic ansatz for the inclusion of scattering and finite temperature in the trace formula is, as already pointed out, limited to the contributions of leading order in $\hbar$. It is therefore questionable to use this smoothing scheme for higher-order $\hbar$ terms like bifurcations or grazing, since thereby the influence of the corrections on the smoothing is neglected. The examination of the impact of higher-order $\hbar$ corrections thus demands a generalized smoothing scheme which is applicable to the relevant $\hbar$ corrections. But just as the inclusion of $\hbar$ corrections necessitates an adaption to the smoothing scheme, so does the exclusion thereof. This comes about as omitting $\hbar$ corrections does not only lead to missing terms in the trace sum, but also renders the inclusion of the smoothing inaccurate. A way to distinguish these two effects is desired.

A complete inclusion of second leading order $\hbar$ effects in the microscopic calculation of Sect. 3.1 requires the derivation of the trace formula itself to second order. This task is, as already pointed out, both numerically and analytically so involved that it renders the semiclassical approach useless for practical applications. This work therefore follows a different approach, namely to replace the microscopic approach by the formulas stating the equivalence between smoothing and amplitude damping. The latter formulae shall be found much easier to generalize.

Along this path, the following section derives explicit amplitude damping formulas applicable to two kinds of higher-order $\hbar$ corrections, namely bifurcations and grazing. The ansatz is, however, not restricted to these specific cases but can be used to derive analogous formulae for a large class of corrections.

After that, Sec. 3.3.2 will introduce the *folding approach*, a simple numerical scheme cutting down the influence of higher-order $\hbar$ contributions on the smoothing procedure. This method does not rely on the knowledge of the correction terms, so that it makes the separation of the two contributions of $\hbar$ corrections to the trace formula discussed above possible.

3.3.1 Including oscillating amplitudes

The general procedure to implement smoothing in trace formulae has been derived in Sec. 3.2. The main result is restated here in a notation convenient for a generalization:

For an energy variable $e(E)$ and a trace formula

$$\delta g \;=\; \mathcal{I}m\left[\sum_\Gamma A_\Gamma(e)\, e^{i x_\Gamma(e)}\right] \;=\; \sum_\Gamma A_\Gamma(e)\, \sin[x_\Gamma(e)]\;, \tag{3.22}$$

the smoothing, i. e. the convolution with the line shape function $f(e)$, can be approximated by damping the semiclassical amplitudes with a window function $F(T_\Gamma)$:

$$\delta g^F \;=\; \sum_\Gamma A_\Gamma(e)\, F(T_\Gamma)\, \sin[x_\Gamma(e)] \;\approx\; f(e) * \delta g\;. \tag{3.23}$$

This approximation is only valid for slowly varying real amplitudes. The implementation of two kinds of $\hbar$ corrections to the trace formula for the disk billiard, namely tangent bifurcations and grazing, will lead to oscillating amplitudes. This motivates a generalization of Eq. (3.23) to oscillating real and complex amplitudes.

3.3.1.1 Oscillating real amplitudes

Any real amplitude $A_\Gamma(e)$ can be written as

$$A_\Gamma(e) = M_\Gamma(e)\cdot\cos[\Theta_\Gamma(e)]\;, \tag{3.24}$$

where $\Theta(e)$ is monotonous in e and $M(e)$ is real and does not change sign. Inserting this in Eq. (3.22) and using

$$\sin(x)\cos(\Theta) = \frac{1}{2}[\sin(x-\Theta)+\sin(x+\Theta)]\;, \tag{3.25}$$

the two terms can individually be treated according to Eq. (3.23). This leads to the following smoothing scheme generally applicable to oscillating real amplitudes:

$$\begin{aligned}\delta g^F &= \sum_\Gamma M_\Gamma\,\left[\bar{F}\,\cos(\Theta_\Gamma)\,\sin(x_\Gamma) + \Delta F\,\sin(\Theta_\Gamma)\,\cos(x_\Gamma)\right]\\ &= \sum_\Gamma A_\Gamma\,\bar{F}\,\sin(x_\Gamma) + \sum_\Gamma \Delta F\, M_\Gamma\,\sin(\Theta_\Gamma)\,\cos(x_\Gamma)\;,\end{aligned} \tag{3.26}$$

where

$$\begin{aligned}\bar{F} \;&=\; \frac{F^+ + F^-}{2} \quad;\quad \Delta F = \frac{F^+ - F^-}{2}\;;\\ F^+ = F(x'+\Theta') \quad&;\quad F^- = F(x'-\Theta')\;.\end{aligned} \tag{3.27}$$

The dashes denote the derivatives with respect to e. For slowly oscillating amplitudes ($\Theta' \ll x'$) the second term in Eq. (3.26) is negligible, whereas the first term reproduces the previous result for non-oscillating amplitudes Eq. (3.14). The second term gives a correction depending mainly on Θ', i. e. the frequency of the amplitude oscillation. As expected, this correction is large for rapidly oscillating amplitudes.

3.3.1.2 Special case: Tangent bifurcations

The uniform approximation of the tangent bifurcation according to Eqs. (B.8) and (B.7) leads to the Airy function as semiclassical amplitude. For this special case

$$\delta g = \sum_{\Gamma} Ai(y_\Gamma)\, \sin(x_\Gamma) \tag{3.28}$$

one gets, using Eq. (3.26),

$$\delta g^F = \sum_{\Gamma} \left[\bar{F}\, Ai(y_\Gamma)\, \sin(x_\Gamma) + \Delta F\, Bi(y_\Gamma)\, \cos(x_\Gamma) \right] \ . \tag{3.29}$$

The frequency Θ' can be expressed as

$$\Theta'(e) = \frac{Ai(e)\, Bi'(e) - Ai'(e)\, Bi(e)}{Ai(e)^2 + Bi(e)^2} \cdot y' \ . \tag{3.30}$$

These formulas are used in Sec. 4.3.3 on the treatment of the tangent bifurcations in the disk billiard. There, the corrections to the smoothing scheme (i. e. mainly the second term of Eq. (3.29)) will be seen to be comparable to the corrections stemming from the uniform treatment of the bifurcations. This shows that the correct implementation of the smoothing is vital for an examination of higher-order $\hbar$ contributions to the trace formula.

3.3.1.3 Oscillating complex amplitudes

For oscillating complex amplitudes, Eq. (3.26) can be applied to the real and the imaginary part of A_Γ separately, so that no special treatment has to be introduced. For the special case that the amplitude can be written as

$$A_\Gamma(e) = M_\Gamma(e) \cdot \exp\{i\Theta_\Gamma(e)\} \ , \tag{3.31}$$

the implementation of smoothing is simply given by

$$\delta g^F = \sum_{\Gamma} M_\Gamma\, F^+\, \sin(x_\Gamma + \Theta_\Gamma) \ . \tag{3.32}$$

Note that now both the oscillating term and the damping via the window function F only depend on $x_\Gamma + \Theta_\Gamma$. This is similar to the original formula for slowly varying amplitudes Eq. (3.23).

3.3.1.4 Special case: Grazing

Eq. (3.32) can be used for the Fresnel integrals occurring in grazing corrections (see, e. g., Sec. 4.3.4). Setting

$$\tilde{I}(y) = \left(C(y) - \frac{1}{2} \right) + i \left(S(y) - \frac{1}{2} \right) \ , \tag{3.33}$$

$\tilde{I}$ can be written according to Eq. (3.31). Using Eq. (3.32), some straight-forward calculations show that the smoothing of a trace formula

$$\delta g = \mathcal{I}m \left[\sum_{\Gamma} \left[\mathrm{C}(y_\Gamma) + i\alpha \mathrm{S}(y_\Gamma) \right] e^{i x_\Gamma} \right] \tag{3.34}$$

can be implemented by

$$\delta g^F = \sum_{\Gamma} \left(F^+ \left[C(y)\, \sin(x) + \alpha S(y)\, \cos(x) \right] + \frac{F(x') - F^+}{\sqrt{2}} \sin\left(x + \alpha \frac{\pi}{4} \right) \right), \tag{3.35}$$

where $\alpha = \pm 1$ and $\Theta = \pi/2 \cdot y^2$. Note that now, in contrast to Eq. (3.32), a correction term with an amplitude depending mainly on Θ' shows up.

3.3.2 The folding approach

The smoothing procedure presented above can only be applied if the $\hbar$ corrections can be calculated explicitly. But, as already pointed out, also the neglected (and thus unknown) corrections affect the validity of the amplitude damping ansatz for the implementation of smoothing. This is especially clear for bifurcations: Neglecting bifurcations leads to diverging Gutzwiller amplitudes. In the vicinity of the bifurcation condition Eq. (3.20) of Sec. 3.2 is thus violated. The convolution of the trace sum with the line shape is therefore no longer equivalent to the common amplitude damping. Since at bifurcations the contribution to the trace sum is lower in powers of $\hbar$, the microscopic approach also fails, as the leading-order assumption is not fulfilled.

The simplest technique to separate the direct influence of higher-order $\hbar$-terms on the trace formula from the effects they have on the implementation of smoothing is to perform the smoothing exactly by a numerical convolution with the appropriate line shape. With the plausible assumption that higher-order $\hbar$ contributions do not influence the line shape, this can be taken according to Sec. 3.2 as the Fourier transform of the amplitude damping function. This numerical procedure to implement smoothing in the trace formula will be referred to as *folding approach*.

Both the example of the disk billiard in chapter 4 and the magnetoconductance of the channel with antidots in chapter 7 will show that for systems where many orbits contribute, the dominating effect of bifurcations is not given by the additional terms they introduce in the trace formula, but stems from their influence on the implementation of smoothing. Neglecting the $\hbar$-corrections of the bifurcations in trace formulae, but correctly implementing the smoothing, will prove to be a good approximation in these cases.

3.4 Smoothing for other reasons

Even for systems where no experimental smoothing is relevant,[2] the implementation of a smoothing scheme as presented above might be useful.

A first motivation is given by the mathematical properties of semiclassical trace formulae. In the form used in this work, they exhibit non-trivial convergence properties. From a

[2] See for example the disk billiard in chapter 4, which is only compared to the pure quantum result.

mathematical point of view they cannot be summed up straight-forwardly. This is already clear from the fact that the quantum mechanical single particle level densities are sums of δ-functions. These are not functions in a mathematical sense, but *distributions*, which need special treatment. For various attempts establishing proper resummation schemes of trace formulae see Refs. [111, 101].
If one considers, on the other hand, the smoothed level density, the mathematical problems vanish to a great extent. Calculating the trace formula without smoothing as the limit of vanishing smoothing width allows to ignore the convergence properties of the trace sums within the context of this work.

Another application of smoothing is to cope with the technical limits of a numerical evaluation of the trace formula. Eq. (2.14) consists of a sum over all classical periodic orbits of a system, usually infinitely many. In a numerical approach, this sum has to be truncated. The impact of this truncation can be controlled according to Sec. 3.2 by identifying the cut-off with the window function $F(G)$. Eq. (3.18) thus allows a precise estimate of the error introduced by the truncation in a numerical evaluation.
It is however often more effective to use the relation between smoothing and amplitude damping in the other direction: Given the tolerated numerical effort, the question is how to choose the orbits which are included in the numerical evaluation. This problem is equivalent to the standard problem of Fourier spectroscopy, namely how to get the best spectrum from a finite range of measured intensities. There, special window functions in analogy to Sec. 3.2 are used. There is a large variety of reasonable window-functions at hand. For a detailed discussion see Ref. [43]. There is no optimal window function for all applications, as there is a fundamental trade-off between the width of the peaks and the intensity of spurious sidebands. For the evaluation of the trace formula it is usually convenient to use window functions which already include the (unavoidable) truncation. Choosing a $F(G)$ which is nonzero only in a finite range automatically controls the truncation error. In this work, a triangular window function is used.

The last reason for the implementation of a smoothing scheme like Eq. (3.18) is closely related to the problem of the numerical evaluation of trace formulae mentioned above. For any given window function (which may be only due to the truncation scheme implemented), the expected line width and line shape can be calculated. This method provides the basis for a very precise numerical calculation of the semiclassical single-particle energies. For details see Sec. 4.6 of Ref. [1]. In Ref. [2] this ansatz was used to prove the identity of the EBK and the Gutzwiller result for the disk billiard numerically.

Chapter 4

The disk billiard

The disk billiard in homogeneous magnetic fields is used as a model system for semiclassical approximations. Its quantum mechanical level density can be calculated analytically. Therefore, a precise comparison of the semiclassical approach to the exact result is possible. The influence of various $\hbar$-corrections to the trace formula is examined. With the help of the trace formula's close relation to classical dynamics it is possible to give a simple, intuitive picture explaining all features of the level density.

Contents

The trace formula is a relatively new technique in mesoscopic physics. The experience with the approach is therefore rather limited. The application of this method to a simple, well-known model system has three motivations: First, it is desirable to test the new ansatz on a non-trivial, but well-known reference system to learn about the limitations of the method. So the second goal considering a model system is to find out under which circumstances specific corrections in higher order of $\hbar$ become relevant. Finally, in cases where these corrections are not negligible, the challenge is to improve the semiclassical ansatz, i.e. to include the relevant corrections in a generalized trace formula.

The semiclassical description of the disk billiard in homogeneous magnetic fields is therefore worked out not *although* the problem can be solved exactly, but *because* it can. The three goals formulated above will serve as a guiding line through the following sections.

4.1 Exact quantum solution

The disk billiard in homogeneous magnetic fields is integrable. The two constants of motion are the angular momentum and the energy. In the following, normalized energies $\widetilde{E}$ in units of

$$E_0 = \frac{\hbar^2}{2mR^2} \tag{4.1}$$

and normalized magnetic fields $\widetilde{B}$ in units of $\hbar/eR^2$ will be used. With the disk radius R and the wavenumber k the normalized energy is given by $\sqrt{\widetilde{E}} = kR$. The classical cyclotron radius is given by $R_c = \hbar k/eB$, and in normalized units by $R_c/R = kR/\widetilde{B}$. The exact solution for the eigenenergies was presented by Geerinckx [31] and, using a different approach, by Klama *et al.* [49]:

$$\widetilde{E}_{nl} = 2\widetilde{B} \cdot \left(\alpha_{nl} + \frac{1+|l|}{2} + \frac{1}{2} \right) , \tag{4.2}$$

where the α_{nl} are the zeros of the confluent hypergeometric function ${}_1F_1$

$${}_1F_1\left(-\alpha_{nl}; 1+|l|; \frac{\widetilde{B}}{2} \right) = 0 . \tag{4.3}$$

Here $n > 0$ denotes the radial and l the angular-momentum quantum number. For $B = 0$ the eigenvalue equation simplifies to the well-known result $\widetilde{E}_{nl} = (j_{nl})^2$, where j_{nl} are the zeros of the Bessel functions $J_l(j_{nl}) = 0$. For the details of the numerical evaluation, I refer to my Diploma thesis [1]. Fig. 4.1 shows the dependence of the eigenvalues $\widetilde{E}_{nl}$ on $\widetilde{B}$. One clearly sees how with increasing magnetic field the different states condense into the Landau levels (dashed lines).

4.2 The leading order in $\hbar$: Standard semiclassics

The standard Gutzwiller approach [36, 37, 38, 39, 40] is limited to orbits which are isolated in phase space. Therefore it cannot be applied to the disk with its continuous rotational

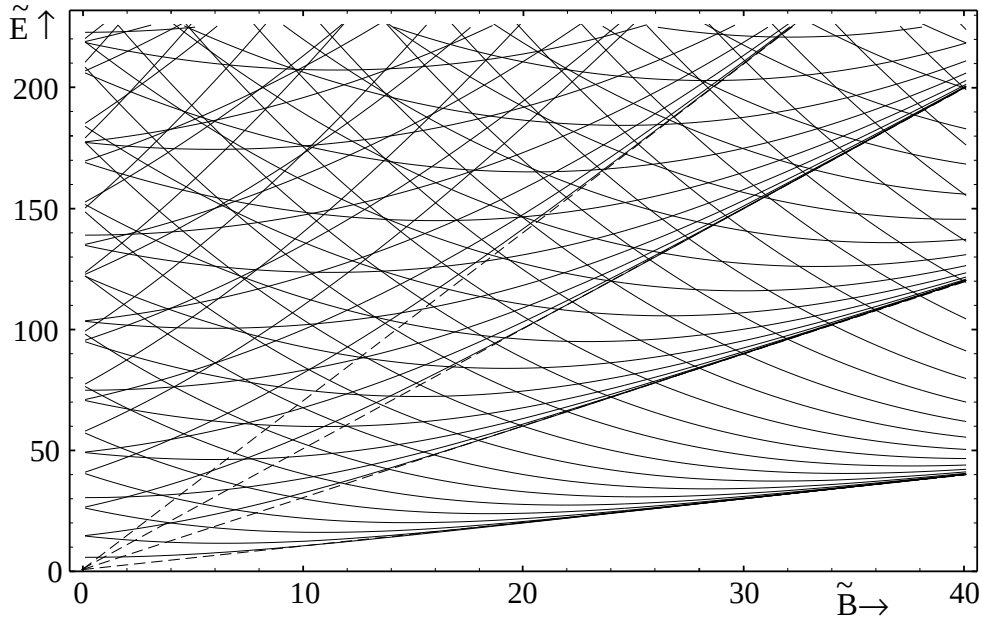

Figure 4.1: *The quantum-mechanical eigenenergies of the circular billiard in dependence of the magnetic field. The dashed lines correspond to the four lowest Landau levels.*

symmetry. Deriving a trace formula requires the extensions of Strutinisky and Magner [76] or Creagh and Littlejohn [23]. This has been done for the zero-field case by Reimann *et al.* [2] and, independently, by Tatievski *et al.* [79]. Equivalent results have been obtained by Balian and Bloch [11]. Von Oppen [123] followed the approach of Berry and Tabor [13], which starts from the EBK quantization of the system [46]. Via Poisson resummation and subsequent saddle point approximations he derived a trace formula equivalent to the modified Gutzwiller approach. This result shows that EBK and the modified Gutzwiller approximation are identical in the leading order of $\hbar$. Since the intermediate steps of the calculation include saddle-point approximations, the identity does not necessarily hold beyond the leading order. In a previous work I was, however, able to show numerically with high accuracy that the Gutzwiller-like trace formula reproduces exactly[1] the single-particle energies of the EBK quantization. For details see Refs. [2, 1].

For weak magnetic fields, the circular billiard was treated using a perturbative approach by Bogachek and Gogadze [15], Ullmo *et al.* [82] and Reimann *et al.* [62].

4.2.1 Trace formula for arbitrarily strong fields

The generalization of the Gutzwiller trace formula to systems with continuous symmetries by Creagh and Littlejohn is a convenient starting point for the semiclassical description of the level density of a circular billiard in arbitrarily strong magnetic fields. For the application of this generalized trace formula, the periodic orbits have to be classified and their actions, amplitudes, and Maslov indices have to be calculated. This was the topic of my diploma thesis [1]. Since these results provide the basis for the subsequent calculations, they will be shortly reviewed in the following.

[1] This has to be interpreted as a very fortunate case, comparable to the harmonic oscillator. There all $\hbar$ corrections vanish, and the semiclassical approximation is therefore exact [18].

4.2.1.1 Classification of the periodic orbits

The classification of the periodic orbits in the system is straightforward. In zero field, the periodic orbits (PO) of a circular billiard are equivalent to those in a three-dimensional spherical cavity. The complete classification of those has already been given by Balian and Bloch [11]. The only difference to the three-dimensional case is that the orbits in the disk billiard only have a one-dimensional degeneracy, corresponding to the rotational symmetry of the system. Each family of degenerate orbits with a given action can be represented by a regular polygon. The first few polygons are shown in Fig. 4.2. These

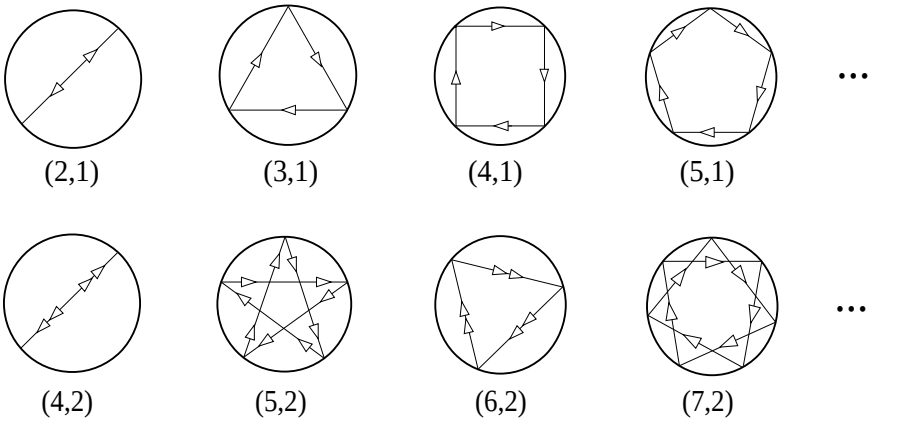

Figure 4.2: *The classical periodic orbits of the circular billiard in zero field are the regular polygons. They can be classified with (v, w), where v is the number of corners and w indicates how often the trajectory winds around the center.*

orbit families are classified by $\beta = (v, w)$, where v denotes the number of corners (vertices), and w is the winding number, i. e., it counts how often an orbit winds around the center of the disk. With $v \geq 2w > 2$ ($v, w \in \mathbb{N}$), all families of POs of the system in the absence of a magnetic field are uniquely described by $\beta = (v, w)$. Because of the time-reversal symmetry, all orbits except the diameter ($v = 2w$) have an additional discrete two-fold degeneracy, which has to be accounted for in the trace formula.

Switching on the magnetic field causes the classical trajectories to bend, the direction of the curvature depending on the direction of motion with respect to the magnetic field. This entails a breaking of time-reversal symmetry. For weak fields, the orbits can still be classified by β if an additional index ($\pm$) is introduced. This situation is shown in the upper row of diagrams in Fig. 4.3 for the orbit $\beta = (4, 1)$. Up to a field strength where the

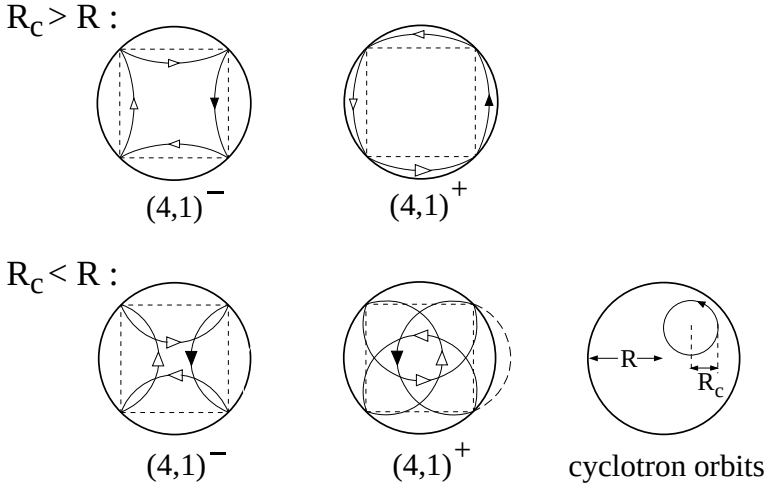

Figure 4.3: *A magnetic field breaks the time-reversal symmetry, so that the orbits are no longer independent of the direction of motion. Introducing an additional index $\pm$, the orbits can be classified by $(v, w)^{\pm}$, both in weak ($R_c > R$) and in strong ($R_c < R$) fields. For strong fields an additional family of orbits occurs. These are the cyclotron orbits, which do not touch the boundary.*

classical cyclotron radius R_c equals the disk radius R, henceforth referred to as the *weak-field regime*, the orbits do not change their topology and the classification $\beta^{\pm}$ holds. For the *strong-field regime* with $\widetilde{B} > kR$, the structure of the POs is different. This situation is shown in the second row of diagrams in Fig. 4.3. The β^- orbits vary their shapes continuously over the point $R_c = R$, but the topologies of the β^+ orbits change abruptly. However, since there is a one-to-one correspondence between orbits for $R_c \gtrsim R$ and for $R_c \lesssim R$, $\beta^{\pm}$ still gives a complete classification of all *bouncing orbits*, i. e., of orbits that are reflected at the boundary. For $R_c < R$, there are additional *cyclotron orbits* which do not touch the boundary at all. They have to be included additionally in the sum over all orbits in the trace formula. At field strengths where $R_c \leq R \cdot \sin(\pi w/v)$, the $(v,w)^{\pm}$ orbits no longer exist (see Fig. 4.4). They vanish pairwise in a tangent bifurcations. This imposes

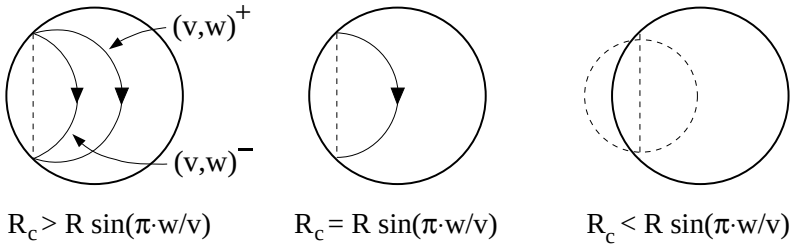

Figure 4.4: *At a magnetic field strength where $R_c = R\sin(\pi\ w/v)$, the orbits $(v,w)^{\pm}$ vanish pairwise in tangent bifurcations.*

an additional restriction on the sum over (v,w). Including this finally yields a complete classification of all periodic orbits in the circular billiard at arbitrary field strengths.

4.2.1.2 The bouncing orbits

The action of a closed orbit in a magnetic field can be written as the sum of the kinetic part and the magnetic flux enclosed by the orbit

$$S_\beta = \int p\,\mathrm{d}q = \hbar k L_\beta - eBF_\beta\ . \tag{4.4}$$

The enclosed areas F_β of the periodic orbits discussed above (correctly counting those areas that are enclosed several times, cf. Fig. 4.5) as well as their geometrical lengths L_β

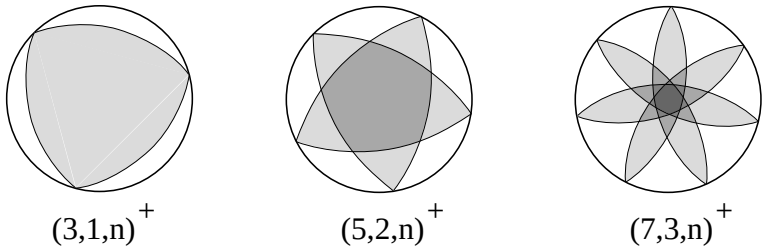

Figure 4.5: *Calculating the magnetic flux enclosed by an orbit, the multiple enclosed areas (darker gray) have to be correctly accounted for.*

can be calculated by elementary geometry. In terms of the geometrical quantities R_c, R, γ and Θ explained in Fig. 4.6 they are given by

$$S_\beta(E) \quad = \quad v\hbar k R_c \eta\ , \tag{4.5}$$

$$\eta = \begin{cases} \gamma + \frac{\sin 2\gamma}{2} - \left(\frac{R}{R_c}\right)^2 \frac{\sin 2\Theta}{2} & \text{for } (\beta^+, R_c \geq R) \\ \pi - \gamma - \frac{\sin 2\gamma}{2} + \left(\frac{R}{R_c}\right)^2 \frac{\sin 2\Theta}{2} & \text{for } (\beta^+, R_c \leq R) \\ \gamma + \frac{\sin 2\gamma}{2} + \left(\frac{R}{R_c}\right)^2 \frac{\sin 2\Theta}{2} & \text{for } (\beta^-) \end{cases} .$$

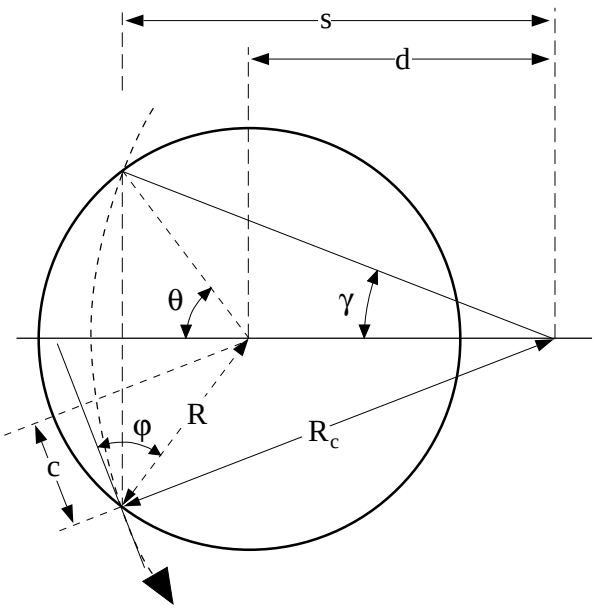

Figure 4.6: *The actions and amplitudes of the classical periodical orbits can be expressed in terms of the geometrical quantities shown in this figure.*

According to the trace formula Eq. (2.15), the orbit amplitudes include an integral over the symmetry group. For the rotational $U(1)$ symmetry of the disk this integral just gives $2\pi/v$. The remaining factors in the amplitude are the period of the orbit $L/\hbar k$, and the Jacobian resulting from the symmetry reduction $\mathrm{d}L/\mathrm{d}\Psi$, where $\Psi = -2n\Theta$. All these quantities can be calculated analytically, resulting in

$$\begin{aligned} A_\beta &= \frac{1}{E_0}\frac{1}{\sqrt{Rk\pi}}\frac{1}{\sqrt{v}}\frac{R_c}{R}\sqrt{\frac{cd}{sR}}\,\xi_\beta , \\ \xi_\beta &= \begin{cases} \pi - \gamma & \text{for } (\beta^+, R_c < R) \\ \gamma & \text{otherwise} \end{cases} , \end{aligned} \tag{4.6}$$

where c, d, and s are the geometrical lengths sketched in Fig. 4.6. The dependence of these geometrical quantities on the classification parameter $\beta^\pm$ and the cyclotron radius R_c is given by

$$\begin{aligned} \Theta &= \frac{w}{v}\pi , \\ \gamma &= \arcsin\left(\frac{R}{R_c}\sin\Theta\right) , \\ \varphi &= \begin{cases} \gamma - \Theta + \pi/2 & \text{for } (\beta^+, R_c > R) \\ -\gamma + \Theta + \pi/2 & \text{for } (\beta^+, R_c < R) \\ \gamma + \Theta - \pi/2 & \text{for } (\beta^-) \end{cases} , \\ c &= R\cos\varphi , \\ s &= \sqrt{{R_c}^2 - R^2\sin^2\Theta} , \\ d &= \begin{cases} |s - R\cos\Theta| & \text{for } \beta^+ \\ s + R\cos\Theta & \text{for } \beta^- . \end{cases} \end{aligned} \tag{4.7}$$

4.2.1.3 Cyclotron orbits

As already mentioned above, a new class of orbits occurs for $\widetilde{B} > kR$. These are the *cyclotron orbits*, which do not touch the boundary at all (see Fig. 4.3). They form translationally degenerate families, whereas the bouncing orbits $(v, w)^\pm$ considered above are

degenerate with respect to rotations. For the translational case, the symmetry reduction can be performed directly, without need for the general procedure of Creagh and Littlejohn. Therefore, the the phase-space coordinates are transformed according to

$$\pi_x := \frac{1}{\sqrt{|eB|}}\left(p_x + \frac{eB}{2}y\right) , \qquad \Pi_x := \pi_y + \sqrt{|eB|}\, x ,$$
$$\pi_y := \frac{1}{\sqrt{|eB|}}\left(p_y - \frac{eB}{2}x\right) , \qquad \Pi_y := \pi_x - \sqrt{|eB|}\, y . \tag{4.8}$$

Π_x and Π_y are canonically conjugate variables, since $[\Pi_x, \Pi_y] = i\hbar$. The same holds for π_x and π_y. Apart from the factor $\sqrt{|eB|}$, (π_x, π_y) are the coordinates of the motion relative to the center of gyration (Π_x, Π_y), as illustrated in Fig. 4.7. In these coordinates the Hamiltonian reads

$$H = \frac{eB}{2m}(\pi_x^2 + \pi_y^2) . \tag{4.9}$$

As expected, H does not depend on the coordinates of the center of gyration. Because the relative and the center-of-gyration coordinates commute, i. e., $[\Pi_x, \pi_x] = [\Pi_x, \pi_y] = [\Pi_y, \pi_x] = [\Pi_y, \pi_y] = 0$, the degeneracy of a cyclotron orbit is proportional to the phase-space volume V accessible for (Π_x, Π_y). This can be directly read off Fig. 4.7 (shaded area). The degeneracy is therefore given by

$$N = \frac{V}{2\pi\hbar} = \frac{\tilde{B}}{2}\left(1 - \frac{R_c}{R}\right)^2 . \tag{4.10}$$

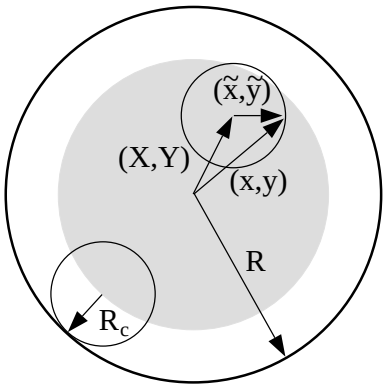

Figure 4.7: *The motion of a charged particle in a homogeneous magnetic field can be expressed in the coordinates of the relative motion* $(\tilde{x}, \tilde{y}) = |eB|^{-1/2}(-\pi_y, \pi_x)$ *and the coordinates of the center of gyration* $(X, Y) = |eB|^{-1/2}(\Pi_x, -\Pi_y)$. *The Hamiltonian is independent of* (Π_x, Π_y)*; all orbits with the center* (X, Y) *in the gray shaded area are degenerate.*

The Hamiltonian Eq. (4.9) is identical to that of a one-dimensional harmonic oscillator. Using its analytical trace formula,[2] the contribution of the cyclotron orbits to the oscillating part of the level density can be written as

$$\delta g^c = \frac{1}{2E_0}\left(1 - \frac{R_c}{R}\right)^2 \sum_{n=1}^{\infty} \cos(nk\pi R_c - n\pi) . \tag{4.11}$$

Here n is the winding number around the center of gyration. The frequency is again determined by the classical action along the orbit, which in this case is

$$S = n \cdot \hbar k \cdot \pi R_c . \tag{4.12}$$

Note that here exactly half of the kinetic contribution to the action is canceled by the flux term.

[2]The one dimensional harmonic oscillator is one of the few cases that can be treated exactly within standard POT [18].

4.2.1.4 Additional phases

The additional phases σ in the trace formula (2.15) are discussed in Sec. 4.3.2.1. There, the Maslov index μ is found to be $\mu = 3v$ for bouncing orbits and $\mu = 2$ for cyclotron orbits. The additional phase of $\delta \cdot \pi/2$ stemming from the symmetry reduction is given by

$$\delta = \begin{cases} 0 & \text{for } (\beta^+, R_c < R) \\ 1 & \text{otherwise} \end{cases} . \tag{4.13}$$

Now for all quantities of the trace formula analytical expressions have been derived. Inserting them in Eq. (2.15), the semiclassical level density for the disk billiard in homogeneous magnetic fields can be evaluated.

4.2.2 Numerical evaluation

The infinite trace sum Eq. 2.15 has to be truncated in a numerical evaluation. The implications of this truncation have been discussed in Sec. 3.4. To ensure the convergence of the sum and the comparability with the quantum results as well as to control the truncation errors, the considerations of Sec. 3.2 will now be applied to the trace formula of the disk billiard.

As discussed on page 20, the natural choice for the generalized energy in billiard systems is k. According to Eq. (3.21) the quasiperiod is then given by the geometrical orbit length

$$L = vR_c \cdot \begin{cases} 2\pi - 2\gamma & \text{for } (\beta^+, R_c < R) \\ 2\gamma & \text{otherwise} \end{cases} . \tag{4.14}$$

Note that for weak fields ($R_c > R$) L is independent of the direction of motion $\pm$.

To compute the trace formula, an appropriate window function $F(L)$ has to be selected. For this choice two criteria are relevant: First, $F(L)$ should be nonzero only in a finite range of L, so that many terms in the trace formula are eliminated and the numerical evaluation is simplified. Second, the window function should have an analytical Fourier transform to enable an easy and accurate comparison with the quantum results. Either of these conditions is met by the usual Gaussian smoothing, where the orbits are suppressed with increasing length L according to $\exp\{-(L/L_0)^2\}$. In this work a triangular window is used instead, which matches both demands. In order to make the results comparable with the usual Gaussian smoothing, the window function is characterized with a parameter $\tilde{\gamma}$. It corresponds to the variance of a Gaussian smoothing $\exp\{-1/2(k/\tilde{\gamma})^2\}$ with the same half-width.

Since the trace formula should be evaluated via Eq. (3.14), the compliance of conditions Eqs. (3.19) and (3.20) has to be checked. These depend on the behavior of the amplitudes which are plotted in Fig. 4.18. As already discussed, the orbit amplitudes diverge at the bifurcations, so that Eq. (3.20) is violated at these points. This problem will be treated together with the inclusion of the bifurcations in Sec. 4.3.3. Except in the vicinity of bifurcations, the conditions (3.19) and (3.20) are fulfilled, so that Eq. (3.14) is applicable. For the cyclotron orbits discussed in Sec. 4.2.1.3, $G = n \cdot 2\pi R_c$ and $A = (2E_0)^{-1}(1-R_c/R)^2$. This amplitude is slowly varying in the whole energy range. For the cyclotron orbits, approximation (3.18) is therefore justified for all $\widetilde{E}$ and $\widetilde{B}$.

Putting everything together, this establishes a numerical scheme for the evaluation of the semiclassical trace formula for the circular billiard.

4.2.3 Results of the trace formula

The results of the trace formula for the disk billiard in homogeneous magnetic fields will only be discussed insofar as they are relevant for the present work. Further details can be found in my Diploma thesis [1] or in Ref. [4].

For zero field, the trace formula leads to an exact quantization at the EBK eigenvalues [2]. In the weak-field limit the trace formula can be approximated by replacing the amplitudes of Eq. (4.6) by their asymptotic values for $\widetilde{B} \to 0$ and expanding the actions of Eq. (4.5) up to first order in $\widetilde{B}$. This reproduces, as expected, the perturbative results of Bogachek *et al.* [15] and Reimann *et al.* [62].

The result for the shell structure (i. e. the coarse-grained level density) in comparison to the exact quantum mechanical result is displayed in Fig. 4.8. For $R_c > R$, the agreement

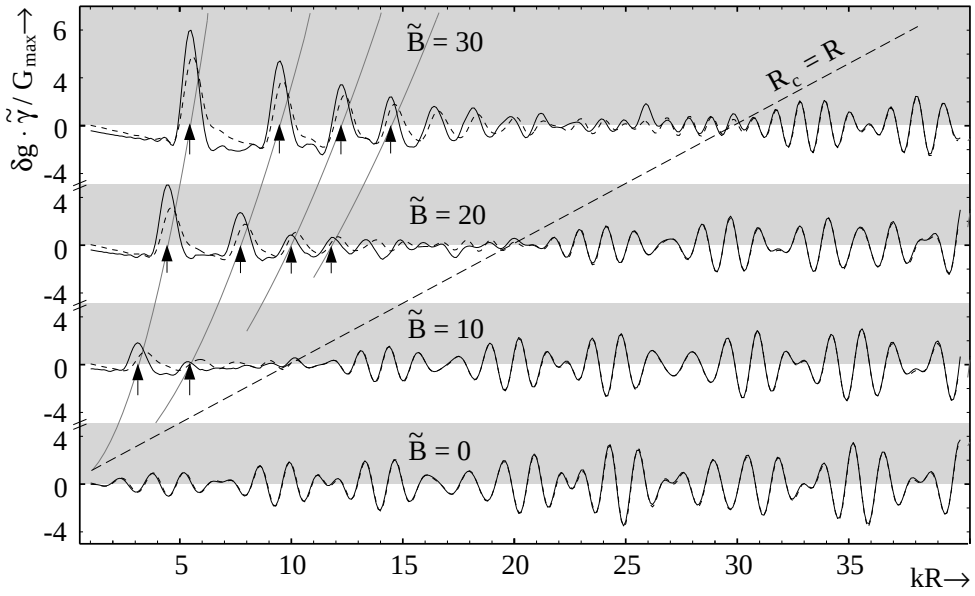

Figure 4.8: *The semiclassical level density of the disk billiard (solid) compared to the equivalently smoothed quantum-mechanical result (dashed). The smoothing width is $\tilde{\gamma} = 0.35$. Gray lines and the arrows indicate the positions of the first four Landau levels. In weak fields ($R_c > R$) the semiclassical result is in excellent agreement with the exact solution, for strong fields ($R_c \lesssim R$) the agreement is not satisfactory.*

with the exact quantum mechanical result is excellent. In the strong-field regime $R_C \lesssim R$, however, the agreement is not satisfactory. The positions of the Landau levels are reproduced, but their degeneracy is overestimated in the semiclassical approximation. In the extreme field limit ($R_c \ll R$) the Landau states dominate the level density. In this regime the cyclotron orbits dominate, since their degeneracy prefactor Eq. (4.10) grows linearly in B. As shown in Sec. 4.2.1.3, the cyclotron orbits can be analytically transformed to a harmonic oscillator. Thus, the semiclassical description of these orbits is *exact*. For extremely strong fields, the trace formula is therefore again a good approximation.

The same results have also been obtained for the full quantization of the system [1, 4]. To summarize, both the shell structure and the full quantization, in weak as well as in extremely strong fields, are well approximated by the semiclassical method. The regime $R_c \lesssim R$, however, is poorly reproduced by the trace formula.

4.3 Beyond the leading order: $\hbar$ corrections

4.3.1 The inherent $\hbar$ problem in the disk billiard

As explained in the previous section, a new class of periodic orbits appears in strong magnetic fields. These are the cyclotron orbits, which exist only for $\widetilde{B} > kR$. Whereas the bouncing orbits have a one-dimensional rotational symmetry, the cyclotron orbits are two-dimensionally translationally degenerate. The application of Creagh's trace formula Eq. (2.15) leads to contributions in $\hbar^{-3/2}$ stemming from the bouncing orbits. The cyclotron orbits, however, have a prefactor $\hbar^{-2}$. Even though the trace formula is derived as the leading-order contribution in $\hbar$, its application to the disk billiard results in terms of different orders in $\hbar$.

The inherent $\hbar$ problem of the disk billiard is that these different powers in $\hbar$ are indeed necessary to describe the level density of the system. The leading order in $\hbar$ is given by the contributions of the cyclotron orbits. These describe the Landau levels correctly, which dominate the level density in the extreme strong field limit. At weak fields, however, $R_c > R$ and the trace formula only consists of the bouncing orbits.

In the two limits where one order in $\hbar$ is dominant, i. e. the extreme and the weak field limit, the trace formula was seen to be a good approximation. In the strong field regime ($R_c \lesssim R$) different powers in $\hbar$ become relevant, and the semiclassical description is not satisfactory (cf. Fig. 4.8). This observation is surprising, since the transition between the limiting cases is mainly governed by the smoothly varying degeneracy prefactor of the cyclotron orbits. The origin of the discrepancy between the semiclassical and the quantum result in the strong field regime needs further investigation.

Formally, the bouncing orbits give rise to an $\hbar$ correction in this regime – but, as we have just seen, they cannot be neglected. This naturally rises the question whether other $\hbar$ corrections are also relevant for the semiclassical description of this system. The following sections select various $\hbar$ corrections from physical and mathematical arguments and examine their influence. These investigations will finally show that all relevant effects can be described in a simple, intuitive picture. More mathematically motivated corrections will be of negligible influence. This is very convenient from an applicant's point of view, since the necessary modifications to the trace formula remain simple, and more involved $\hbar$ corrections are irrelevant for practical applications. A theorist, however, might be disappointed by the fact that all the elaborate lengthy formulas have so little influence in the end.

4.3.2 Reflection phases

The calculation of corrections to the Maslov index is motivated by two observations: First, a close look at the shell structure in Fig. 4.8 as well as at the corresponding full quantization data shows that the semiclassical approximation overestimates the degeneracy of the Landau levels, and completely misses the levels slightly higher in energy. A simple hand-waving argument links this behavior to a boundary effect: Quantum mechanically, a particle moving on a cyclotron orbit will feel the boundary even if classically not touching it. Particles on cyclotron orbits close to the boundary thus feel an additional confinement. This restriction to a smaller volume will lead to a higher energy. In this picture, not all the cyclotron orbits are degenerate. The orbits close to the boundary no longer have the

energy of the Landau level, but a slightly higher one. This corrects the observed defects of the semiclassical approximation. The boundary properties enter the standard trace formula only via the Maslov index, so that a correction of μ is indicated.

The second observation motivating a closer examination of the Maslov index can be illustrated with the diameter orbit. It exists only in the weak-field regime and develops into a cyclotron orbit at $R_c = R$. The action and the period change smoothly over this point, but the Maslov index does not: It is 4 for the bouncing, and 2 for the cyclotron orbit. A correction to the Maslov index should remove this spurious jump.

In my Diploma thesis [1], I suggested an $\hbar$-correction to the Maslov index, i. e. replacing it with a more sophisticated quantity explicitly depending on $\hbar$. This section will summarize the ansatz together with the main results.

4.3.2.1 The Maslov index

The origin of the Maslov index can most easily be understood in the one-dimensional case. As presented in more detail in Sec. 2.1, the semiclassical approach approximates the wave functions by plane waves with the local wave number $k(x) = \sqrt{2m[E - V(x)]}$. This approximation obviously breaks down at the classical turning points where $E = V(x)$, so that the wavelength diverges. Expanding the wave function around the classical turning points and matching them to the plane-wave solutions far from the turning points leads to additional phases in the semiclassical quantization. In the limit $\hbar \to 0$ these are independent of the detailed shape of the potential. Each reflection at a soft[3] turning point gives a phase of $-\pi/2$, whereas each reflection at an infinitely steep wall gives a phase of $-\pi$. These phases (in units of $\pi/2$) are the Maslov indices.

In the case of the disk billiard, the Maslov index can be obtained by counting the classical turning points of the one-dimensional effective potential in the radial variable r. For skipping orbits, the Maslov index per bounce is 3, including one soft reflection at the centrifugal barrier and one hard-wall reflection. For the cyclotron orbits, the effective potential is a one-dimensional harmonic oscillator (see Sec. 4.2.1.3) with two soft turning points, and thus their Maslov index per period is 2. In higher dimensions, the Maslov index is less accessible to intuition. It can be described as a topological index characteristic for an orbit. Its calculation for two-dimensional systems is described in appendix A.2.3. For higher dimensions see e. g. Refs. [22, 66].

4.3.2.2 Reflection phases

For finite $\hbar$ the additional phases stemming from classical turning points depend on the shape of the potential. This can be easily understood considering a cyclotron orbit at a distance x_w from the billiard boundary. Neglecting the curvature of the boundary (which corresponds to the strong-field limit), the motion in the presence of the wall can be reduced to an effective 1D motion just as presented in Sec. 4.2.1.3. This is shown in Fig. 4.9. The upper row of diagrams shows the 2D motion, the lower row gives the reduction to the one-dimensional motion in an effective potential. Figure 4.9 (a) shows the unbounded case, in (b) the orbit is near the boundary, and (c, d) illustrate skipping orbits.

[3] In this context "soft" means that the slopes of the potential at the classical turning points are finite.

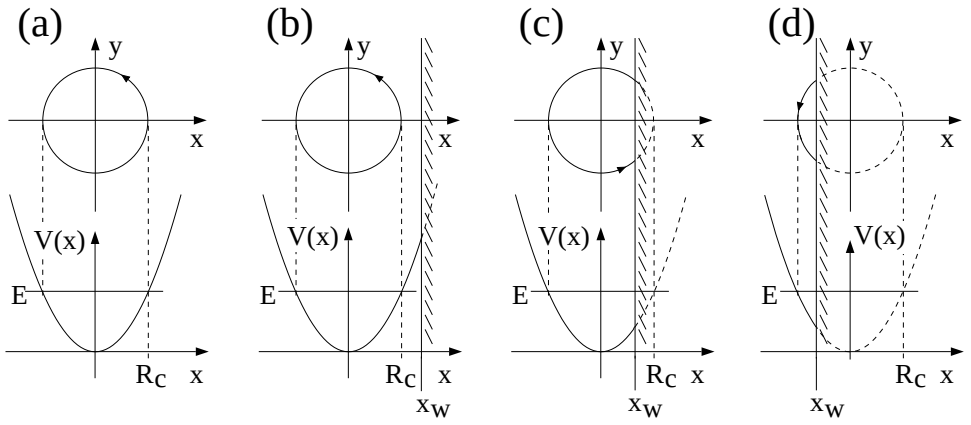

Figure 4.9: *The cyclotron orbit is equivalent to the motion in a one-dimensional harmonic oscillator (a). Neglecting its curvature, the billiard boundary can be implemented in the effective one-dimensional motion (b)-(d).*

A particle in the potential sketched in Fig. 4.9(b) is classically not influenced by the additional wall, since it will never touch it. Quantum mechanically, however, the wave function enters the classically forbidden region and thus feels the boundary even for $x_\mathrm{w} > R_c$. This leads to a smooth transition of the quantum-mechanical reflection phase φ_R over $x_\mathrm{w} = R_c$. The semiclassical Maslov phase, in contrast, is discontinuous at this point. As explained in Sec. 4.3.2.1 above, it is $-\pi$ for $x_\mathrm{w} > R_c$ and $-3/2\pi$ for $x_\mathrm{w} < R_c$. The quantum mechanical boundary effects can be implemented in the semiclassical trace formula by replacing $\mu\pi/2$ by the reflection phase φ_R of the corresponding one-dimensional motion. This smooth version of the Maslov phase will also remove the former clear separation between cyclotron orbits and skipping orbits. These two limiting cases are now continuously linked, with φ_R ranging between $-\pi$ and $-3\pi/2$. We will refer to the orbits in the transition region, which are close to the boundary within $\hbar$, as to the *grazing orbits*.

In this approximation the calculation of the reflection phases is reduced to the problem of the one-dimensional harmonic oscillator in an additional square-well potential. The approach chosen in my Diploma thesis [1] was to integrate the quantum-mechanical problem numerically and calculate the reflection phases φ_R from the solutions. Alternatively to this numerical approach, an analytical approximation of the reflection phase is possible. For a linear potential, the Schrödinger equation can be solved analytically. Matching the solutions with the boundary condition yields an expression of the reflection phases in terms of Airy functions:

$$\varphi_R = \begin{cases} -2\left(\frac{\pi}{4} + \arctan\left[\frac{A_i(X)}{B_i(X)}\right]\right) & \text{for } X \geq 0 \\ -2\left(\frac{\pi}{4} + \arctan\left[\frac{A_i(-X)}{B_i(-X)}\right] - \frac{2}{3}|X|^{2/3}\right) & \text{for } X < 0\,. \end{cases} \tag{4.15}$$

Expanding the potential at the turning point to linear order, these reflection phases can be used for arbitrary potential shapes. In this approximation, X is given by

$$X = \left(\frac{3}{2}\int_T^W \sqrt{|E - V(x)|}\, dx\right)^{2/3}\,, \tag{4.16}$$

with the classical turning point T and the position of the hard wall W. For the harmonic oscillator considered above, one finds explicitly

$$X = \begin{cases} \left[\frac{3}{4}\sqrt{\widetilde{E}}\left(\quad \widetilde{x}_{\mathrm{w}}\sqrt{\widetilde{x}_{\mathrm{w}}^2-1} - \operatorname{arcosh}(\widetilde{x}_{\mathrm{w}})\right)\right]^{(2/3)} & \text{for } |\widetilde{x}_{\mathrm{w}}| \geq 1 \\ -\left[\frac{3}{4}\sqrt{\widetilde{E}}\left(\frac{\pi}{2} - |\widetilde{x}_{\mathrm{w}}|\sqrt{\widetilde{x}_{\mathrm{w}}^2-1} - \arcsin(|\widetilde{x}_{\mathrm{w}}|)\right)\right]^{(2/3)} & \text{for } |\widetilde{x}_{\mathrm{w}}| < 1\,, \end{cases} \tag{4.17}$$

where $\widetilde{x}_{\mathrm{w}} := x_{\mathrm{w}}/R_c$. An equivalent approach to the reflection phase was used in a different context by Isihara and Ebina [44].

The corrections to the Maslov index obtained from the numerical approach and the analytic approximation of the reflection phase are equivalent within the context of this work. Fig. 4.10 shows the result of the quantum mechanical calculation for the reflection phase φ_R. As expected, the transition from $-\pi$ at $x_{\mathrm{w}} \gg R_c$ to $-3/2\pi$ at $x_{\mathrm{w}} \ll R_c$ is smooth. The transition gets sharper if $(kR)^2/\widetilde{B}$ increases. For $(kR)^2/\widetilde{B} \to \infty$, which corresponds to the semiclassical limit $\hbar \to 0$, the standard Maslov phase (thick line) is reproduced. Fig. 4.10 shows that quantum corrections have the greatest influence on the grazing orbits ($x_{\mathrm{w}} \approx R_c$) and on orbits with $x_{\mathrm{w}} \gtrsim -R_c$. The latter are known as the *whispering gallery* orbits, as they move in a narrow region along the boundary.

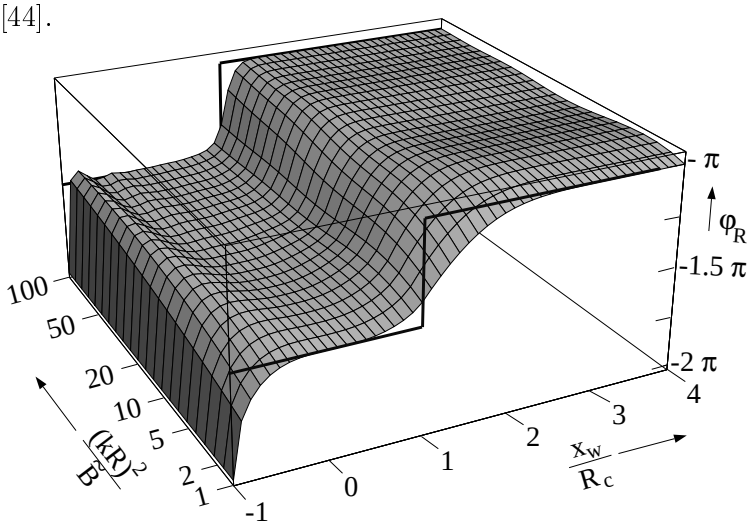

Figure 4.10: *The reflection phase φ_R in dependence of the distance of the center of gyration from the boundary x_{w}. The transition from $x_{\mathrm{w}} < R_c$ to $x_{\mathrm{w}} > R_c$ is continuous and gets sharper for increasing $(kR)^2/\widetilde{B}$. In the limit $(kR)^2/\widetilde{B} \to \infty$, which corresponds to the semiclassical limit $\hbar \to 0$, the Maslov phase (thick line) is recovered.*

4.3.2.3 Comparison to the quantum-mechanical result

Fig. 4.11 depicts the semiclassical shell structure calculated with reflection phases in the whole range from zero field to full Landau quantization (solid). The comparison with the exact quantum result (dashed) shows that the semiclassical approximation is now valid for arbitrarily strong fields, in contrast to the standard trace formula result displayed in Fig. 4.8. Especially the degeneracies of the Landau levels are now reproduced correctly. This shows that the replacement of the Maslov index by the reflection phase is an important correction in the intermediate strong field regime. The reflection phase explicitly depends on $\hbar$, so that the inclusion of this term formally corresponds to a correction in higher than leading order in $\hbar$.

Some bifurcations of important orbits are marked with vertical lines in Fig. 4.11. The quality of the semiclassical approximation is excellent even at these points, where the semiclassical trace formula is expected to diverge. This apparent contradiction will be explained in the following section. There, the bifurcations will be included in the trace

formula, and the influence of the corresponding $\hbar$ correction will be analyzed for the various field regimes.

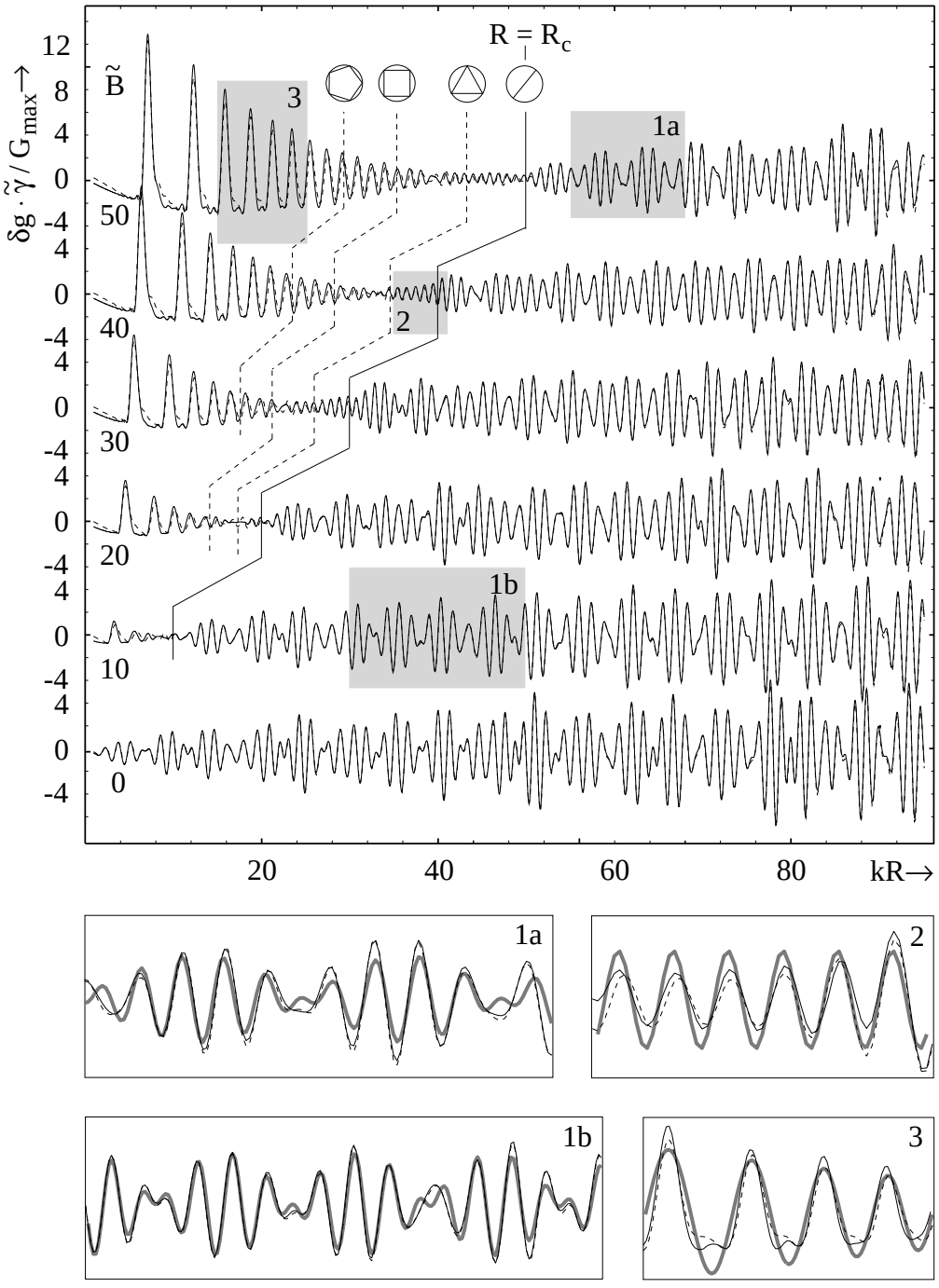

Figure 4.11: *The semiclassical coarse-grained* ($\widetilde{\gamma} \approx 0.35$) *level density of the disk billiard with corrected reflection phases (solid) compared to the equivalently smoothed quantum-mechanical result (dashed). The agreement is excellent in the whole range of energies, disk radii, and magnetic fields. The vertical lines indicate the bifurcation points of the most important orbits. The shaded regions are enlarged in the figures below. The thick gray lines correspond to the interpretation of the level density as given in Sec. 4.4.*

4.3.3 Bifurcations

In the disk billiard, the orbits $(v, w)^{\pm}$ vanish pairwise with increasing magnetic field (or decreasing energy) in *tangent bifurcations* (see Fig. 4.4). This type of bifurcation was already introduced in Sec. 2.4. Due to the continuous symmetry of the disk billiard, the integration considered there has to be performed over the angular momentum L instead of r, but apart from that the schematic behavior of Fig. 2.1 is directly recovered. Fig. 4.12 shows the situation for the triangular[4] orbits. The stationary points of $S(L)$ in the first row correspond to the periodic orbits plotted below. Fig. 4.12(A) shows the generic

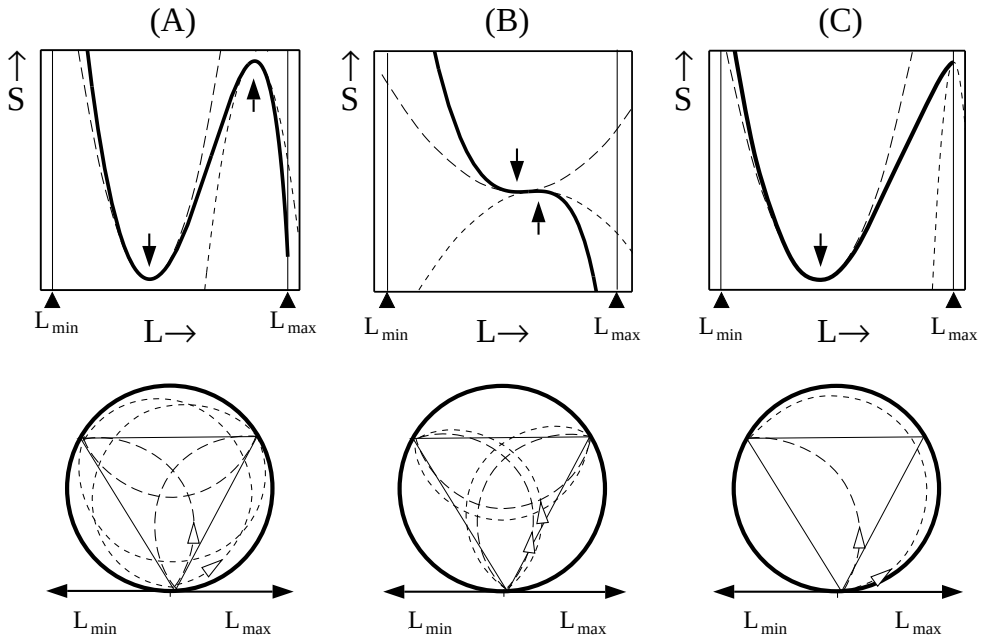

Figure 4.12: *$\hbar$ corrections to the stationary phase approximation of the trace integral of the level density. Upper row: Classical action S in dependence of the angular momentum L (solid). Dashed lines give the quadratic approximations at the stationary points (arrows). Lower row: Classical orbits corresponding to the stationary points of $S(L)$. (A) Generic Gutzwiller case, (B) close to a bifurcation, (C) close to the integration limit: creeping orbits.*

situation, where the stationary points are well separated from each other and from the integration limits. There, the stationary phase approximation according to Eq. (2.9) is well justified. Near a bifurcation, the stationary points are in close proximity. This is shown in Fig. 4.12(B). The situation corresponds exactly to the one discussed in Sec. 2.4. There is was outlined that uniform approximations are the appropriate tool to overcome the spurious divergencies of the standard Gutzwiller approach at the bifurcation points.

Applying the uniform approximation for tangent bifurcations Eqs. (B.7, B.8) to the disk billiard, a modified trace formula which incorporates all bifurcations can be derived. This trace formula reads

$$\delta g = \frac{1}{\pi\hbar} \sum_{\beta=(v,w)} D_\beta [a\mathrm{Ai}(\eta)\cos(\chi) + b\mathrm{Ai}'(\eta)\sin(\chi)] \; . \tag{4.18}$$

[4]Note that $S(L) = S(L, \beta)$, i. e. the functional dependence of S on L, depends on the type of orbit.

with

$$
\begin{aligned}
D_\beta &= \frac{1}{E_0}\frac{\pi}{\sqrt{kR}}\cos\Theta\sqrt{\frac{R_c\sin\Theta}{vs}} \\
a &= \left(\frac{3}{2}v\left|\frac{R_c}{R}\widetilde{\gamma}-\frac{s\sin\Theta}{R_c}\right|+\frac{3\pi(\sigma_{\beta+}-\sigma_{\beta-})}{8}\right)^{1/6} \\
b &= \frac{1}{a}\left(\frac{s}{R\cos(\Theta)}-\frac{2\widetilde{\gamma}}{\pi}\right) \\
\eta &= \begin{cases} +a^4 & \text{for} \quad \sin\Theta > R_c/R \\ -a^4 & \text{else} \end{cases} \\
\chi &= v\left(\frac{R_c}{R}\frac{\pi}{2}+\frac{R}{R_c}\frac{\sin(2\Theta)}{2}\right)+\frac{\pi(\sigma_\beta^+ + \sigma_\beta^-)}{4} \\
\widetilde{\gamma} &= \begin{cases} \mathrm{acos}(R\sin(\Theta)/R_c) & \text{for } \sin\Theta > R_c/R \\ \mathrm{acosh}(R\sin(\Theta)/R_c) & \text{else} \end{cases} \quad .
\end{aligned}
$$

For the reasons mentioned in Sec. 3.4, again the smoothed level density is considered in the numerical evaluation. The implementation of the smoothing in the trace formula requires special care, as the amplitude factors of Eq. (4.18) are oscillating functions. The procedure how to deal with this complication is discussed in Sec. 3.3.1. The result of the uniform approximation, together with the influence of the smoothing scheme, is examined in Fig. 4.13. There the contributions of the $\beta = (4,1)^{\pm}$ orbits to the oscillating part of

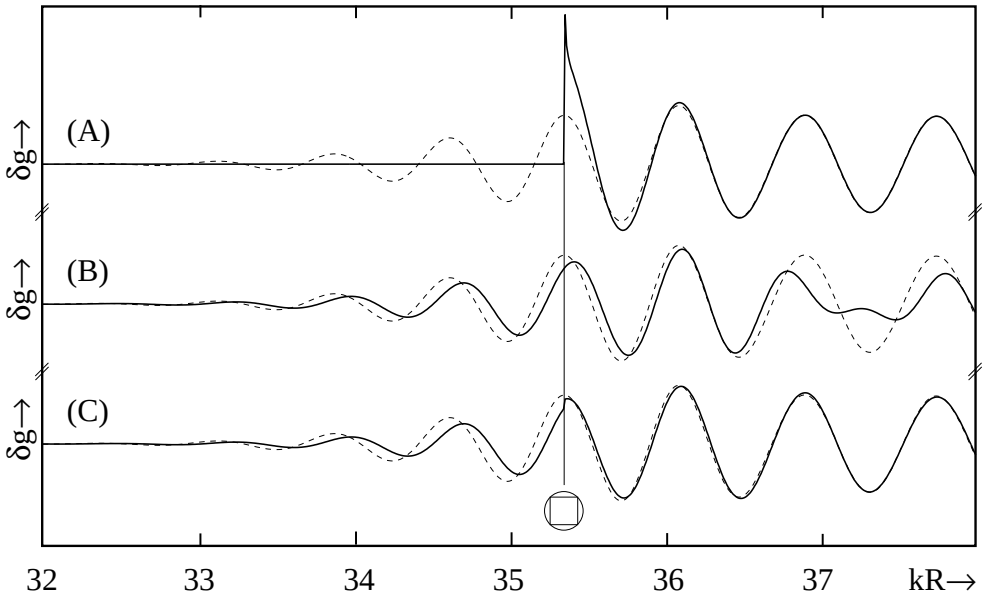

Figure 4.13: *The influence of the smoothing scheme on the uniform approximation. All data correspond to the contributions of the $\beta = (4,1)^{\pm}$ orbits to the semiclassical level density for $\widetilde{B} = 50$ and $\widetilde{\gamma} \approx 0.21$. The dashed lines in (A-C) give the uniform result together with the exact implementation of smoothing according to Sec. 3.3.1. The solid lines show (A) Gutzwiller result; (B) naive implementation of the smoothing, assuming slowly varying amplitudes; (C) improved ansatz as explained in the main text.*

the level density are plotted for $\widetilde{B} = 50$ and $\tilde{\gamma} \approx 0.21$. In Fig. 4.13(A), the solid line gives the result of the Gutzwiller trace formula, with smoothing according to Eq. (3.14). The

characteristic divergence at the bifurcation point can clearly be seen. For $\widetilde{B} \lesssim 35.36$ the $(4,1)^{\pm}$ orbits classically do no longer exist, so that their contribution to the Gutzwiller trace formula is zero. The uniform approximation Eq. (4.18) with smoothing according to Eq. (3.29) is illustrated by the dashed lines in (A-C). This ansatz interpolates smoothly over the bifurcation. Far on the *real side* of the bifurcation, i. e. the side where the orbits classically exist, the uniform approximation reproduces, as expected, the Gutzwiller result. On the *complex side*, the uniform approximation includes contributions of ghost orbits. These are damped exponentially. The detailed discussion of the effects of the bifurcations on the level density is postponed until the influence of the smoothing scheme on the uniform result is examined.

In (B), the correct smoothing scheme (dashed) is compared to the naive application of Eq. (3.14). This ansatz corresponds to the approximation of the Airy functions in Eq. (4.18) as constants. Except for the vicinity of the bifurcation, this approach fails completely. This is easily understood looking at the formula for the uniform treatment of the tangent bifurcation Eqs. (B.7, B.8). Applying the smoothing scheme of Eq. (3.14) to this expression, the damping depends on the average $\partial S/\partial E$ of the two orbits. This does not converge to the correct limit far from the bifurcation, which is given by the Gutzwiller expression. There the damping is given in terms of the individual orbit frequencies. The correct asymptotic behavior on the real side can be imposed by interpreting the damping terms as parts of the semiclassical amplitudes, thus including them in the sum and difference terms of the amplitudes in Eqs. (B.7, B.8). This approach, however, is restricted to the real side, since on the complex side the actions are imaginary. This results in complex arguments for the window function, which is not covered by the smoothing scheme of Sec. 3.2. In Fig. 4.13(C), this modified smoothing scheme (solid) is compared with the exact implementation according to Eq. (3.29) (dashed). On the real side this simple approach leads to acceptable results. The difference to the exact inclusion of smoothing on the complex side of the bifurcation, however, is not negligible.
In conclusion, Fig. 4.13 shows that the correct implementation of smoothing is crucial when considering bifurcations in the trace formula. It leads to significant corrections to the standard schemes.

Now as the effect of the smoothing scheme has been examined, the influence of the bifurcations on the level density should be considered. In Fig. 4.14(A), once again the contribution of the $(4,1)^{\pm}$ orbits to the level density with (dashed) and without (solid) uniform approximation is plotted. The large mismatch confirms that neglecting the bifurcation results in a wrong contribution of a single orbit to the trace formula. The total level density, however, is not much affected. This is shown in (B, D) for two smoothing widths. Broad smoothing leads to a small number of orbits which contribute to the trace sum. Since the bifurcation points of these orbits do not coincide, the other orbits partially mask the effect of a bifurcation (B). For narrow smoothing (D) more orbits contribute to the trace formula, and the net effect of the bifurcations further decreases. Even the widths of the poles at the divergencies get less wide when more orbits are included. This effect is due to higher repetitions of the bifurcating orbits. These bifurcate at the same points as the primitive orbits. Fig. 4.14 indicates that the effects of the different bifurcations compensate to a great extent.

Although a finer resolution leads to a larger number of bifurcations included in the trace formula (illustrated by vertical lines in Fig. 4.14(C)), their net effect decreases. The shell structure is therefore more affected by the $\hbar$ corrections than the full quantization data. For extremely broad smoothing, however, the effect of the bifurcations also decreases. This

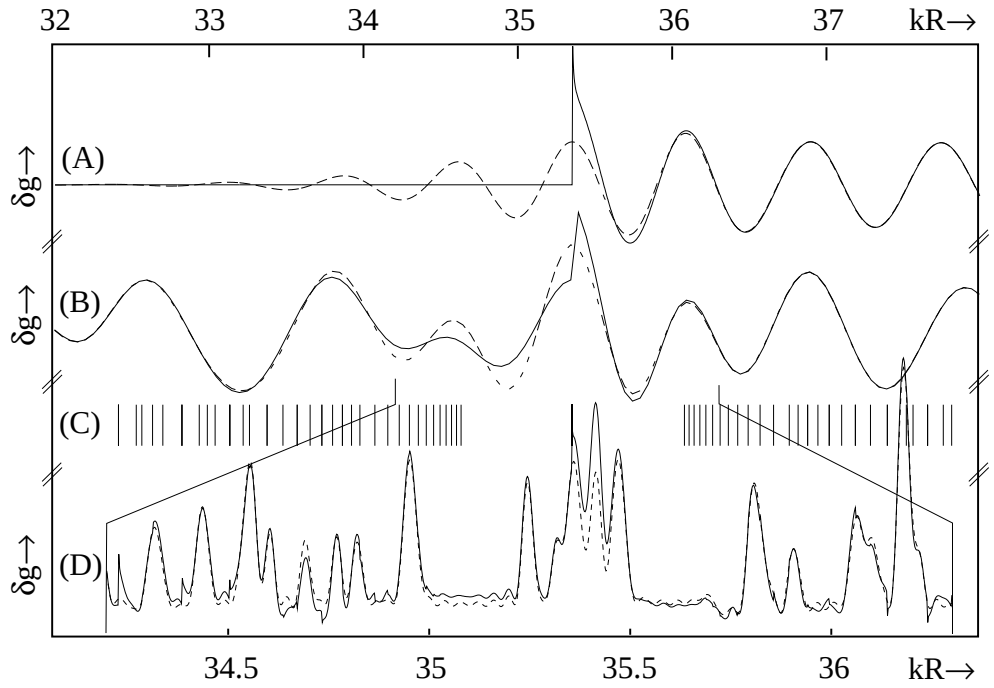

Figure 4.14: *Comparison between the standard trace formula (solid) and the uniform approximation (dashed) for* $\widetilde{B} = 50$. *(A) shows the contribution of the orbits* $(4,1)^{\pm}$, *(B) and (D) give the level density with smoothing widths of* $\widetilde{\gamma} \approx 0.21$ *and* 0.012 *in* kR. *The vertical lines (C) indicate the positions of the bifurcations of the orbits included in the calculation of (D).*

is due to the properties of the periodic orbits in the disk billiard: At the bifurcation point, the quasiperiod (i. e. the geometrical orbit length) is given by (cf. Eq. (4.14))

$$L_{\mathrm{bif}} = Rv\pi \sin(\pi w/v) \approx R\pi^2 \; . \tag{4.19}$$

The approximation on the r.h.s. is justified for all orbits except the diameter (where $L_{\mathrm{bif}} = 2R\pi$), since for strong smoothing only the orbits with $w = 1$ are relevant. Smoothing widths equivalent to an cut-off length $L_{\max} \approx R\pi^2 w$ therefore lead to a strong damping of the contributions from bifurcations. A cut-off length $L_{\max} < R\pi^2 w$ suppresses the bifurcations completely.[5] This is the reason why in Fig. 4.11 the expected divergencies at the bifurcations can not be seen.

The maximum effect of the bifurcations on the level density should therefore be observed for medium strong smoothing. This situation is plotted in Fig. 4.15, where the length cutoff of the triangular window function was taken to be $L_{\max} = 12R$, corresponding to a smoothing width of $\widetilde{\gamma} \approx 0.195$. The dashed lines give, just as in Fig. 4.11, the exact quantum result with equivalent smoothing. It is compared to the standard Gutzwiller approach in (A, C) and to the uniform approximation in (B, D). Even for this situation, where the influence of the bifurcations is maximal, the uniform approximation only leads to marginally better results than the standard trace formula.

In conclusion, the influence of the bifurcations is negligible for all spectral resolutions from the shell structure up to full quantization. Fig. 4.11 illustrates that the contributions are

[5] This strictly holds only for window functions with $F(L) = 0 \; \forall \; L > L_{\max}$, as for the triangular window function used here.

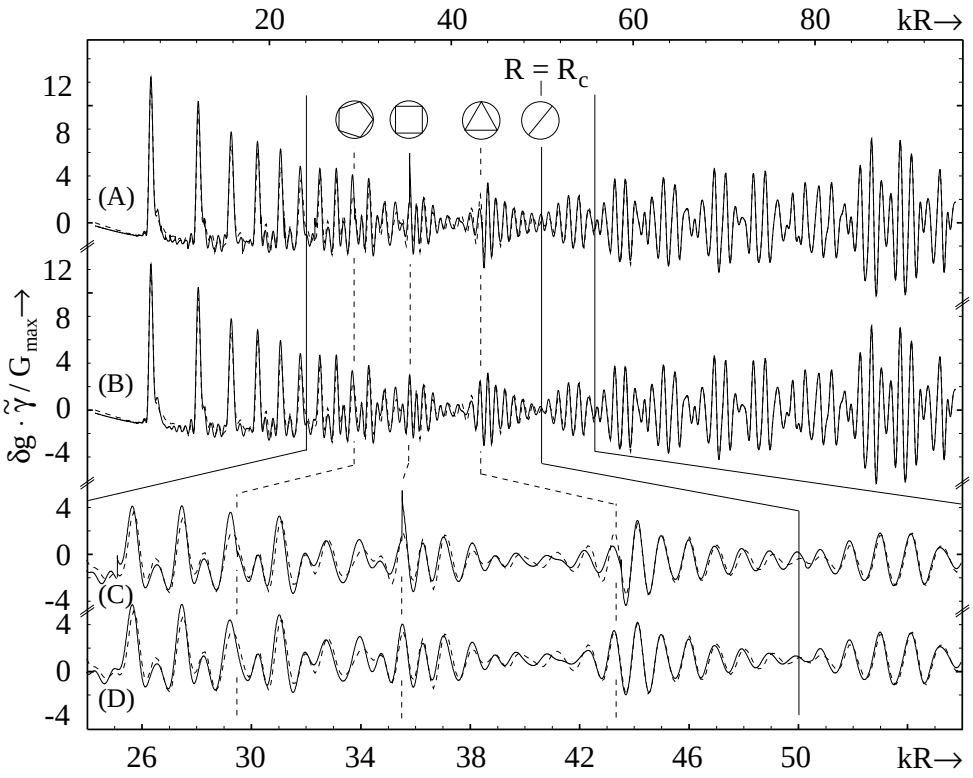

Figure 4.15: *The influence of the bifurcations. Dashed: exact quantum result for* $\widetilde{B} = 50$, $\widetilde{\gamma} \approx 0.195$. *Solid lines correspond to the standard Gutzwiller formula in (A, C) and to the uniform approximation in (B, D). The* $\hbar$ *correction from the bifurcations is small and strongly localized at the bifurcation points.*

damped out for large smoothing. For intermediate strong smoothing, as presented in Fig. 4.15, the uniform approximation slightly improves the semiclassical level density. The effect, however, is localized in a narrow region around the bifurcations and hardly relevant in size. For higher resolution spectra, Fig. 4.13 shows that the contributions of the bifurcations mostly cancel. The widths of the divergencies are becoming smaller, and their net effect further decreases. The bifurcations therefore do not give rise to a relevant $\hbar$ correction of the semiclassical level density, even though they lead to divergencies of the trace formula. It should be noted that the $\hbar$ correction from the bifurcations is comparable in size with the correction stemming from the correct implementation of smoothing. It is therefore not reasonable to include the uniform approximation without adapting the smoothing scheme.

4.3.4 Grazing

The mechanism which necessitated the implementation of the uniform approximation in the last section was that the final stationary phase approximation in the derivation of the trace formula for the disk billiard failed close to bifurcations points. Fig. 4.12, which plots the dependence of the action S on the angular momentum L of the triangular orbit, shows that another correction might be relevant in this step.

In Fig. 4.12(A) the stationary points, which correspond to the periodic orbits sketched below, are well separated both from each other and from the integration limits. Fig. 4.12(C) illustrates the case where the β^+ orbit approaches the maximum angular momentum. For

orbits which creep along the billiard boundary, one integration limit coincides with the stationary point. The contributions of these paths to the trace sum are expected to be half the value of the original formula. These corrections apply for orbits close to the boundary, so that they are called *grazing corrections*. At $\widetilde{B} = kR$, i. e. for $R_c = R$, this correction applies to all β^+ orbits simultaneously[6]. For this magnetic field strength the effect should therefore be most pronounced.

The grazing correction can be included in the trace formula by incorporating the finite integration limits. This leads to Fresnel type of integral instead of the Gaussian integrals occurring for the unconstraint integration according to Eq. (2.9). The corresponding modification of the trace formula for the disk billiard reads

$$\delta g = \frac{1}{\pi\hbar}\mathcal{I}m\left[\sum_{\beta} A_\beta B_\beta e^{i\left(\frac{S_\beta}{\hbar}-\mu_\beta\frac{\pi}{2}\right)}\right] . \tag{4.20}$$

The only changes to the original expression are the factors B_β, which replace the additional phases δ in Eq. (2.15). These complex factors are defined as

$$B_\beta = \sum_{\xi=\xi_{\rm u},\xi_{\rm o}} 2^{-1/2}\left[C(\xi) + i\alpha S(\xi)\right] . \tag{4.21}$$

For β^+ orbits and $R_c < R$ the coefficient $\alpha = -1$, otherwise $\alpha = +1$. The $\xi_{\rm u\atop l}$ are determined by the upper and lower integration limit, respectively:

$$\xi_{\rm u\atop l} = \sqrt{\frac{kR}{\pi}}\sqrt{\frac{2vs}{R_c\sin\Theta}}\left|\frac{R_c \mp R}{s - \zeta R\cos\Theta} \mp \zeta\cos\Theta\right| . \tag{4.22}$$

The geometrical quantities Θ and s are explicitly given in Eq. (4.7) on page 32. $\zeta = +1$ for the β^+, and $\zeta = -1$ for the β^- orbits. For constant energy ξ is proportional to $\hbar^{-1/2}$. Taking into account the finite integration limits therefore leads to corrections of the order $\sqrt{\hbar}$ beyond the leading order.

The numerical evaluation of the trace formula again forces the introduction of a finite smoothing width. The Fresnel integrals C and S are oscillating functions. Therefore the common damping ansatz Eq. 3.18 can not be used. The appropriate generalization is given in Sec. 3.3.1, and Eq. (3.29) applies to the situation considered here. Fig. 4.16 shows the semiclassical level density with (solid black) and without (gray) grazing correction. The simple smoothing which assumes the Fresnel factor to be a slowly varying function is given by the dotted line. The magnetic field is $\widetilde{B} = 50$, so that $R_c = R$ for $kR = 50$. The smoothing width is $\widetilde{\gamma} \approx 0.33$. The upper part of the figure shows the contributions of the β^+ orbits. The closeup in the inset confirms that the simple smoothing (dashed) leads, indeed, to a 50% correction of the Gutzwiller contribution (gray) of the β^+ orbits. Including the correct windowing (solid black), however, mostly compensates this effect. Even more surprising is the behavior of the β^- orbits. Although they are not as close to the integration limit as the β^+ orbits, their grazing correction is nearly of the same magnitude. The lower part of the diagram shows the total effect of the grazing correction including all orbits. At $\widetilde{B} = 50$, which corresponds to $R_c = R$ where the grazing effect was expected to be most pronounced, the influence of the correction is small. The main

[6] For $R_c = R$ all β^+ orbits coincide, building the *whispering gallery*.

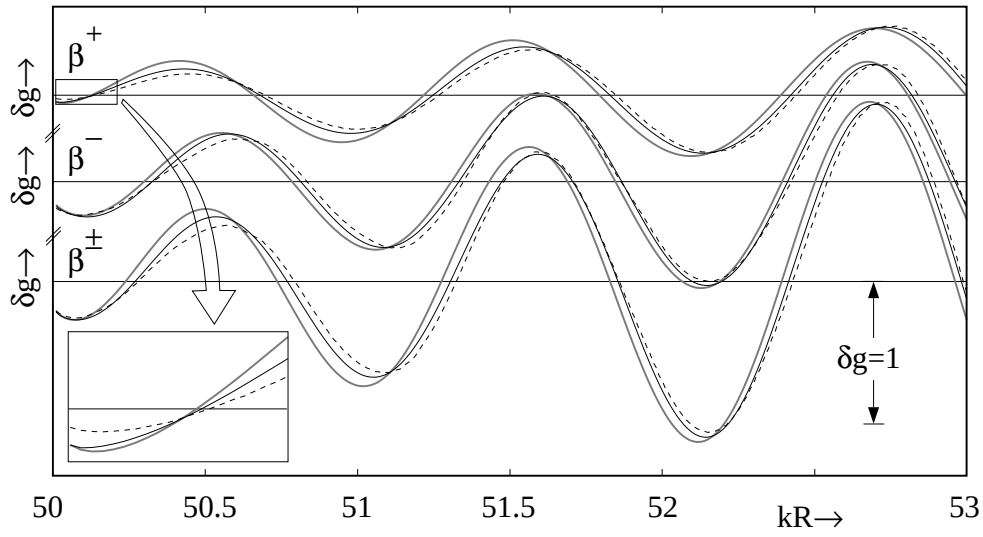

Figure 4.16: *The effect of the grazing correction for* $\widetilde{B} = 50$ *and* $\widetilde{\gamma} \approx 0.33$. *Gray: without grazing correction; dashed: grazing correction with simple smoothing; solid black: grazing correction with correct smoothing. Offset for clarity.*

effect is not a variation of the amplitude, but a slight shift of the phase stemming from the complex part of B_β.

This result shows that the $\hbar$ correction stemming from grazing can be neglected in the trace formula of the disk billiard. Please note that the effect of the correct windowing is of the same order of magnitude as the correct implementation of the grazing effect. As for the bifurcation treatment above, this again shows that the technical detail of the implementation of smoothing is of considerable importance.

4.4 Semiclassical interpretation of δg

An attractive feature of the semiclassical approximation which was not used until now is the simple, intuitive picture it gives. This should be exploited in the following to explain the shell structure of the disk billiard in terms of classical quantities.

According to the trace formula Eq. (2.15), each periodic orbit β contributes an oscillating term to δg. Its frequency is determined by the classical action S_β along this path, which can be locally approximated by

$$S_\beta(k) = S_\beta(k_0) + \hbar\, G_\beta(k)\ (k - k_0)\ , \tag{4.23}$$

with the *quasiperiod* $\hbar G$. For billiard systems the quasiperiod is, according to Eq. (3.21), identical to the geometrical orbit length L given in Eq. (4.14). The amplitudes of the oscillating terms are $A_\beta\, F(G_\beta)$, where F is the window function that depends on the desired smoothing of the level density. Prior to the interpretation of the contributions of the various orbits to δg, the behavior of $G_\beta (= L_\beta)$ and A_β shall be discussed.

Fig. 4.17 shows the dependence of G on the ratio $R_c/R = kR/\widetilde{B}$. Note that for $R_c > R$ (see right diagram of Fig. 4.17) G is independent of the direction of motion $\pm$, even if the classical action depends on it. In strong fields ($R_c < R$, left diagram) G is different for the "+" and the "–" orbits. Only at the bifurcation points, where the two orbits coincide,

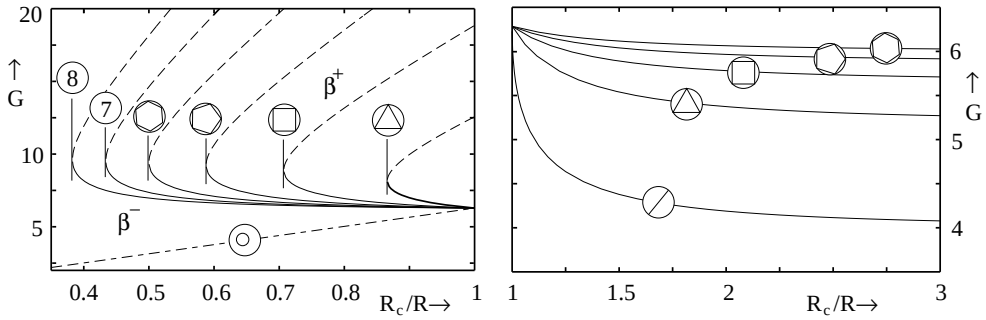

Figure 4.17: *The quasiperiods G of the most important orbits in dependence of R_c/R. For $R_c > R$, G is independent of the index $\pm$. The orbit bifurcation points in strong fields (vertical lines) can clearly be seen.*

they have identical G. According to Eq. (4.19), the value of G at the bifurcation points converges to $w \cdot \pi^2 R$ for strong fields.

In Fig. 4.18 the amplitudes of the orbits relative to the $B = 0$ values,

$$A_\beta^0 = \frac{\sin^{3/2}\Theta}{\sqrt{v}} \,, \tag{4.24}$$

are plotted versus the ratio R_c/R. The amplitude of the "–" orbit is always larger than that of the corresponding "+" orbit. At $R_c = R$, where the "+" orbits change the topology (see Fig. 4.3), their amplitudes are zero, so that these discontinuities do not lead to artefacts in the level density. At the tangent bifurcations discussed above, the orbit amplitudes diverge.

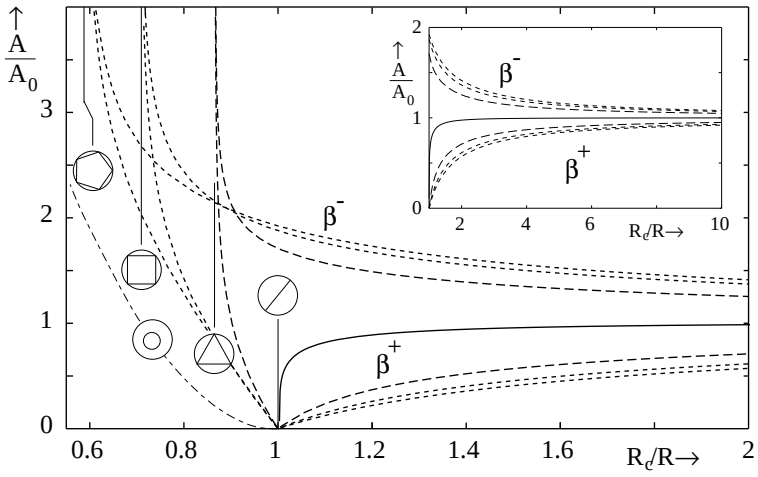

Figure 4.18: *The amplitudes of the dominating orbits $\beta = (v,1)^\pm$ with $v = 2,\ldots,5$ relative to their $B = 0$ value. (The amplitude of the cyclotron orbit is in arbitrary units.) At the bifurcation points $R_c = \sin(\pi\ v/w)$ indicated by vertical lines, the amplitudes diverge. For $R_c > R$ the amplitudes of the bouncing orbits quickly approach their asymptotic (zero-field) value. The inset shows this convergence in a wider range.*

Now the shell structure shall be interpreted in these classical terms, starting with the weak-field regime ($R_c > R$). The amplitudes for zero field given in Eq. (4.24) are proportional to $v^{-1/2}$, favoring orbits with a small number of bounces v. The dependence of the amplitudes on the magnetic field as shown in Fig. 4.18 indicates that in the region where the "–" orbits differ significantly from the "+" orbits, the latter are negligible. These effects[7] together strongly favor the $(2,1)$ and the $(3,1)^-$ orbit. They end up with comparable amplitudes. From this picture a pronounced beating pattern from the interference of the diameter and the triangular orbit is expected as the dominating feature of the level density. This beating

[7]The G dependence of $F(G)$ also slightly supports this effect.

pattern is indeed observed (cf. Fig. 4.11). The analogous effect in three dimensional metal clusters is known as *supershell oscillations* [61].[8] The semiclassical description furthermore predicts that this beating will persist in homogeneous magnetic fields up to a strength of $\widetilde{B} = kR$. This is in agreement with the findings in Fig. 4.11. The thick gray lines in the frames (1a) and (1b) correspond to a function[9]

$$\sin(kG_{(1,2)}) + \sin(kG_{(1,3)^-}) = \sin\left(k\frac{\Delta G}{2}\right)\ \sin\left(k\frac{\bar{G}}{2}\right)\ . \tag{4.25}$$

It correctly predicts the structure of the level density in this regime.

Approaching the field strength where $R_c = R$, all orbits change G sharply to $2\pi R$. At this point, the β^+ orbits coincide. The amplitude of this collective mode is small. The β^- orbits differ from each other at $R_c = R$. The change of S with varying B is, however, identical for all orbits, since according to Eq. (4.23) all bouncing orbits have the same lengths for $R_c = R$. This implies that the variation with magnetic field is coherent for all bouncing orbits, although their absolute values of S are different. The semiclassical picture therefore predicts that the beating behavior will disappear at $R_c = R$, leaving just a simple oscillation with the common frequency. In Fig. 4.11 this sudden stop of the beat at $R_c = R$ can clearly be seen. The gray line in frame 2 shows that the frequency of the remaining single oscillation is predicted correctly.

In strong fields, only cyclotron orbits and bouncing orbits with a great number of bounces v exist. The amplitudes of the latter are proportional to $v^{-1/2}$, so that in the strong field limit the cyclotron orbits are expected to dominate the level density. The gray lines in frame 3 of Fig. 4.11 show the corresponding oscillating term,[10] which, indeed, reproduces the main feature of the quantum-mechanical result (solid black). The skipping orbits with greatest amplitudes are those which are close to their bifurcation points. All those orbits have nearly the same value of $G = w \cdot \pi^2 R$. Their contributions should therefore interfere constructively, giving rise to small structures in the level density of this period. Such structures can indeed be observed in a higher-resolution spectrum, and their spacing is consistent with this simple picture.[11] The effect of the only relevant $\hbar$ contribution was already discussed in Sec. 4.3.2. The reflection phases remove the degeneracy of all cyclotron orbits, leading to slightly higher energies of the orbits close to the billiard boundary. This leads to a reduction of the Landau peak heights and to an increased level density slightly above the Landau levels. This correction is only relevant in the intermediate strong field regime $R_c \lesssim R$.

This analysis shows that the simple semiclassical picture using only the classical properties of three periodic orbits is able to explain the main features of the quite complicated behavior of the level density[12] for arbitrarily strong fields.

[8] In the 3D spherical cavity, the beat is due to the interference of the triangle and the square orbits (see Ref. [11]).

[9] The phases are, of course, adjusted.

[10] For a simpler comparison, the amplitude is chosen to rise quadratically, as indicated by Eq. (4.10).

[11] For details see Refs. [1, 4].

[12] Here the dependence of the level density on the energy was interpreted. For the dependence on the magnetic field a completely analogous approach is possible.

4.5 Summary

In this chapter, a semiclassical approximation for the level density of the disk billiard in homogeneous magnetic fields was derived. The agreement of the standard trace formula with the exact quantum result is excellent for small fields as well as for extremely strong fields, but not in the intermediate regime. This failure was suspected to be due to $\hbar$ corrections to the trace formula. Three different $\hbar$-corrections have been analyzed.

First a correction to the Maslov index was considered. This exhibits a discontinuity when the reflection at the hard boundary is, with increasing field strength, replaced by the soft turning point in the magnetic potential. A one-dimensional approximation leads to reflection phases which interpolate smoothly between these limits. It was shown that replacing the Maslov indices by reflection phases is of great importance in the strong field regime $R_c \lesssim R$. This holds for the shell structure as well as for full quantization.

At bifurcations, the second-order approximation of the action S around stationary points breaks down, leading to spurious divergencies in the semiclassical amplitudes. A uniform approximation to higher order in S shows that at the tangent bifurcation the contribution to the trace formula is increased by a factor $\hbar^{1/6}$ [70]. The inclusion of this $\hbar$ correction is important when one considers the contribution of individual orbits to the trace formula. The corrections, however, rapidly loose influence if either many orbits are included (which generally is the case if a higher resolution of the spectrum is required), or the smoothing is so broad as to suppress the bifurcating orbits strongly. The main result of this consideration is that the bifurcations have the maximum influence on moderately coarse-grained level densities. But even for this case, the $\hbar$ corrections due to the bifurcations are only marginal.

Finally the creeping correction, formally occurring due to finite integration limits, was shown to be completely negligible in the semiclassical approximation — although on first sight it is expected to be a 50% effect. Both the implementation of bifurcation and of grazing effects require a modification of the smoothing procedure. The corrections from the adapted smoothing are in both cases comparable to the magnitude of the $\hbar$ corrections themselves.

These considerations show that the only relevant correction to the trace formula is given by the reflection phases. Including this, the semiclassical trace formula for the level density is a good approximation for arbitrarily strong fields. It reproduces the exact quantum-mechanical result with a remarkably reduced numerical effort. For the quantum-mechanical calculation shown in Fig. 4.11, about 2500 eigenvalues had to be calculated and numerically smoothed for each value of $\widetilde{B}$, whereas the semiclassical result is obtained summing the contributions of just 20 orbits.[13]

The main features of the level density could be explained in a simple picture. The classical properties of three interfering orbits are sufficient to explain the behavior of the level density in arbitrary field strengths. In weak fields the diameter together with the the inwards-curved triangular orbit lead to a pronounced beating pattern. For $\widetilde{B} = kR$ all orbits interfere constructively, and in strong fields the cyclotron orbits dominate. They lead to the Landau quantization. The degeneracy of the Landau levels is reproduced correctly implementing the proximity effect of the boundary via the refection phase.

[13] For $R_c > R$ even 10 orbits are sufficient.

Chapter 5

Semiclassical Transport

Transport properties are, in contrast to the level density considered above, readily accessible in experiment. This chapter gives a short introduction to the semiclassical approximation of electrical transport within the linear response formalism. The formulas presented will be used in the subsequent chapters.

Contents

The semiclassical approximation of the level density has been successfully applied to hydrogen as well as to Rydberg states [92, 52] and to neutral helium [28]. In all these cases, the experimental observables are emission or absorption lines. A theoretical description hence has to resolve the individual energy levels of the system. This is feasible in a semiclassical approach, but not the most favorable application of this method. For the required full quantization, many periodic orbits have to be included in the trace formula. The benefit from a semiclassical approach is considerable larger for systems where the line widths exceed the mean level spacing. In these situations only the shell structure is observed, which usually depends only on a few orbits.

Systems in this regime include nuclei, clusters and nanostructured devices – finite fermion systems with particle numbers of some 10 to a few 1000. For all these systems, semiclassical level density calculations have been performed. Such an analysis was presented for the fission barrier of nuclei [19, 118] as well as for the shell structure of metal clusters in magnetic fields [77] and their ground-state deformation [121, 122, 59]. Apart from these examples, the application of the standard trace formula to experimental situations is very limited, as the level density is rarely directly observable. In some cases a close relation to the measured quantity can be assumed. Such an approach was used for the analysis of the mass distribution of sodium clusters [61] or the magnetoconductance of a mesoscopic circular quantum dot [2].

To extend the applicability of semiclassical methods it is desirable to develop descriptions for other physical quantities than the level density. This has been done for example regarding the magnetic susceptibility [96, 78], current oscillations in I-V curves [114] or the conductance [63, 41].

As already pointed out, nanostructured semiconductor devices are extremely versatile systems. Many parameters like size, geometry, electron density or magnetic field can be varied experimentally, some even during measurement. This opens up tremendous new theoretical and experimental opportunities, as many of these parameters are beyond control in more "natural" systems like atoms and nuclei. Most easily accessible to measurement are electrical transport properties. This is also an area of great commercial interest: The rapid developments in semiconductor technology lead to continually decreasing feature sizes on memory or logic circuits. The smallest structures already approach the mesoscopic scale. It is for these reasons, the direct experimental access, the great variability of the device, the large number of controllable parameters, and the commercial relevance that much of the work on nanostructures deals with electrical transport properties.

A quantum mechanical description of these systems is very demanding. The usually large number of electrons involves the calculation of numerous highly excited states. Regarding semiclassics, in contrast, high quantum numbers are especially favorable. As pointed out above, the semiclassical description is further facilitated by the broad line widths of these systems, which generically only allow the observation of the shell structure. All this makes a semiclassical approach to these structures very promising.

The following sections are devoted to the derivation of a semiclassical linear response formula for electrical transport. This will be applied to specific systems in the subsequent chapters.

5.1 Semiclassical linear response

The calculation of transport properties for small external fields is possible within the context of linear response theory. This powerful tool relates the response of a system to a small external excitation to its ground state properties. Richter and Mehlig [58, 120] have derived a general semiclassical treatment of dynamic linear response functions for ballistic quantum systems at finite frequency and finite temperature. Their ansatz is not only applicable to electrical transport, but also to magnetic properties or far-infrared absorption of closed quantum dots. Here, the discussion is restricted to electrical transport in static external fields. Please note that due to the linear response ansatz all nonlinear transport effects are beyond the scope of this work. Those effects can already occur for low-excitation measurements (cf. Ref. [74]).

For absolutely clean systems the conductivity is not finite. In contrast to the level density, which can also be calculated for pure systems, transport properties are inseparably related to the disorder present in the system. The semiclassical approximations therefore depend strongly on the detailed properties of the scatterers in the sample. This is why it is not possible to give a unified approach valid for all situations.

The following section will describe the different transport regimes, before Sec. 5.5 presents a semiclassical approximation for coherent ballistic transport. This is the regime that will be relevant for the specific systems considered later.

5.2 Different transport regimes

The transport properties depend on the microscopic scattering process, the density of the scatterers, their strengths and their distribution. A rough classification of the different transport regimes is possible regarding the typical length scales involved:

The system size a:
This important datum for the discussion of quantum oscillations may be ambivalent for some systems.[1]

The magnetic length ℓ_B:
A magnetic fields introduces an additional length scale $\ell_B = \sqrt{\hbar/(eB)}$, which may replace the system size a in some problems. This complication will not be discussed here.

The Fermi wavelength λ_F:
$\lambda_F = 2\pi\hbar/\sqrt{2m^\star E}$ usually defines the smallest length scale. For two-dimensional systems this is equivalent to $\lambda_F = \sqrt{\pi/n_s}$, where n_s denotes the electron density per spin.

The elastic mean-free path ℓ:
This is a quantum mechanical quantity, generally without classical meaning. It is related to the total amplitude diffracted by disorder [68] and to the single-particle relaxation time [97]. It is often given in terms of the total relaxation time $\tau = \ell/v_F$.

[1] For a long, narrow channel it is *a-priori* not clear whether the length or the width is the characteristic quantity. Something similar holds for antidot lattices, where both the system size and the size of the elementary cell might be relevant.

Here v_F denotes the Fermi velocity $v_F = \hbar k/m^\star$, which in two dimensions can be expressed as $v_F = 2\hbar\sqrt{\pi n_s}/m^\star$.

The transport mean-free path ℓ_T:
This quantity can be interpreted classically, indicating the length scale over which the electron momentum is randomized. It is related to the momentum relaxation time τ_p via $\ell_T = \tau_p v_F$. Short-range impurity potentials lead to isotropic scattering, and $\ell_T \approx \ell$. For long-range impurity potentials the momentum before and after the scattering process are correlated, so that ℓ_T can significantly exceed ℓ.

The phase coherence length ℓ_Φ:
ℓ_ϕ gives the length over which the phase coherence of the wave function is lost. The phase coherence length exceeds the mean-free path, as elastic scattering preserves phase coherence. Only some inelastic scattering processes lead to finite ℓ_ϕ.

Depending on these length scales, transport can roughly be divided into the following regimes:

macroscopic ($a \gg \lambda_F$) or microscopic ($a \gtrsim \lambda_F$):
$a \gg \lambda_F$ is the regime of high quantum numbers, where the levels get closer in energy.[2] Once the line width exceeds the mean level spacing, the quantization information gradually disappears, eventually leading to classically smooth spectra.

classical ($a > \ell_\Phi$) or coherent ($a < \ell_\Phi$):
For $a > \ell_\Phi$, phase coherence is broken between two points in the system. Thus no correlation of the wavefunctions at these points is left, and the two parts of the system add classically (i. e. without interference).

diffusive ($\ell_T \ll a$) or clean ($\ell_T \gg a$):
The regime ($\ell_T > a$) is often referred to as the *ballistic regime*. There particles can traverse the system without randomizing their momentum.

The distinction between diffusive and ballistic systems is easily visualized in the semiclassical picture. Fig. 5.1(A) depicts the diffusive situation, where a trajectory is frequently scattered, and the motion is essentially a random walk. The periodic orbits in this system are depicted in the lower part of Fig. 5.1(B). They depend on the individual locations of the scatterers. The assumption that, in analogy to the level density discussed above, the

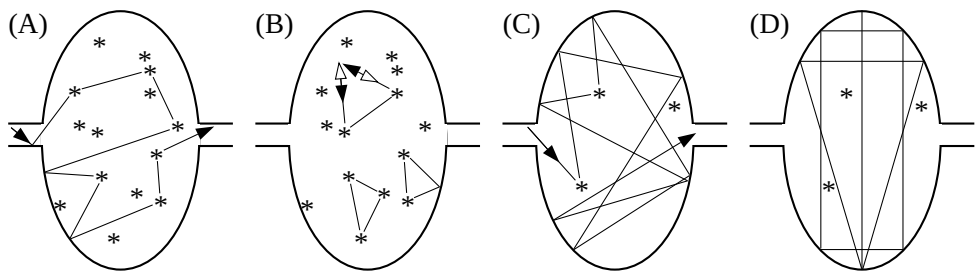

Figure 5.1: *Diffusive (A, B) and ballistic transport regime (C, D). (B) and (D) depict some classical closed orbits. These are relevant for quantum oscillations.*

[2] This holds for systems where the number of degrees of freedom minus the number of constants of motion is larger than one.

system properties depend on the classical periodic orbits already captures the essential physics of these systems. The detailed structure of the magnetoconductance depends on the microscopic distribution of the scatterers, which is unique for each sample. This leads to the "fingerprint" characteristics of the magnetoconductance of disordered samples.

Weak localization, another effect in diffusive samples, can be understood as a consequence of coherent backscattering: The central mechanism is that closed paths as in the upper part of Fig. 5.1(B) can be followed in both directions. Their contributions therefore interfere constructively. This enlarges the return probability of the particle, which is hence weakly localized. A magnetic field breaks the time-reversal symmetry, so that the two orientations are no longer coherent. This explains why a magnetic field destroys weak localization. Detailed information about these and related diffusion-based effects can be found in Refs. [99, 90, 91].

In the following coherent ($a < l_\Phi$), ballistic ($l_T > a$), mesoscopic ($1 \ll \lambda_F/a \ll \infty$) transport is considered. Fig. 5.1(C) sketches the ballistic case, where trajectories are rarely scattered. In this regime the periodic orbits (c.f. Fig. 5.1(D)), and thus the quantum oscillations, mainly depend on the confinement of the system and not on the distribution of the scatterers.

The effects of disorder on the semiclassical approximations have already been listed on page 17. For the low impurity concentrations of ballistic systems, periodic orbits as in Fig. 5.1(B) can be neglected, and the coherence of degenerate families is hardly affected. The orbits which contribute in the ballistic regime are therefore those of the clean system. Disorder induces a finite probability of scattering out of a periodic trajectory. This leads to a reduction of the semiclassical amplitudes.

Note that in the ballistic regime the quantum oscillations are dominated by the confinement potential, i. e. depend on the fact that the system is finite. Therefore quantum mechanical calculations including impurity scattering which rely on the translational invariance of an infinite system cannot be applied here.

5.3 The model for disorder

Scattering is, as already outlined in Sec. 3.1, introduced by appropriate averages. For a single, isolated system this is the average over the impurity constellation. If ensembles of systems, like dot-arrays, are considered, this average also includes system parameters like geometry and Fermi energy.

For an explicit calculation, both the scattering potential and the distribution of scatterers have to be known. The problem of a realistic description of these properties is not completely settled so far. The scattering potential depends strongly on the nature of the scatterer, its distance to the 2DEG, and, for ionized impurities, the screening properties of the 2DEG. Modeling the distribution of scatterers is also non-trivial. For high-mobility 2DEG, scattering at ionized donors is the dominant process. Their distribution does not only depend on the growth process,[3] but also on the cooling scheme. The underlying mechanism is called *coulomb ordering*. It applies to the generic case where only a part of the donors is ionized. While cooling down slowly, an energetically favorable subgroup is getting ionized. The ionized donors are hence preferably equally spaced. This introduces

[3] The growth process is usually, but not generally believed to lead to randomly distributed donors.

correlations in the positions of the scatterers, even if the donors themselves are randomly distributed [110, 113].

The calculation of transport properties, especially of line shapes and amplitudes, from realistic impurity potentials and distributions is currently an area of active research (see, e. g., [60]). As this work is not intended to contribute to this area, impurity correlation effects will be neglected in the following. A wide-spread model for uncorrelated impurities uses random gaussian potentials

$$V(\boldsymbol{r}) = \sum_{i=i} N \frac{V_i}{2\pi\xi^2} \exp\left[-\frac{1}{2}\left(\frac{\boldsymbol{r}-\boldsymbol{R_i}}{\xi}\right)^2\right] , \tag{5.1}$$

characterized by an average strength V_0 and a correlation length ξ. Following this ansatz, Richter [105] derived a semiclassical approximation for the susceptibility. He finds that the impurities can be included in the semiclassical susceptibility by factors $F(L)$ damping the orbit amplitudes. Due to the different averages involved, the results for individual systems differ from those for ensembles. They also depend on the relative size of the correlation length ξ, the system dimension a, and the Fermi wavelength λ_F. In the context of this work isolated systems with finite-range ($\lambda_F < \xi < a$) impurities will be considered. For those systems $F(L)$ is given by

$$F(L) = e^{-L/(2\ell)} , \tag{5.2}$$

with the elastic mean-free path ℓ. For these samples the transport mean-free-path ℓ_T is considerably larger than ℓ [105]. Therefore a ballistic treatment of systems with a size comparable to the elastic mean-free-path is still justified.

Please note that the ansatz of randomly distributed scatterers is restricted to the first repetition of classical orbits. This comes about as the repetition of an orbit sees the same impurity constellation as the primitive orbit. Therefore random impurity positions on the sample are not random along the trajectory. A refined discussion as presented by Richter [105] shows that the higher repetitions of orbits are also damped exponentially, but with an exponent depending quadratically on the repetition number.

5.4 Finite temperature

Just as the inclusion of scattering, the consideration of finite temperatures in semiclassical linear response formulae is not completely settled so far[4]. The intuitive approach to replace the δ functions in the corresponding quantum mechanical expressions by Lorentzians with width γ

$$\delta(E) \to \frac{1}{\pi}\frac{\gamma}{E^2+\gamma^2} \tag{5.3}$$

has been confirmed by more involved calculations [80] and has been established as a quasi-standard [112]. Since a detailed discussion of the microscopic mechanism involved in dissipation is beyond the scope of this work, this heuristic approach will be implemented.

[4] For grand canonical systems, the approach of Sect. 3.1 can shown to be exact [17].

5.5 The semiclassical Kubo formula

In the ballistic regime the quantum oscillations are, as already pointed out, determined by the sample boundaries, not by the impurity constellation. This *geometric* effect is of special interest, as the geometry of the sample can be adapted in a wide range. Two different types of ballistic devices can be distinguished:
The first are small structures coupled to leads, which are completely phase coherent. The current through these systems does not scale with the system size, so that only conductances, but no conductivities can be defined. For the transport through those samples, a semiclassical approximation of the Landauer-Büttiker formalism is appropriate. The generic example for the second class of devices is a regular array with a lattice constant smaller than the phase coherence length, and a total size exceeding ℓ_Φ. Then quantum oscillations stemming from interference effects within elementary cells can be observed, but the elementary cells themselves add classically. Therefore the definition of specific quantities like conductivities is justified. For those systems, Kubo linear response theory is the adapted description.
For the systems considered in this work, the Kubo formalism will provide the correct framework. Please note that the distinction between Kubo and Landauer does not reflect a physical difference: Quantum mechanically, both approaches have been shown to be equivalent [12].

The general idea how to obtain a semiclassical version of the Kubo conductivity is to express the quantum mechanical Kubo formula in terms of Green's functions. After the inclusion of finite temperature and weak disorder by appropriate averages, the Green's functions are replaced by their semiclassical approximation. Following this line, Richter and Hackenbroich/von Oppen derived a semiclassical expression for the oscillating part of the conductivity tensor.[5] They use approximation Eq. (5.2), which is equivalent to the assumption of an energy-independent scattering time. Temperature is included as indicated in Eq. (5.3). Vertex corrections, which correspond to orbits including scattering events (c.f. Fig. 5.1(B)), are neglected. Under these assumptions they find

$$\begin{aligned}
\delta\sigma_{xx}(E_F,B) &= \frac{2}{V}\frac{e^2}{h}\sum_{\mathrm{ppo},n} \qquad\qquad \mathcal{C}_{xx}\ \frac{R_n(\tau_\beta)F_n(\tau_s)}{|\mathrm{Det}(\widetilde{\mathrm{M}}^n-\mathbf{1})|}\cos\left(\frac{nS}{\hbar}-\mu_n\frac{\pi}{2}\right)\\
\delta\sigma_{xy}(E_F,B) &= \frac{2}{V}\frac{e^2}{h}\sum_{\mathrm{ppo},n}\left(\frac{1}{e}\frac{\partial S}{\partial B}+\mathcal{C}_{xy}\right)\frac{R_n(\tau_\beta)F_n(\tau_s)}{|\mathrm{Det}(\widetilde{\mathrm{M}}^n-\mathbf{1})|}\cos\left(\frac{nS}{\hbar}-\mu_n\frac{\pi}{2}\right)\ .
\end{aligned} \tag{5.4}$$

In these formulas the sum over the primitive periodic orbits ppo is separated from the sum over their repetitions n. All quantities except the Maslov indices μ refer to the primitive periodic orbit.[6] The temperature T is included by

$$R_n(\tau_\beta) = \frac{nT_0/\tau_\beta}{\sinh(nT_0/\tau_\beta)}\ , \tag{5.5}$$

with the temperature-related scattering time $\tau_\beta = \hbar/(\pi k_B T)$. The impurities lead to an exponential suppression of longer orbits according to Eq. (5.2). In the following an

[5] The derivations of the authors are virtually identical, and the results were published simultaneously. Please note the (identical!) misprints in the expression for σ_{xy} in Refs. [63, 41]. There, the action of the total orbit instead of the primitive orbit shows up in $\partial S/\partial B$. The formulas in Refs. [105, 42] are correct.

[6] The Maslov index for stable orbits is not proportional to the repetition number.

approximate expression for the damping term which depends on the period of the orbit instead of its lengths will be convenient:

$$F_n(\tau_s) = e^{-n^2 T_0/(2\tau_s)} \; . \tag{5.6}$$

The scattering time $\tau_s = m^*\mu/e$ is extracted from the experimental mobility μ. The velocity-velocity correlation $\mathcal{C}_{ij}$ of a primitive periodic orbit is finally given by

$$\mathcal{C}_{ij} = \int_0^\infty dt \; e^{-t/\tau_s} \int_0^{T_0} d\tau \; v_i(\tau)\, v_j(t+\tau) \; . \tag{5.7}$$

Apart from the prefactors and the velocity correlation function (which replaces the period of the orbit), the structure of the trace formula Eq. (5.7) is identical to the Gutzwiller expression for the level density Eq. (2.14).

The semiclassical approximation of the conductivity tensor will be used to calculate electrical transport properties of the free 2DEG in chapter 6 and of the channel with antidots in chapter 7. Prior to this, the basic formulas connecting σ with the measured voltages and currents will be reviewed.

5.6 Electrical transport

Within linear response, the local electrical field $\vec{E}$ and the local current density $\vec{j}$ are related via the *conductivity tensor* $\underline{\sigma}$ according to

$$\vec{j} = \underline{\sigma}\vec{E} \; . \tag{5.8}$$

The inverse tensor $\underline{\rho} = \underline{\sigma}^{-1}$ is known as the *resistivity*. It connects $\vec{j}$ and $\vec{E}$ by $\vec{E} = \underline{\rho}\vec{j}$, and is explicitly given by

$$\underline{\rho} = \frac{1}{\sigma_{xx}\sigma_{yy} - \sigma_{xy}\sigma_{yx}} \begin{pmatrix} \sigma_{yy} & -\sigma_{xy} \\ -\sigma_{yx} & \sigma_{xx} \end{pmatrix} \; . \tag{5.9}$$

For isotropic systems $\sigma_{xx} = \sigma_{yy}$ and $\sigma_{yx} = -\sigma_{xy}$, so that Eq. (5.9) simplifies to

$$\rho_{xx} = \frac{\sigma_{xx}}{\sigma_{xx}^2 + \sigma_{xy}^2} \qquad \text{and} \qquad \rho_{xy} = \frac{-\sigma_{xy}}{\sigma_{xx}^2 + \sigma_{xy}^2} \; . \tag{5.10}$$

For the free electron gas in high magnetic fields $|\sigma_{xy}| \gg \sigma_{xx}$. In this case the hall resistivity and the hall conductivity are, as expected, inverse quantities: $\rho_{xy} \approx 1/\sigma_{xy}$. The longitudinal conductivity, however, is proportional to the longitudinal resistivity: $\rho_{xx} \propto \sigma_{xx}$. This relation is somewhat counterintuitive.

For the usual hall-bar geometry, i. e. a macroscopic, homogeneous, rectangular system with length l and width w where a current I is drawn in x-direction, Eq. (5.10) leads to

$$U_x = R_l I \qquad \text{and} \qquad U_y = R_h I \; , \tag{5.11}$$

with the longitudinal resistance $R_l := \frac{l}{w}\rho_{xx}$ and the hall resistance $R_h := \rho_{xy}$. Please note that for two-dimensional systems the hall resistivity and the hall resistance are identical.

Chapter 6

Magnetoconductance of the free 2DEG

The experimental realization of a free two dimensional electron gas (2DEG) is outlined. The Shubnikov-de-Haas oscillations (SdH) in its longitudinal resistivity are reproduced by the semiclassical Kubo formula, but the plateaus in the Hall resistivity, i. e. the integer quantum Hall effect (QHE), are not. The description of the QHE succeeds by including a specific higher-order $\hbar$ term originating from the level density. The corresponding correction is derived for general systems.

Contents

The free two dimensional electron gas (2DEG) is predisposed as a test system for the semiclassical Kubo formula Eq. (5.4). The longitudinal conductivity in the presence of a transverse magnetic field B was already evaluated by the authors of the semiclassical Kubo formula [63, 41]. In the following sections, both the longitudinal and the Hall conductivity for the free 2DEG are derived. The resulting description is also valid for particles with spin. For those, n_s denotes the electron density per spin orientation, i. e. $n_s = 2(S+1/2)n_e$. For spin-less particles, n_s is given by the total electron sheet density n_e.

6.1 Two dimensional electron gas

The electronic bands of semiconductors bend at interfaces. In a suitable designed heterostructure (e. g. GaAs/GaAlAs), this leads to a narrow, triangular region at the interface where the conduction band is below the Fermi energy. E_F can be chosen so that only the lowest eigenstate of this well is occupied. For sufficiently low thermal energies higher states are energetically unaccessible, so that the corresponding degree of freedom is blocked. From a quantum mechanical point of view, such a system is truly two-dimensional. Fig. 6.1 illustrates this situation.

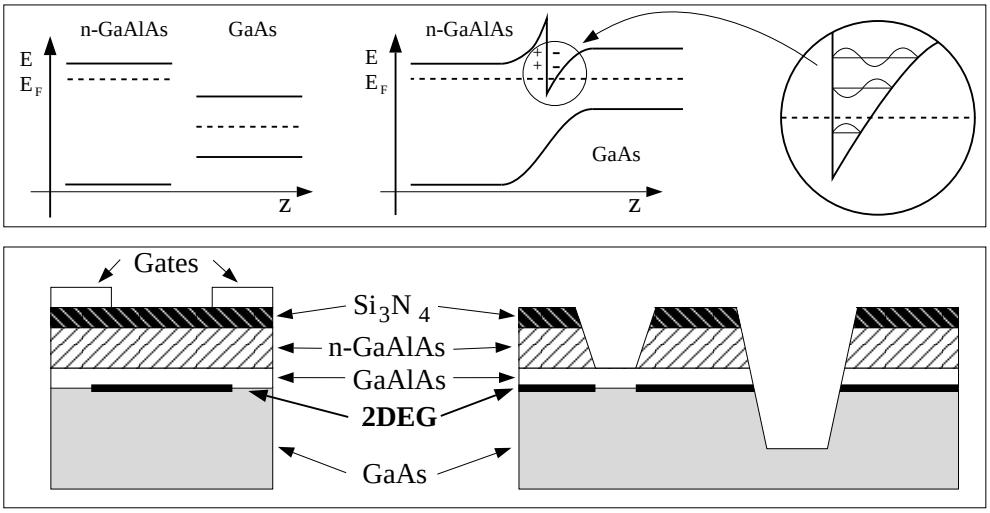

Figure 6.1: *Upper part: The mechanism leading to a 2DEG at the interface. Lower part: An undoped spacer layer between GaAs and n-GaAlAs reduces impurity scattering at the donors. The 2DEG can additionally be laterally confined by electrostatic gates (left), shallow etching (middle) or deep etching (right).*

Implementing the donors at a distance from the interface extremely reduces the impurity scattering. At low temperatures, where electron-phonon scattering can be neglected, this is nevertheless the dominant scattering mechanism. This comes about as semiconductors can nowadays be produced with extremely low contaminations and lattice defects. The latter is facilitated by the nearly identical lattice constants of GaAs and GaAlAs. For these reasons, the mobility of those devices can be extremely high. The mean-free path in state-of-the-art samples exceeds 10μm.

An additional lateral confinement of the 2DEG is possible either by etching or by applying electrostatic gates. By electron beam lithography structures in the 10nm regime can be defined. This is comparable to the Fermi wavelength, which is typically of the order of some 10nm.

6.2 The classical conductivity

In the classical picture, an external electric field accelerates the electrons. Due to impurity collisions, they acquire an average drift velocity $\vec{v}_d = -\mu\vec{E}$. The mobility μ is related to the scattering time τ_s via $\mu = e\tau_s/m^\star$, and the mean-free path is given by $\ell = v_F\tau_s$. The classical magnetoconductivity can be derived using the Einstein relation

$$\widetilde{\underline{\sigma}} = e^2\, g(E_F)\, \underline{D}\,, \tag{6.1}$$

where g denotes the level density and $\underline{D}$ the diffusion tensor. $\underline{D}$ can be evaluated within linear response, leading to [103]

$$D_{ij} = \int_0^\infty dt\, \langle v_i(t)\, v_j(0)\rangle\,, \tag{6.2}$$

where the brackets denote an average over the Fermi surface. This finally leads to the Drude conductivity tensor (for a detailed derivation see e. g. Ref. [99])

$$\widetilde{\underline{\sigma}} = \frac{\sigma_0}{1+(\omega_c\tau_s)^2}\begin{pmatrix} 1 & -\omega_c\tau_s \\ \omega_c\tau_s & 1 \end{pmatrix} \quad ; \quad \sigma_0 = \frac{n_s e^2\tau_s}{m^\star} = n_s e\mu\,. \tag{6.3}$$

The symmetry of the system enforces $\widetilde{\sigma}_{xx} = \widetilde{\sigma}_{yy}$ and $\widetilde{\sigma}_{xy} = -\widetilde{\sigma}_{yx}$. Using Eq. (5.10), the resistivity tensor $\widetilde{\underline{\rho}}$ is given by

$$\widetilde{\underline{\rho}} = \rho_0\begin{pmatrix} 1 & \omega_c\tau_s \\ -\omega_c\tau_s & 1 \end{pmatrix} \quad ; \quad \rho_0 = \frac{1}{\sigma_0} = \frac{m^\star}{n_s e^2\tau_s}\,. \tag{6.4}$$

The classical longitudinal resistivity $\widetilde{\rho}_{xx} = \rho_0 = m^\star/(n_e e^2\tau_s)$ is independent of the magnetic field. Experimentally, the classical limit is recovered in the low-field regime. Therefore the measurement of $\widetilde{\rho}_{xx}|_{B=0}$ is a convenient way to determine the mobility μ (and thus the scattering time τ_s). The Hall resistivity $\widetilde{\rho}_{xy} = B/(en_s)$ is proportional to the magnetic field, which is consistent with the usual definition of the Hall resistance.

In analogy to the smooth part of the level density $\widetilde{g}$ considered above, the classical (smooth) part of the conductivity (resistivity) of the free 2DEG according to Eq. (6.3) (Eq. (6.4)) is denoted with a tilde.

6.3 Leading order in $\hbar$

The trace formula for the oscillating part of the conductivity given in Sec. 5.5 is, just as the Gutzwiller trace formula, only valid for isolated periodic orbits. An extension to the case of the free 2DEG with its two-dimensional translational symmetry is possible using an approach analog to Creagh and Littlejohn's treatment of the level density for systems with continuous symmetries (see Sec. 2.3, especially Eq. (2.15)). Alternatively one can proceed as for the calculation of the level density associated with the cyclotron orbits (cf. Sec. 4.2.1.3). Both approaches reduce the problem to a one dimensional harmonic oscillator with an additional factor

$$\kappa = V\cdot\frac{eB}{2\pi\hbar} \tag{6.5}$$

from integration over the symmetry. The cyclotron orbit is the only primitive periodic orbit of the system, so that the sum over all orbits in the trace formula reduces to the sum over its repetitions. The velocity-velocity correlation of the primitive periodic orbit according to Eq. (5.7) can be calculated analytically, resulting in

$$\mathcal{C}_{xx} = R_c^2 \pi \frac{\omega_c \tau_s}{1+(\omega_c\tau_s)^2} \quad \text{and} \quad \mathcal{C}_{xy} = R_c^2 \pi \frac{(\omega_c\tau_s)^2}{1+(\omega_c\tau_s)^2} , \tag{6.6}$$

with the cyclotron frequency $w_c = eB/m^\star$ and the cyclotron radius $R_c = \hbar/eB \cdot \sqrt{4\pi n_s}$. Inserting all this into Eq. (5.4) and denoting the period of the primitive orbit with $T_0 = 2\pi/\omega_c$ results in

$$\begin{aligned} \delta\sigma_{xx} &= 2 \quad \frac{\sigma_0}{1+(\omega_c\tau_s)^2} \sum_{p=1}^{\infty} R(pT_0) e^{-p^2 T_0/2\tau_s} \cos\left[2\pi p\left(\widetilde{E}-\frac{1}{2}\right)\right] \\ \delta\sigma_{xy} &= -2\,\frac{1}{\omega_c\tau_s} \frac{\sigma_0}{1+(\omega_c\tau_s)^2} \sum_{p=1}^{\infty} R(pT_0) e^{-p^2 T_0/2\tau_s} \cos\left[2\pi p\left(\widetilde{E}-\frac{1}{2}\right)\right] . \end{aligned} \tag{6.7}$$

The relation between σ_{xx} and σ_{xy} is remarkable: Both the classical contributions according to Eq. (6.3) and the oscillating parts of Eq. (6.7) are proportional to each other, but with inverse factors:

$$\widetilde{\sigma}_{xy} = -\omega_c\tau_s \cdot \widetilde{\sigma}_{xx} , \quad \text{and} \quad \delta\sigma_{xy} = -1/(\omega_c\tau_s) \cdot \delta\sigma_{xx} . \tag{6.8}$$

In the strong field limit the classical Hall conductivity thus dominates over the longitudinal conductivity ($\widetilde{\sigma}_{xy} \gg \widetilde{\sigma}_{xx}$), and the quantum oscillations in σ_{xy} are suppressed compared to the oscillations in σ_{xx} ($\delta\sigma_{xy} \ll \delta\sigma_{xx}$).

On Landau levels, the normalized energy $\widetilde{E}$ in Eq. (6.7) is identical to the Landau quantum number. For spin-less particles it is therefore given by $\widetilde{E} = E_F/(\hbar\omega_c) = 2\pi\hbar n_s/(eB)$. Including spin leads to

$$\widetilde{E} = \frac{E_F}{\hbar\omega_c} + s g^\star \frac{1}{2}\frac{m^\star}{m_e} , \tag{6.9}$$

with the spin quantum number s and the Landé g-factor $g^\star$ of the material. For the 2DEG in GaAs, $s = \pm 1/2$ and $g^\star m^\star/m_e \approx -0.0293$. This corresponds to a spin splitting of $\approx 1.5\%$ of the Landau level separation, which usually cannot be detected. For InAs, in contrast, $g^\star m^\star/m_e \approx 0.338$, leading to a separation of the two spin peaks of $\approx 17\%$ of the Landau level distance. This explains why in GaAs/GaAlAs heterostructures the spin is generally neglected. Including spin, the contributions of the spin-subsystems to $\delta\underline{\sigma}$ have to be added. As obvious from Eq. (6.9), the inclusion of spin only leads to a shift of the Landau levels. Since within this approach no additional spin-related effects are included, the discussion of Eq. (6.7) can be restricted to spin-less particles without loss of generality.

The total resistivity $\underline{\rho} = \underline{\sigma}^{-1}$ is found by adding the classical part according to Eq. (6.4) and the semiclassical approximation of the quantum oscillations of Eq. (6.7), i. e.

$$\underline{\sigma} = \underline{\widetilde{\sigma}} + \delta\underline{\sigma} . \tag{6.10}$$

For the longitudinal conductivity σ_{xx}, the quantum mechanical self-consistent Born approximation for short-range scatters [9, 87] in the low-field regime $\omega_c\tau_s < 1$ is equivalent to this semiclassical result.

In Fig. 6.2 the result of Eq. (6.7) for ρ_{xx} and ρ_{xy} is shown for a system with electron density $n_s = 1.0 \cdot 10^{16}\mathrm{m}^{-2}$ and mobility $\mu = 100\mathrm{m}^2\mathrm{V}^{-1}\mathrm{s}^{-1}$ at a temperature of 10K. The classical resistivity (solid) is compared to the semiclassical description (dashed). The quantum oscillations to ρ_{xx} are seen to be an important correction in large fields. They give rise to the Shubnikov-de-Haas (SdH) oscillations.

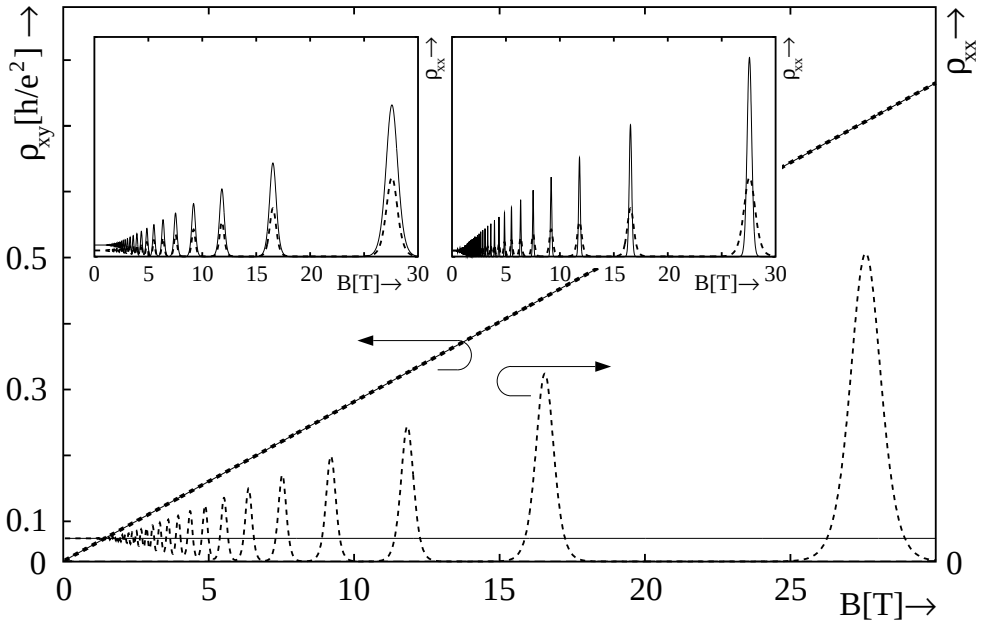

Figure 6.2: *The diagonal and the Hall resistivity of the free 2DEG. Solid: classical result of Eq. (6.4); dashed: semiclassical results according to Eqs. (6.10, 6.7, 6.4). The SdH oscillations in the longitudinal resistivity are well reproduced, but the QHE is not recovered in the semiclassical approximation. Insets show the influence of mobility (left) and temperature (right) on ρ_{xx}. Dashed: results of the central graphic ($\mu = 100\mathrm{m}^2\mathrm{V}^{-1}\mathrm{s}^{-1}$, $T = 10\mathrm{K}$); solid: $\mu = 50\mathrm{m}^2\mathrm{V}^{-1}\mathrm{s}^{-1}$ (left inset), $T = 3\mathrm{K}$ (right inset).*

The dependence on the scatterer density is illustrated in the left inset. The dashed line repeats the result of the main graphic with $\mu = 100\mathrm{m}^2\mathrm{V}^{-1}\mathrm{s}^{-1}$, whereas the solid line corresponds to $\mu = 50\mathrm{m}^2\mathrm{V}^{-1}\mathrm{s}^{-1}$. The zero field resistance is, as expected from Eq. (6.4), inverse proportional to the mobility. The amplitude of the SdH oscillations increases with lower mobility, and their relative width remains essentially unchanged. This is not consistent with the general accepted picture of the SdH oscillations. An increased scatterer density extends the region of localized states between the Landau levels, pushing the mobility edges closer to the Landau levels. This leads to sharper peaks in ρ_{xx}. The localization of states is semiclassically due to periodic orbits which include scattering events. As pointed out in Sec. 5.2, those have been neglected in the derivation of the semiclassical Kubo formula. Therefore the semiclassical approximation for the diffusive limit can not be expected to describe the SdH line widths correctly.

The right inset shows the influence of temperature. The dashed line repeats the result of the central graphic for $T = 10\mathrm{K}$, whereas the solid line corresponds to $T = 3K$. The SdH oscillations get sharper for lower temperatures. High temperatures lead, as expected, to

the classical limit $\rho_{xx} = \rho_0$. This is the correct temperature dependence.

In conclusion, the longitudinal resistivity of the 2DEG is well approximated by the semiclassical Kubo formula. It only fails to reproduce the correct dependence of the peak widths on the mobility. This is due to the neglect of periodic orbits including scattering.

In contrast to the successful description of ρ_{xx}, the semiclassical approximation of the Hall resistivity is inadequate. The semiclassical correction to the off-diagonal resistivity Eq. (6.7) plotted in Fig. 6.2 is completely negligible. It does not reproduce the integer quantum Hall effect (QHE).

6.4 $\hbar$ correction from the level density

The failure of the semiclassical description for ρ_{xy} might be due to the restriction to leading order in $\hbar$. Higher-order corrections can be implemented by going back to the quantum mechanical formula for the linear transport properties proposed by Středa [75]:

$$\begin{aligned} V \cdot \sigma_{xx} &= \pi e^2 \hbar \,\mathrm{Tr}[v_x \delta(E-H) v_x \delta(E-H)] \qquad (6.11) \\ V \cdot \sigma_{xy} &= e\,\frac{\partial N(E,B)}{\partial B} + \frac{i}{2} e^2 \hbar \,\mathrm{Tr}[v_x G^+(E) v_y \delta(E-H) - v_x \delta(E-H) v_y G^-(E)] \,. \end{aligned}$$

Here $G^{\pm}$ denotes the advanced and retarded Green's function, respectively. The second term of σ_{xy} is analog to the expression for σ_{xx}. This well approximated by the semiclassical Kubo formula, indicating that higher-order corrections to this term are irrelevant.

In the following, a higher-order correction to $\partial N/\partial B$ shall be derived. It should not be restricted to the free 2DEG, so that the general form of a semiclassical level density is chosen as starting point:

$$\delta g(E) = \frac{1}{\hbar^{(k+2)/2}} \sum_{\mathrm{po}} A_{\mathrm{po}}\, T_{\mathrm{ppo}} \cos\left(\frac{S_{\mathrm{po}}}{\hbar} - \mu_{\mathrm{po}} \frac{\pi}{2}\right) \,, \qquad (6.12)$$

The damping terms due to temperature and impurities as well as other prefactors are included in the amplitudes A_{po} for notational convenience. The volume term of the Thomas-Fermi level density, which gives the leading contribution to the smooth part of $g(E)$, is independent of the magnetic field. Therefore only the oscillating part of the level density contributes to $\partial N/\partial B$. Using

$$\delta N(E,B) = \int_0^{E_F} \delta g(E,B)\, dE \,, \qquad (6.13)$$

the semiclassical approximation for the first term in Eq. (6.11) can be expressed as

$$\begin{aligned} \delta\sigma_{xy}^I &:= e\,\frac{\partial N(E,B)}{\partial B} = e\,\frac{\partial[\delta N(E,B)]}{\partial B} \qquad (6.14) \\ &\approx -\frac{e}{\hbar^{(k+2)/2}} \sum_{\mathrm{po}} \frac{1}{p} \frac{\partial}{\partial B} \int_0^{E_F} A_{\mathrm{po}}(E,B) \frac{\partial S_{\mathrm{po}}}{\partial E} \cos\left(\frac{S_{\mathrm{po}}(E,B)}{\hbar} - \mu_{\mathrm{po}}\frac{\pi}{2}\right) dE \\ &= -\frac{e}{\hbar^{(k+2)/2}} \sum_{\mathrm{po}} \frac{1}{p} \frac{\partial}{\partial B} \int_{S(0,B)}^{S(E_F,B)} A_{\mathrm{po}}(S,B) \cos\left(\frac{S_{\mathrm{po}}(S,B)}{\hbar} - \mu_{\mathrm{po}}\frac{\pi}{2}\right) dS \,. \end{aligned}$$

In the second line it was used that the period of an orbit is given by $T_{\mathrm{po}} = p \cdot T_{\mathrm{ppo}} = p \cdot \partial S_{\mathrm{ppo}}/\partial E$, where p denotes the winding number. The last step assumed that the action $S(E,B)$ is invertible[1], so that $E(S,B)$ is uniquely defined for all S and B. The integral over S can be performed by subsequent partial integration. The partial derivative with respect to B acts both on the semiclassical amplitude of the orbit and on the action.[2] Taking these derivatives and sorting the terms in powers of $\hbar$ finally leads to

$$\delta\sigma_{xy}^{I} \approx \frac{-e}{\hbar^{(k+2)/2}} \sum_{\mathrm{po}} \frac{1}{p} \left[A_{\mathrm{po}} \frac{\partial S_{\mathrm{po}}}{\partial B} \cos\left(\frac{S_{\mathrm{po}}}{\hbar} - \mu_{\mathrm{po}} \frac{\pi}{2} \right) \right]_{E=0}^{E=E_F} + \delta\sigma_{xy}^{\hbar} \,, \tag{6.15}$$

$$\delta\sigma_{xy}^{\hbar} = \frac{-e}{\hbar^{(k+2)/2}} \sum_{\mathrm{po}} \frac{1}{p} \left[\sum_{i=1}^{\infty} \hbar^i \cos\left(\frac{S_{\mathrm{po}}}{\hbar} - \mu_{\mathrm{po}} \frac{\pi}{2} + i\frac{\pi}{2} \right) \times \right.$$

$$\left. \times \left\{ \left(\frac{d^i}{dS^i} A_{\mathrm{po}}(S,B) \right) \frac{\partial S_{\mathrm{po}}}{\partial B} - \frac{\partial}{\partial B} \left(\frac{d^{i-1}}{dS^{i-1}} A_{\mathrm{po}}(S,B) \right) \right\} \right]_{E=0}^{E=E_F} .$$

The leading order in $\hbar$ is given by the first term of $\delta\sigma_{xy}^{I}$ in Eq. (6.15). If the contribution of the lower integration limit vanishes, this reproduces the term $1/e\,\partial S/\partial B$ of the semiclassical Kubo formula Eq. (5.4). $\delta\sigma_{xy}^{\hbar}$ gives a series of $\hbar$-corrections.

The starting point of this derivation is given by the semiclassical level density, which by itself is only valid in leading order in $\hbar$. Higher-order corrections to δg entail additional terms to Eq. (6.15). If the semiclassical approximation of the level density of the system is good, $\delta\sigma_{xy}^{\hbar}$ as given in Eq. (6.15) contains the dominant corrections.

For the free 2DEG this condition is fulfilled, since the semiclassical approximation of its level density is exact (cf. Sec. 4.2.1.3). For this system all $\hbar$ corrections to $\delta\sigma_{xy}^{I}$ are included in Eq. (6.15).[3] The relevance of the $\hbar$ corrections in Eq. (6.15) for the conductivity tensor of the free 2DEG shall now be discussed.

By writing the prefactors of the level density Eq. (4.11) as a product of dS/dE and an amplitude, Eq. (6.15) can be applied to the free 2DEG.[4] Including explicitly finite temperature and impurities by appropriate damping terms, the result reads

$$\begin{aligned} \delta\sigma_{xy}^{I} &= \frac{2en_s}{B} \sum_{p=1}^{\infty} R(pT_0) e^{-p^2 T_0/2\tau_s} \cos\left[2\pi p \left(\widetilde{E} - \frac{1}{2} \right) \right] + \delta\sigma_{xy}^{\hbar} \,, \\ \delta\sigma_{xy}^{\hbar} &= -\frac{e^2}{h\pi} \sum_{p=1}^{\infty} \frac{1}{p} R(pT_0) e^{-p^2 T_0/2\tau_s} \sin\left[2\pi p \left(\widetilde{E} - \frac{1}{2} \right) \right] . \end{aligned} \tag{6.16}$$

The period of the primitive cyclotron orbit is given by $T_0 = 2\pi m/(eB)$. The first term of $\delta\sigma_{xy}^{I}$ is the leading-order contribution in $\hbar$[5]. It is already included in the trace formula Eq. (6.7).[6] Only the first term of Eq. (6.15) is nonzero, so that for the 2DEG only

[1] The general case is that $S(E,B)$ can only be piecewise inverted. The following derivation can be extended to this situation. This introduces only the inconvenience to notate the correct branch or, if necessary, the sum over the relevant branches.

[2] If the Maslov index μ_{po} is replaced by the reflection phase φ_R, a third term shows up in the following calculation, since φ_R depends on B and E.

[3] The other terms of Eq. (6.11), of course, may give rise to additional higher-order contributions.

[4] Alternatively, $\delta\sigma_{xy}^{I}$ can be directly evaluated from δg of Eq. (4.11).

[5] Note that the sheet density contains powers of $\hbar$, since $n_s = E_F m/(2\pi\hbar^2)$.

[6] Note that $\frac{en_s}{B} = \frac{\sigma_0}{w_c\tau_s}$ and $\frac{1}{w_c\tau_s} - \frac{w_c\tau_s}{1+(w_c\tau_s)^2} = \frac{1}{w_c\tau_s[1+(w_c\tau_s)^2]}$ to compare with Eq. (6.7).

corrections in second leading order $\hbar$ show up. The prefactor of $\delta\sigma_{xy}^{\hbar}$ compared to the prefactor of $\delta\sigma_{xy}^{I}$ increases linearly in B. Therefore this correction, although of lower order in $\hbar$, becomes dominant in strong fields.

The influence of this $\hbar$ correction is presented in Fig. 6.3. The solid line indicates the semiclassical result in leading order in $\hbar$, as given above. The dashed line includes the correction of $\delta\sigma_{xy}^{\hbar}$. The semiclassical trace formula now reproduces the plateaus in the Hall resistance, i. e. the QHE. This shows that the quantum Hall effect is dominantly an effect of *second* leading order in $\hbar$. Its origin is the dependence of the period $T_{\mathrm{ppo}} = dS/dE$ on the magnetic field.

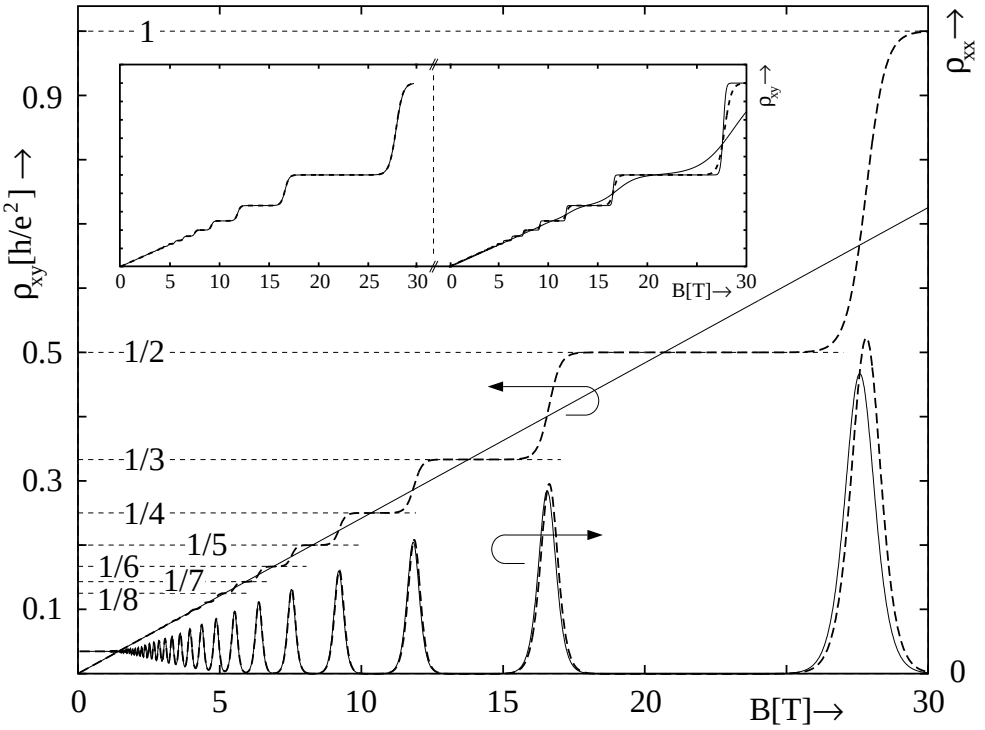

Figure 6.3: *The longitudinal and the Hall resistivity for the free 2DEG. Solid: semiclassical result in leading order in $\hbar$ as in Fig. 6.2; dashed: semiclassical result including the $\hbar$ correction of Eq. (6.16). The correction to the longitudinal resistance is negligible. The quantized conduction, however is purely an effect of second leading order in $\hbar$. Insets show the influence of mobility and temperature on ρ_{xy}. Dashed: results of the central graphic ($\mu = 100\mathrm{m}^2\mathrm{V}^{-1}\mathrm{s}^{-1}$, $T = 10K$); solid: $\mu = 50\mathrm{m}^2\mathrm{V}^{-1}\mathrm{s}^{-1}$ (left inset), $T = 3K$ and $T = 50K$ (right inset).*

The left inset shows the influence of the mobility on the QHE. The dashed line is a copy of the result shown in the the main graphic. It corresponds to $\mu = 100\mathrm{m}^2\mathrm{V}^{-1}\mathrm{s}^{-1}$. The solid line shows the data for $\mu = 50\mathrm{m}^2\mathrm{V}^{-1}\mathrm{s}^{-1}$. The Hall resistivity is hardly influenced by the amount of disorder. This does not agree with the established picture of the QHE, where the width of the localized states, and thus the width of the Hall plateaus, depends on the impurity concentration. The reason for this deficiency of the semiclassical approximation in the non-ballistic regime has already been given discussing the peak widths of the SdH oscillations above. Additionally, the validity of the present inclusion of finite free path-lengths is, as stated in Sect. 3.1, limited to the leading order in $\hbar$. It thus cannot be expected that this simple formalism reproduces the behaviour of higher-order $\hbar$ terms

correctly.[7]

In the right inset of Fig. 6.3 the temperature dependence is depicted. The solid lines are calculated for $T = 3\text{K}$ and $T = 50\text{K}$, respectively. For low temperatures the step-function is approached, whereas large temperatures smear the steps until the classical linear result is recovered. The temperature is therefore correctly included in the semiclassical approximation.[8]

In conclusion, the semiclassical Kubo formula successfully explains the longitudinal conductivity of the 2DEG, but fails for the Hall component. The $\hbar$ corrections according to Eq. (6.15) are the key ingredients for a semiclassical description of the Hall conductivity. The term in second leading order in $\hbar$ is responsible for the integer quantum hall effect. Including this term, the semiclassical Kubo formula explains both the Shubnikov-de-Haas oscillations and the QHE. It also reproduces the temperature dependence of these effects correctly. The approach is, however, limited to the ballistic regime. It therefore fails for effects that are related to localization, like the dependence of the QHE plateau width on the mobility. To describe these dependencies, periodic orbits which include scattering events would have to be taken into account.

The discussion of the Hall resistivity was restricted to the free 2DEG. The higher-order $\hbar$ corrections, however, were derived for arbitrary systems. They are not only relevant for samples which exhibit cyclotron-like orbits. For arbitrary systems, $\delta\sigma_{xy}^{\hbar}$ contains the relevant corrections if the semiclassical description of δg is sufficiently good, i. e. the higher-order $\hbar$ contributions to the *level density* can be neglected. Since this condition is frequently fulfilled, it is justified to include at least the second leading order term of Eq. (6.15) in all semiclassical descriptions of the Hall conductivity.

[7] Note that in this situation the procedure of Sect. 3.3 cannot be applied, since it starts out from the assumption that the line shape is known. The calculation of line shapes (or Hall plateaux widths) is thus obviously beyond the scope of this approach.

[8] This had to be expected, since the inclusion of finite temperature is exact for grand canonical systems as long as phonon scattering can be neglected (cf. Sect. 5.4).

Chapter 7

The channel with antidots

This chapter studies the longitudinal magnetoconductance of a mesoscopic channel with a central antidot dimer. The experimentally observed conductance oscillates in dependence of both the magnetic field strengths and the antidot radius (regulated by the applied gate voltage). The period of the oscillations in B is approximately constant, and the maxima positions exhibit characteristic dislocations when varying the antidot diameter. This behavior was previously related to inherent quantum effects and believed not to be accessible by semiclassical methods. The semiclassical description developed in this chapter is able to reproduce qualitatively as well as quantitatively all observed features. Additionally, it allows an intuitive explanation of the origin of the maxima dislocations.

Contents

Many physical observations in mesoscopic ballistic devices could successfully be explained by the interference of classical orbits in the system. Among these are the Shubnikov-de-Haas oscillations and the QHE of the free 2DEG discussed in the previous chapter, the magnetoconductance oscillations of a 2DEG in an antidot superlattice [84, 55] and those of a large circular quantum dot [62]. Also the current oscillations in a resonant tunneling diode (RTD) [114] could be described in these terms. There is, however, an ongoing discussion which effects can be treated using semiclassical methods, and which are of genuine quantum origin (i. e. of higher than leading order in $\hbar$).

The experimental observations of a mesoscopic channel with a central antidot molecule (a dimer) have been reproduced by a quantum calculation [48]. The authors related the measured magnetoconductance features to inherent quantum effects. They therefore claimed that the features are not accessible by semiclassical approximations. This motivates a more detailed examination whether the observations of this system are really beyond the limit of a semiclassical description.

A second reason for working out a semiclassical approximation of this structure is that it has a mixed phase space. The bifurcations which occur in those systems lead to divergencies in a leading-order $\hbar$ approximation. Much interest has been focused on the implementation of bifurcations in semiclassical approximations (see for example Ref. [71] and the references cited therein) and to track down their influence on experimental quantum oscillations. In the RTD, for example, period-doubling bifurcations were found to be responsible for a period doubling in the oscillations of the observed I-V curves [114]. The examination of the channel system will, as it exhibits bifurcations, contribute to this discussion.

Finally, the quantum calculations for the channel were able to reproduce its main features. They are, however, numerically so demanding that the dependence on the external variables could only be varied on a relatively coarse grid. For semiclassical calculations these restrictions will be considerably less tight. Within such a description, even a fit of the effective potential of the system could be feasible.

These three points make the channel system a real challenge to semiclassics.

7.1 The device

The device consists of electrostatic gates confining a high-mobility 2DEG in a GaAs/GaAlAs heterostructure. The 2DEG was 82nm beneath the surface, its electron density was $n_e \approx 3.47 \times 10^{15} m^{-2}$, and the mobility about $100\mathrm{m}^2V^{-1}\mathrm{s}^{-1}$. The SEM picture of the

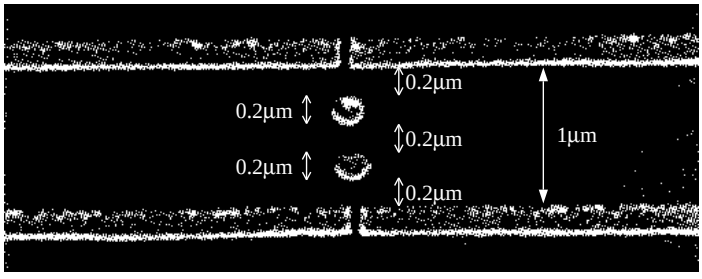

Figure 7.1: *SEM photograph of the gate structure. All gates were contacted separately in a later step. For the experiments discussed in this work, all channel gates are connected to the common gate voltage V_g, and the two antidots are biased with V_d.*

gate structure is shown in Fig. 7.1. Four metallized gates are used to define a long, narrow channel (5μm $\times 1\mu$m). Two circular gates with a diameter of 0.2μm at a distance of 0.2μm

from each other and from the channel gates define the antidot dimer. All gates are individually contacted using a bridge technique. Details about the device and its fabrication are presented in [33, 48, 34] and the references cited therein. All measurements were taken at $T \approx 100$mK using standard low-excitation AC-techniques. The magnetic field was applied perpendicular to the 2DEG.

7.2 Experimental results

This extremely versatile device was used for a variety of different experiments. The conductance was examined for the channel (using all four channel gates) and the half channel (using only the left channel gates). The antidot gate voltages were varied from the open channel to complete pinch-off, and the magnetic field range examined stretches from zero field to the high-field regime, where the quantum mechanical edge channel picture gets accurate. Applying gate voltages that pinch off all but one constriction establishes a quantum point contact (QPC) in the system. A lot of work was dedicated to the measurement of the quantized conductance effects of these QPCs. The corresponding experimental plateaus were also used to approximately scale the antidot voltages to an effective depletion width of both the antidots and the channel walls. Details on these experiments can be found in Refs. [34, 33, 35, 48, 47, 67].

For the experiments considered in this work, an identical voltage V_g, which was held fixed, was applied to all channel gates. Both antidot gates were given the same bias voltage V_d, which was the second parameter besides the magnetic field. The parameter range of interest for this thesis corresponds to large antidots which overlap, so that the central constriction is pinched off. The magnetic field is varied in the regime where the cyclotron diameter of the classical electron motion is comparable with the channel width. In the following, a short summary of the experimental findings relevant for this work will be given.

Fig. 7.2(a) shows a typical magnetoconductance trace measured for large antidots. The longitudinal conductance G_{xx} is near 4 conductance units e^2/h for most field strengths, dropping to approximately half the value in a sharp peak. The peak position corresponds to the commensurability of the size of the antidot dimer and the classical cyclotron diameter (marked with arrows)[1]. Note that this is completely analogous to the commensurability peaks observed in antidot lattices [84, 55]. Fig. 7.2(b) gives a closeup of the peak (boxed region in (a)). Superimposed on the peak, quantum oscillations with an approximately constant period can be observed. This is studied in more detail in (c), where the spacings of the neighboring conductance maxima are plotted as a function of B. The different curves correspond to slightly different antidot voltages. The average spacing of the maxima is nearly constant, only slightly decreasing with stronger fields. Superimposed on this smooth trend random like variations are observed.

The unique design of the sample with individually contacted gates allows to change the voltages of the antidots without affecting the other system properties. This was exploited to measure the influence of the antidot diameter, which is directly related to the applied voltage via the induced depletion width. Fig. 7.2(d) shows the influence of this parameter. The points in the diagram correspond to the positions of the maximum of G_{xx}, the solid

[1] The antidot size is determined by the lowest point of the saddle of the model potential (defined below in Eq. (7.1), with $s_d = 2$ and $s_g = 1$).

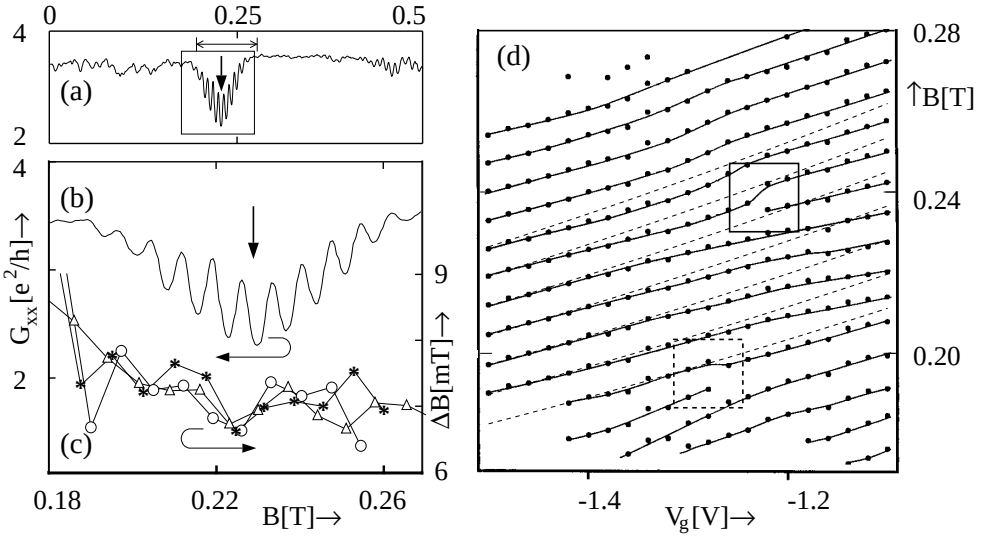

Figure 7.2: *Experimental results. (a,b) Magnetoconductance trace for $V_g = -1.44\,V$. The vertical arrows indicate the commensurability condition (see main text). (c) Spacing of the conductance maxima for three gate voltages $V_g = -1.42 \ldots -1.5$ V. (d) Dots correspond the positions of the conductance maxima in dependence of B and V_g. Solid lines are to guide the eye. Dashed lines are calculated from the simple picture described in Sec. 7.3.1.*

lines are just to guide the eye. For smaller antidot voltage the maxima move to stronger fields. They shift mostly parallel, interrupted by characteristic dislocations (boxes).

7.3 Theoretical description

7.3.1 Intuitive discussion

Some of the observed effects can immediately be understood on an intuitive level. A simple picture will clarify which of the features need more detailed discussion.

Since the central constriction is pinched off in the observed regime of antidot voltages, two QPCs are formed between the channel wall and the antidots. The first plateau of quantized conduction leads to a conductance of e^2/h per constriction and per spin, so that the value of $4e^2/h$ is expected if no interference takes place between the QPCs. If the cyclotron diameter equals the channel width, the electrons passing the lower constriction can be focused back through the upper constriction, so that the conductance falls to $2e^2/h$. Using the simple model potential defined below in Eq. (7.1), one can estimate the central peak position by assuming that the orbits are cyclotron-like, passing the saddle of the potential at the lowest point. A rough estimate of the peak width is given by the magnetic field strengths where cyclotron orbits pass the constriction at Fermi energy. These estimates are compared to the experimental G_{xx} in Fig. 7.2(a). The magnitude of the conductance, the position of the conductance dip (vertical arrow), and also its width (horizontal arrow) are in quantitative agreement with this simple consideration.

The oscillations superimposed on the peak may be explained in analogy to the Aharonov-Bohm (AB) effect. Identifying cyclotron orbits around the two central antidots with the AB ring, equidistant maxima in B are expected. Subsequent maxima correspond in

this picture to an additional flux quantum through the ring, so that their spacing only depends on the ring area. The experimentally observed $\Delta B \approx 7$mT (cf. Fig. 7.2(c)) corresponds to a diameter of the AB ring of $\approx 0.86\mu$m. This is consistent with the device dimensions extracted from the SEM photograph Fig. 7.1. Following this interpretation further, the conductance maxima are expected to shift to larger B fields if the antidot diameter is decreased. Taking the approximate scaling between V_g and depletion with s_d from Kirczenow *et al.* [48] allows a quantitative calculation of the expected effect.[2] The prediction of this simple model is shown in Fig. 7.2(d) with dashed lines. Considering the crude approximations made, the agreement with the experiment is remarkable.[3]

The questions which remain to be answered by a more detailed analysis concern the deviations from this simple behavior: (1) How does the spacing of the maxima change with B? (2) Which mechanism is responsible for the dislocations of the maxima positions?

7.3.2 Quantum mechanical calculation

Kirczenow *et al.* [48] presented a quantum mechanical calculation using a transfer matrix technique on a lattice. The model potential both for the channel and the antidot gates was chosen[4] as

$$V(r) = \begin{cases} E_F \left[r/a_0 - (1+s)\right]^2 & \text{for } r < a_0(1+s) \\ 0 & \text{otherwise} \end{cases} , \tag{7.1}$$

with $a_0 = 0.05\mu m$. Here r denotes the distance to the gate, and a_0 the length scale over which the potential falls of from E_F to 0, i. e. the diffuseness of the potential. s is a dimensionless parameter modeling the depletion width around the gates. For the gates defining the channel, $s = s_c = 1$ was used unless otherwise noticed. The conductance was obtained from the Landauer formula $g = (e^2/h)\mathrm{Tr}(\mathbf{t}\mathbf{t}^\dagger)$. The calculations were performed for $T = 0$ and neglecting impurity scattering. Therefore the quantum mechanical approach misses a smoothing of the data due to temperature and impurity effects.

The results relevant for the further discussion are reproduced in Fig. 7.3. (a) shows the magnetoconductance trace, (b) the variation of the maxima spacings, and (c) the positions of the maxima with varying antidot diameter. The quantum mechanical calculation (heavy lines) qualitatively reproduces both the saturation of the peak spacings and the maxima dislocations observed experimentally. Characteristic deviations are the shift of the conductance peak to higher B-fields, and correspondingly a shift of the ΔB versus B

[2] To establish a relation between the antidot diameter and the cyclotron radius, the cyclotron orbit is assumed to pass the constriction at a constant potential $0.6E_F$. This parameter is adapted so that ΔB matches the experiment. Note that ΔB can only be slightly modified by varying this parameter. The slopes with changing s_d are hardly affected at all.

[3] Note that Gould *et al.* [34] explained the shift of the conductance maxima by the reduced velocity of a particle in the constriction, which also leads to a change of the action of an orbit. The simple AB picture, however, explains already both the spacing of the maxima and their dependence on the antidot diameter. Therefore in this context no additional mechanism has to be introduced.

[4] The electrostatic potential induced by the gates is relatively smooth. The effective single-particle potential, however, gets steeper with increasing particle number. This has been shown in self-consistent calculations for quantum dots [24] and is analogous to the situation in three-dimensional metal clusters [32, 89]. In the limit of high electron densities, the effective potential is box-like. This ensures that the applied gate voltage only determines the depletion region of the gate, whereas the potential steepness depends mainly on the electron density. For the electron densities realized in the experiment, the choice of the model potential consisting of a flat central region with steep walls is justified.

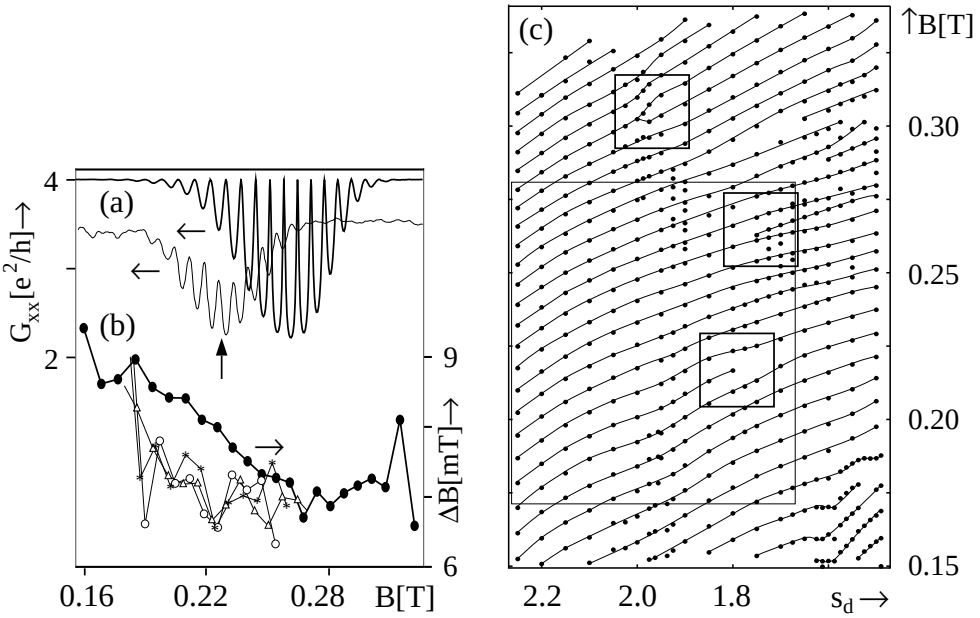

Figure 7.3: *Quantum results. (a) Magnetoconductance. Thick: QM for $s_d = 2.05$, thin: experiment with $V_g = -1.44$ V. The arrow indicates the commensurability condition in the model potential. (b) Spacing of the maxima for $s_d = 2.05$. The thin lines correspond to the experimental curves of Fig. 7.2. (c) Positions of the maxima in dependence of B and s_d. Small boxes indicate dislocations, the large box gives the approximate range of the corresponding experimental data of Fig. 7.2.*

curve. The lack of quantitative agreement could be due to the model potential, whose parameters were not adapted for a perfect fit. Note, however, that the central position of the peak does not coincide with the commensurability condition of the model potential (vertical arrow). The origin of this deviation is unclear.

7.4 Semiclassical description of the conductance

The initial motivation for a semiclassical analysis of this system was to find out whether the variation of the maxima spacings and the dislocations with varying antidot diameter are genuine quantum effects, i. e., of higher than leading order in $\hbar$. This was claimed in Refs. [48, 34] with two arguments: (1) All classical orbits found by the authors show a dependence of the action S on the magnetic field B which implies a decrease of ΔB with larger B. This contradicts the experimental results. (2) The experiment is performed in the regime of the first plateau of quantized conduction. With just one mode transmitting, a semiclassical approach seems questionable to the authors.

In this chapter, the semiclassical description of the magnetoconductance for the channel system is derived. The results are compared to the quantum mechanical data as well as to the experimental findings. It is discussed why the semiclassical description is – in contrast to the above arguments – able to explain all the experimentally observed features. Thereafter, the lower computational effort of the semiclassical ansatz is used to fit the model potential parameters to the experiment. The close relation of the trace formula to the classical dynamics of the system finally allows to explain all effects within a simple, intuitive picture.

7.4.1 Landauer-Büttiker or Kubo?

Although the quantum mechanical results of the Landauer-Büttiker and the Kubo formalism have shown to be identical [12], the appropriate formulation for a semiclassical approximation has to be chosen.

The Landauer-Büttiker approach [54, 21] is valid for completely phase-coherent devices connected to leads which serve as electron reservoirs. The conductance of such a system can be expressed in terms of the transmission coefficients between all the contact modes. This formalism holds for two-terminal measurements as well as for configurations including more contacts. The channel with central antidots consists of a phase-coherent "active region" (the environment of the antidots), connected by "leads" (the channel itself). Since these leads are not phase coherent (their lengths exceed the phase coherence length), they cannot be considered as part of the device. They are not in thermal equilibrium,[5] so that they are no contacts in the sense of the Landauer-Büttiker formalism, either. This approach is therefore not applicable to the present system.

The Kubo approach describes the conductivities of homogeneous, macroscopic samples. Since the channel is neither homogeneous nor macroscopic, it is not reasonable to define a conductivity for this system. Nevertheless, the Kubo formalism is applicable. This becomes clear considering a hypothetic system, namely a 2D lattice with the channel system as its elementary cell. This setup is equivalent to the antidot lattices regularly treated within Kubo formalism. The conductivities which are calculated from the Kubo formula refer to the macroscopic dimensions of the (hypothetical) lattice. Since the vertically separated elementary cells can not interfere because of the channel walls, and horizontally separated antidot dimers are further apart as ℓ_Φ, the classical scaling laws hold down to a single elementary cell of the lattice, i. e. can be applied to the individual channel with a pair of antidots. The conductance of the individual channel is therefore given by the conductivity in connection with the size of the elementary cell. Since the resistance of the channel itself is negligible, the relevant size is given by the active region, i. e. the region around the antidots.

In the following, the semiclassical version of the Kubo transport formula Eq. (5.4) will be applied to the channel with antidots.

7.4.2 The model potential

To allow a comparison of the results, the quantum mechanical model potential is also used for the semiclassical approach. Numerical stability, however, requires[6] smooth second derivatives of $V(\boldsymbol{r})$. The model potential Eq. (7.1) has a discontinuous second derivative between the flat bottom and the quadratic wall. To remove this, a cubic spline is introduced in the transition region. The total potential is given by

$$\frac{V(\tilde{\boldsymbol{r}})}{E_F} = \begin{cases} (|\tilde{\boldsymbol{r}}| - s_1)^2 + \frac{\Delta^2}{12} & |\tilde{\boldsymbol{r}}| < (s_1 - \Delta/2) \\ -\frac{1}{3\Delta}(|\tilde{\boldsymbol{r}}| - s_2)^3 & (s_1 - \Delta/2) < |\tilde{\boldsymbol{r}}| < (s_1 + \Delta/2) \\ 0 & (s_1 + \Delta/2) < |\tilde{\boldsymbol{r}}| \end{cases} \tag{7.2}$$

[5] This is especially clear for high magnetic fields where the current is carried by edge states. The states at the opposite edges of the channel have different Fermi energies in this regime.

[6] This is due to the numerical scheme implemented, which simultaneously integrates the stability matrix. It will be presented in appendix A.

with $\tilde{\boldsymbol{r}} = \boldsymbol{r}/a_0$, $s_1 = 1 + s$ and $\Delta = s_2 - s$. Throughout this chapter, $\Delta = 0.005$ is used. This results in a difference to the pure parabolic case smaller than $2.1 * 10^{-6} E_F$, which is negligible. The potential Eq. (7.2) is illustrated in Fig. 7.4. Unless otherwise noticed,

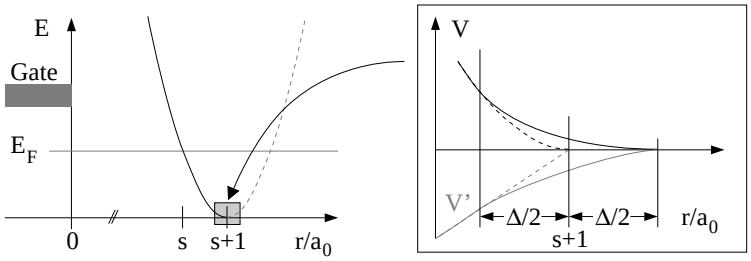

Figure 7.4: *Left: Model potential used for the semiclassical calculations. Right: Closeup of the transition region. Cubic spline correction (solid) and the piecewise parabolic case (dashed).*

the parameters are identical to those of the quantum calculation, i. e. $a_0 = 0.05\mu m$ and $s = s_c = 1$ for the gates defining the channel. The depletion width of the antidot gates s_d was varied between 1.5 and 2.2. Following the approximated relation between s_d and V_g in Ref. [48], this corresponds to an effective antidot diameter between 0.35μm and 0.42μm.

7.4.3 The periodic orbits

Except for a few special cases, the periodic orbits of a system with smooth potential can only be found numerically. This stage involves the main numerical effort of a semiclassical approximation, so that some care reducing the computation time is indicated. In order not to interrupt the discussion, the corresponding technical (though important) details are given in appendix A. The central idea is to implement a fast numerical differential equation solver to integrate *simultaneously* the classical equations of motion (EOM) and a reduced version of the monodromy matrix, the (2D) stability matrix $\widetilde{M}$. Starting with random initial conditions, a two-dimensional Newton-Raphson iteration using the information provided by $\widetilde{M}$ converges to the periodic orbits. These are followed with varying B-field and antidot diameter using an adaptive extrapolation scheme.

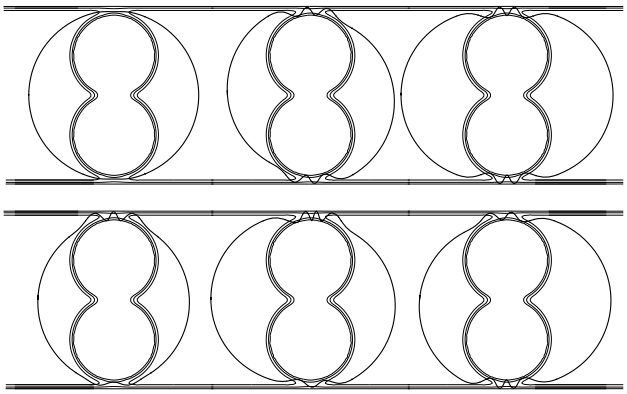

Figure 7.5: *Six typical classical periodic orbits in the channel system. Note that there are orbits breaking the symmetries of the potential.*

Although the potential is simple and symmetric, it gives rise to a large variety of distinct periodic orbits, many of them breaking the symmetry of the system. Some typical examples are shown in Fig. 7.5. According to Sec. 3.2, finite temperature and impurity scattering leads to a strong damping of the contributions of longer periodic orbits to the trace sum. Systems like the disk billiard (see chapter 4) or antidot lattices [63, 41] only have a small number of short periodic orbits. In these cases the evaluation of the semiclassical Kubo formula is especially easy, since only a few contributions are significant. In the channel, unfortunately, the lengths of the orbits are nearly identical, so that much more orbits contribute to the trace sum.

Most of the orbits do not exist over the whole parameter range, appearing and disappearing

in orbit bifurcations. Fig. 7.6 shows the typical behavior of $\mathrm{Tr}(\widetilde{M})$ of some orbits with varying magnetic field. The structure of the classical dynamics is astonishingly rich, showing bifurcations (which correspond to $\mathrm{Tr}(\widetilde{M}) = 2$) of various types and – when varying the antidot diameter s_d – also of higher codimension. The number of orbits increases rapidly with smaller antidot diameter (i. e., wider constriction).

The Poincaré plot of the channel is given in Fig. 7.7. The leftmost picture shows the stability island of a primitive orbit, surrounded by chains of stable and unstable orbits of higher repetition number, in the "sea of chaos". Varying the magnetic field drives the system through a bifurcation. The central stable orbit becomes unstable, creating a pair of new stable orbits (rightmost picture). This is the typical phase space picture of a period doubling (or pitchfork) bifurcation.

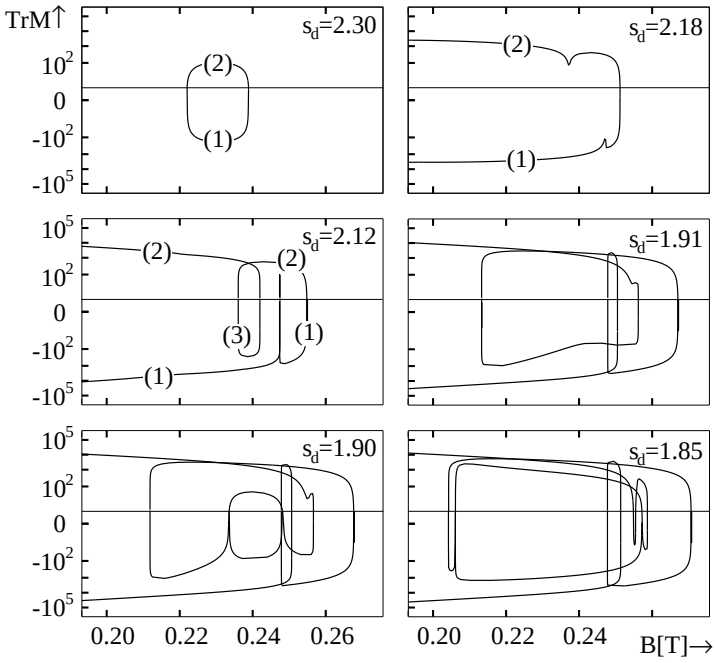

Figure 7.6: *The dependence of $Tr(\widetilde{M})$ of some periodic orbits on B and s_d. The crossings of the line $Tr(\widetilde{M} = 2)$ indicate bifurcations, where new orbits appear. The number of orbits increases rapidly with smaller antidot diameter s_d. The labels of the orbits refer to a classification in three generations, which will be used in Sec. 7.6.*

By checking $\mathrm{Tr}(\widetilde{M})$ as in Fig. 7.6, it was ensured that no orbit was missed at a bifurcation. All together, over 60 orbits (not counting the symmetry-related ones) have been included in the calculations. All relevant classical properties, namely the actions, periods, stabilities, velocity-velocity correlation functions, Maslov indices and degeneracies were determined numerically. The technical details are presented in appendix A.2.

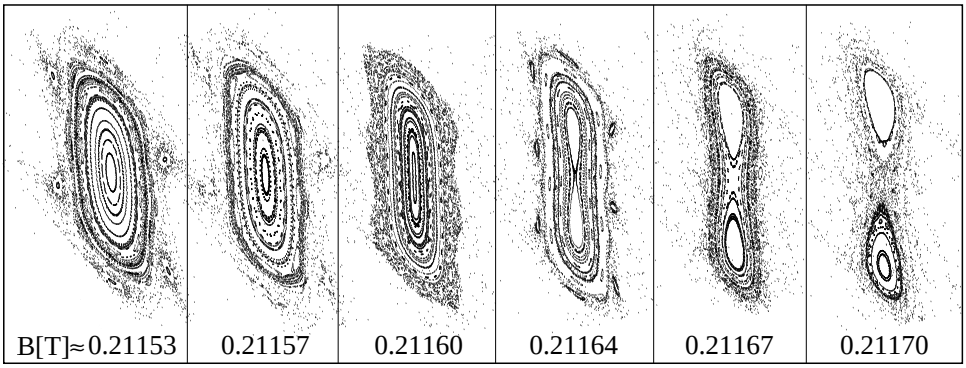

Figure 7.7: *Poincaré plot of a small phase-space region for $s_d = 1.9$ for varying B. From left to right: a stable orbit becomes unstable, creating two new stable orbits. The stable orbits are surrounded by chains of stable and unstable orbits with higher repetition number, which is typical for systems with mixed phase space.*

7.4.4 Evaluating the trace formula

As discussed in Sec. 2.4, leading-order $\hbar$ approximations diverge at bifurcations. This spurious behavior can be removed by a local higher-order expansion. To ensure both the correct local properties at the bifurcation and the (Gutzwiller-) limit far from it, uniform approximations can be used.

Orbit traces like in Fig. 7.6 allow the identification of the types of bifurcations present in the channel system. Varying the magnetic field both tangent and period doubling bifurcations occur. If additionally the antidot diameter is changed, bifurcations of codimension 2 show up as well. The explicit formulas for the uniform approximation of tangent bifurcations are given in appendix B by Eqs. (B.7) and (B.8). Eq. (B.15) applies to pitchfork bifurcations. The next section deals with the implications that these expressions do not only contain information about the classical periodic orbits, but also include the contribution of *ghost orbits*, i. e., analytic continuations of orbits beyond the regime where they classically exist.

7.4.4.1 Numerical implementation of the uniform approximation

The formulas for the uniform bifurcation cannot be applied directly to the system considered here. First, the channel has discrete symmetries, whereas these formulas apply to the generic, symmetry-free case. The discrete symmetry modifies the behavior of the period doubling bifurcation. Its generic form consists of a central orbit which changes its stability (from stable to unstable or vice versa), splitting off a new orbit with twice the period. In the channel system, in contrast, two symmetry-related orbits with the simple period split off (cf. Fig. 7.7 for a Poincaré plot). The total Gutzwiller amplitudes, however, are identical for the symmetric and the generic situation. The factor 2 from the double period in the generic case is replaced by the degeneracy factor 2 stemming from the symmetry. Including the degeneracies correctly, the uniform approximation of Schomerus and Sieber can be applied to the channel system.

The second problem concerns the numerical implementation of the uniform approximation. The information about the ghost orbits which contribute to the analytical formulation is not available if the classical equations of motion are integrated numerically. This prevents the application of the uniform approximation to the complex side of the bifurcation. This work suggest a modified scheme, which retains the correct limiting cases, but requires only information about real orbits. It consists of a local approximation at the bifurcation, which is adapted to both the local form of the uniform approximation and the limit on the far complex side (which is simply the Gutzwiller contribution of the remaining real orbits). The technical details of the procedure are presented in Appendix B.

7.4.4.2 The influence of the bifurcations

As can be deduced from the analytical local form, the contributions of the orbits engaged in a bifurcation are increased by a factor $\hbar^{-\delta}$. The exponent depends on the type of the bifurcation; for the tangent bifurcation $\delta = 1/6$, and for the period doubling bifurcation $\delta = 1/4$ [70]. This shows that bifurcations are of leading order in $\hbar$ and dominate in the semiclassical limit $\hbar/S \to 0$ (with S being the action of a typical periodic orbit in the system). Therefore it has to be checked whether the bifurcations have an increased influence on the conductance of the channel system.

Fig. 7.8(a) shows the trace of the (reduced) stability matrix $\mathrm{Tr}(\widetilde{\mathrm{M}})$ of three periodic orbits taking part in two successive bifurcations (where $\mathrm{Tr}(\widetilde{\mathrm{M}}) = 2$) under variation of the magnetic field strength B. At $\widetilde{B} \approx 0.21$ a tangent bifurcation, and at $\widetilde{B} \approx 0.225$ a pitchfork

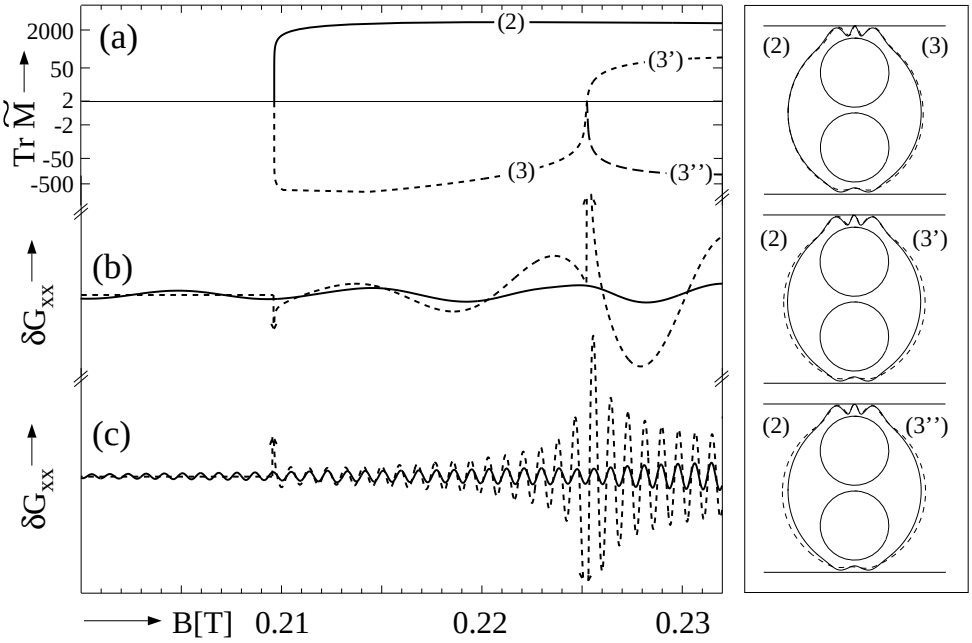

Figure 7.8: *(a) $Tr(\widetilde{\mathrm{M}})$ (note the nonlinear scale!) versus magnetic field B for three characteristic periodic orbits. (b) Contribution of the three orbits to δG_{xx}; dotted line: semiclassical Kubo formula, solid line: uniform approximation. (c) same as (b) but for a system with 10 times larger actions. The right box illustrates the orbits engaged in the bifurcations. Note the tiny differences to orbit 2.*

bifurcation shows up. Fig. 7.8(b) gives the contribution to the conductance of the orbits engaged in the bifurcations. The dotted line corresponds to the result of the semiclassical Kubo formula Eq. (5.4). The amplitudes are diverging at the bifurcations. The uniform approximation (solid line) removes, as expected, the divergences. Fig. 7.8(c) represents the corresponding data for a system scaled to have 10 times larger actions, thus being closer to the semiclassical limit. Even then, the amplitudes of the uniform approximation are nearly constant over the bifurcations. This shows that the bifurcations have no locally dominant influence on the conductance of the present system.

Having established this result, the semiclassical approximation can be further simplified. Whereas for individual orbits a uniform treatment of the bifurcations is vital, their influence becomes smaller if a larger number of orbits is included. This is demonstrated in Fig. 7.9, where δG_{xx} has been calculated including all relevant (~ 60) periodic orbits. The thin line gives the standard Gutzwiller-like approach in leading order in $\hbar$ according to Eq. (5.4). The sharp divergences correspond to bifurcations of various orbits included in the trace sum. The difference to the uniform result[7] (solid) is much less pronounced than in Fig. 7.8.

The influence of higher-order $\hbar$ corrections on the result of Gutzwiller-like trace formulae has been discussed in Sec. 3.3. There it was pointed out that $\hbar$ corrections do not only

[7]The numerical uniform approximation was additionally treated with the folding procedure of Sec. 3.3.2 to handle the spurious divergencies stemming from the bifurcations with codimension 2. Those were not included in the numerical uniform approximation.

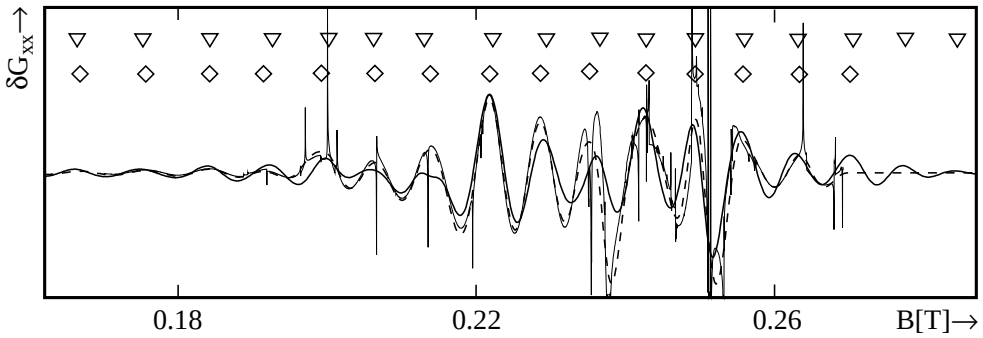

Figure 7.9: *δG_{xx} for $s_d = 1.88$ using the semiclassical Kubo formula either directly (thin) or with additional folding over B (dashed). The uniform approximation corresponds to the heavy solid line. Maxima are marked with diamonds (folded Kubo) and triangles (uniform).*

lead to additional terms in the trace sum, but also require an adaption of the smoothing scheme. This applies, as pointed out there, also to bifurcations. The correct inclusion of finite temperature and impurity scattering is possible using the folding approach presented in Sec. 3.3.2. This procedure implements the smoothing in higher order in $\hbar$, but it does not include higher-order $\hbar$ terms to the trace formula. Comparing the uniform approximation with the results of the semiclassical Kubo formula in combination with the folding approach therefore permits an examination of the effects of the higher-order $\hbar$ terms introduced by the bifurcations.

The dashed line in Fig. 7.9 shows the result of the folding approach. It removes the spurious divergencies at the bifurcations, and the remaining discrepancy to the uniform treatment is small. This is in strong contrast to Fig. 7.8, where only a few orbits are included. The semiclassical result therefore depends only little on the correct treatment of the bifurcations if many orbits are included. From this observation it can be deduced that the higher-order $\hbar$ corrections from the different bifurcations interfere mostly destructively. This effect has already been observed in the study of the disk billiard in chapter 4.

In particular, the influence of the bifurcations on the maximum positions (marked by diamonds and triangles in Fig. 7.9) is small. Therefore the semiclassical description can be further simplified by using the trace formula Eq. (5.4) with additional convolution over B. This will be done in the following.

7.5 Semiclassical results

The discussion of the simple Aharonov-Bohm (AB) picture in Sec. 7.3.1 has shown that the observations which still need to be explained are the dependence of the maximum spacings on B, and the dislocations of the maxima positions with varying antidot diameter. This will be discussed in Sec. 7.5.3 and 7.5.4, respectively. Before that, a closer look at the experimental results will be taken.

7.5.1 Fourier components of the quantum oscillations

The semiclassical trace formula Eq. 5.4 has the structure of a Fourier sum, with the periodic orbits as individual Fourier components. If the semiclassical approach is justified

and a formula of this type describes the quantum oscillations, the traces of the classical orbits should be visible in a Fourier transform of the experimental data. This technique has evolved to a standard approach for extracting the influence of the classical phase space structure on quantum oscillations. Prominent calculations of this type include the Rydberg spectrum of hydrogen [92] and of larger atoms [52]. This powerful method shall now be applied to the channel system in order to check whether the quantum oscillations show indications for the influence of classical orbits.

For such an analysis to be rigidly valid, a scaling law for the actions of the periodic orbits must hold. The observed conductance oscillations resemble Aharonov-Bohm oscillations. The action of the corresponding orbits, the cyclotron orbits, scales like $S = \kappa B$. Taking the Fourier transform of G_{xx} with respect to B, orbits with this scaling property show up as sharp peaks. Fig. 7.10 shows Fourier spectra[8] of the experimental data with respect to B for different antidot voltages. For large antidots (large negative voltage on the antidot gates) one dominant frequency can be observed. With decreasing antidot diameter, the corresponding peak shrinks and finally disappears. Simultaneously, a new peak develops at smaller ΔB. For $V_g \approx -1.24$ V both peaks have approximately equal strength. With decreasing antidot diameter, both peaks move to larger ΔB.

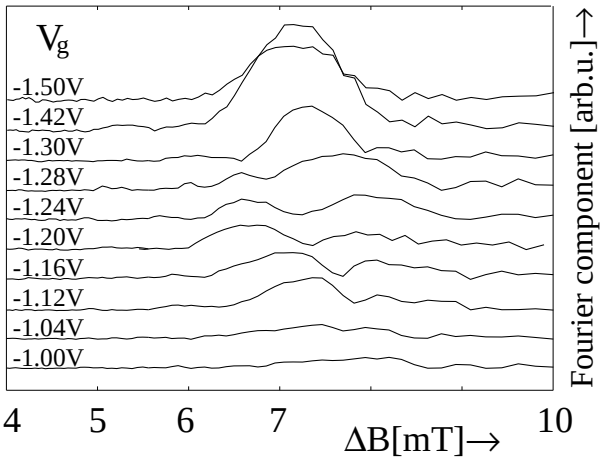

Figure 7.10: *Fourier transform of the experimental data in the range of the commensurability peak $B = 0 \ldots 0.5$ T. For easier comparison with Figs. 7.2 and 7.13, the frequency is given in units of the corresponding maxima spacing. Offset for clarity.*

The width of the peaks in Fig. 7.10 is not restricted by the finite resolution of the Fourier transform. This does not necessarily contradict a semiclassical interpretation. The broadening might be caused by orbits whose action scales only approximately like $S = \kappa B$. The widths of the peaks can also be explained by many orbits which contribute, each with a slightly different frequency. The Fourier data therefore neither gives a clear indication of periodic orbits contributing to the quantum oscillation, nor does it exclude this possibility.

The oscillations in G_{xx} seen in experiment (compare to Fig. 7.2) are nearly sinusoidal, so that one might expect that a single periodic orbit is responsible for the effect. The above Fourier analysis of the data shows, however, that at least two orbits contribute to the quantum oscillations.

7.5.2 The conductance variation with B

Fig. 7.11 compares the semiclassical result for the oscillating part of the conductance with the experimental[9] data.

[8] To clearly separate out the regime of interest around the commensurability peak, a triangular window function was used. The magnetic field range considered was $B = 0 \ldots 0.5$ T.

[9] To extract the oscillating part of the conductance from the the experimental data, the smooth part was calculated by convolution with a Gaussian with $\sigma = 0.004$ T. The difference to the original data gives δG_{xx}.

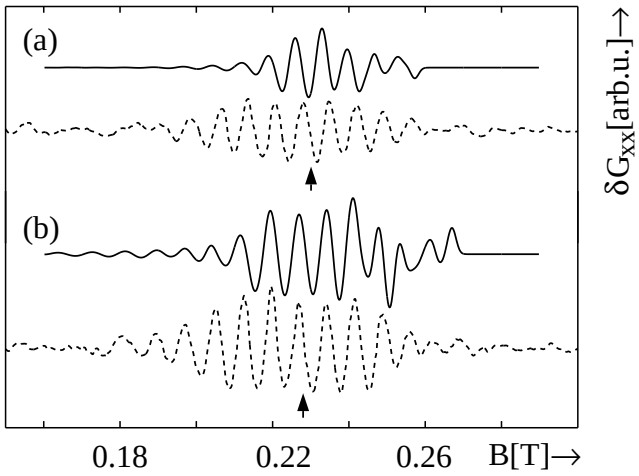

Figure 7.11: *Semiclassical (solid) and experimental data (dashed) for δG_{xx}. The arrows indicate the commensurability condition; offset for clarity. (a) Large antidot diameter. Semiclassics: $s_d = 2.06$, experiment: $V_g = -1.48$ V. (b) Intermediate antidot diameter. Semiclassics: $s_d = 1.91$, experiment: $V_g = -1.38$ V.*

The semiclassical result shows – apart from small shift towards higher magnetic fields – qualitatively the same behavior as the experimental data. Although using an identical model potential, this shift is considerably smaller than for the quantum calculation (compare to Fig. 7.3). The origin of this discrepancy between the two theoretical descriptions is unclear. Please note in this context that the quantum calculation in contrast to the semiclassical approach does not reproduce the correct position of the classical commensurability peak. This is clear comparing Figs. 7.3 and 7.11, where the commensurability conditions are indicated by vertical arrows.

The numerical effort involved in the semiclassical calculation is considerably smaller than for the quantum approach. It is low enough to make a fit of the model potential to the experimental findings feasible. For this task three parameters of the model system have been varied, namely the overall system size and the depletion widths of the channel and antidot gates, s_c and s_d. Since the classical dynamics are size-independent, the scaling of the system with a factor κ in coordinate space can simply be performed by replacing in Eq. (5.4) the action S with κS and the magnetic field B with $\kappa^{-1}B$. To change s_c, the periodic orbits have to be adapted to the new potential using the same scheme already employed when varying B or s_d (see appendix A.3).

Fig. (7.12) shows the semiclassical conductance for $s_c = 1.5$ and $s_d = 1.5$ for a system scaled with $\kappa = 1.075$, i. e. $s_0 = 0.05375\,\mu$m. This size is still in agreement with the SEM picture Fig. 7.1. The adapted model potential removes the mismatch between the semiclassical and the experimental findings, resulting in a quantitative[10] agreement of the semiclassical δG_{xx} with the experimental data.

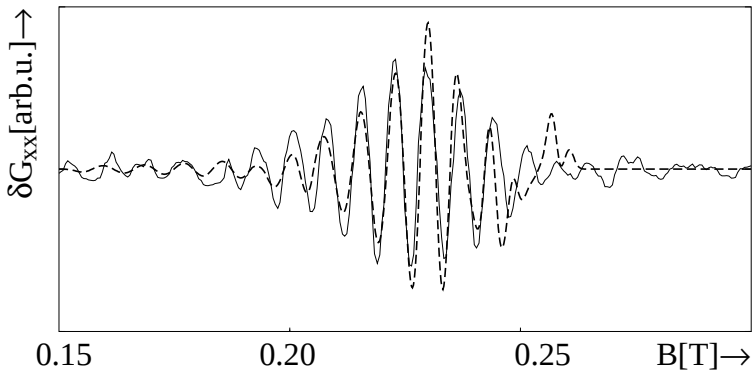

Figure 7.12: *Adapting the parameters of the model potential. Solid: experiment for $V_g = -1.50V$, dashed: semiclassics for $s_c = 1.5$, $s_d = 1.5$, and $s_0 = 0.05375\mu m$.*

The following calculations return to the parameters of the quantum approach in order to have the two theoretical methods on the same basis.

[10]Note that the amplitudes are, as usual in semiclassical calculations, adapted.

7.5.3 The maximum spacing

Fig. 7.13 compares the variation of the maximum spacings of the semiclassical description (heavy lines and filled symbols) to the experimental data[11] (thin lines and open symbols). For large (a) as well as for intermediate antidot diameter (b) the average spacing of the maxima is nearly constant in B, only slightly decreasing for stronger fields. This is clearly reproduced by the semiclassical approach. The mean spacing is – both experimentally and in the semiclassical description – unaffected by changes of the antidot diameter. The maxima spacings, however, do not vary smoothly, but show random-like variations for small changes in either B or s_d. Large antidots (Fig. 7.13(a)) give rise to a more regular pattern than smaller antidot diameters (Fig. 7.13(b)). The amount of variation is correctly reproduced by the semiclassical description. The quantum calculation in Fig. 7.3(b) shows less agreement with the experimental data. This is again due to the shift of the quantum G_{xx} to larger magnetic fields, which was already observed in Sec. 7.3.2.

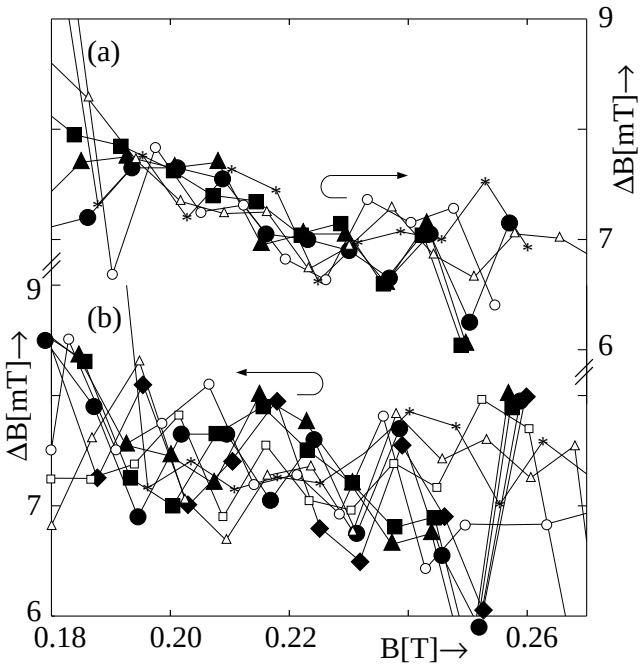

Figure 7.13: *The spacing of the maxima in dependence of B. Thin lines, open symbols: experiment. Heavy lines, filled symbols: semiclassics. (a) Large antidot diameters. Experiment: $V_g = -1.42 \ldots -1.5$ V, semiclassics: $s_d = 2.05 \ldots 2.07$. (b) Medium antidot diameters. Experiment: $V_g = -1.3 \ldots -1.36$ V, semiclassics: $s_d = 1.88 \ldots 1.92$.*

The good agreement of the semiclassical prediction of the maximum spacings with the experimental findings is surprising, since the contributions of the individual orbits show a different behavior. This is illustrated in Fig. 7.14. All individual orbits (thin lines) show a strong decrease of ΔB with stronger fields. This does not agree with the experimental findings for the spacing (heavy lines and symbols). This observation was one of the arguments of Ref. [48], leading to the conclusion that the magnetoconductance of the channel is not accessible to semiclassical approximations. The solution to this apparent contradiction is that in the present system not a few orbits dominate the quantum oscillations, but many of them contribute with comparable amplitudes, actions

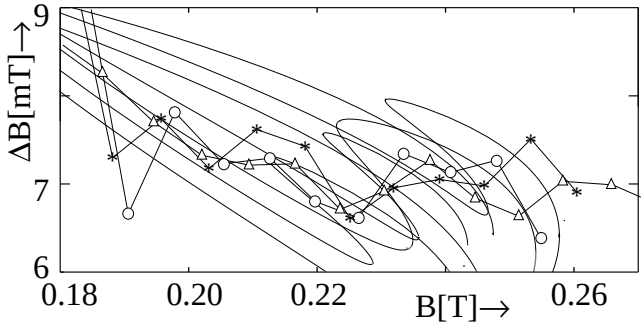

Figure 7.14: *Thick lines and symbols: Experimental maxima spacings as in Fig. 7.13(a). Thin lines: Maxima spacings from the contributions of some individual orbits for $S_d = 2.06$.*

[11] The maxima positions were determined from the experimental δB. A cubic spline fit was used to interpolate between the measured points. The latter were taken each 0.5 mT.

and periods. Varying the magnetic field, the individual orbits change their ΔB. Simultaneously, the orbit stabilities (and thus the relative amplitudes) are affected. In combination, the two effects lead to the weak variation of ΔB plotted in Fig. 7.13.

The semiclassical analysis is, as depicted in Fig. 7.13, also able to reproduce the amount of short-range variation of the maximum spacings. This shows that the effect is not due to experimental noise, but reflects the physical properties of the system. The basic mechanism can easily be understood within the semiclassical picture. As pointed out above, the influence of the individual orbits varies strongly with both magnetic field and antidot diameter. Small changes in these parameters therefore can lead to significant shifts of the maxima positions. The more the orbits differ geometrically, the larger are the changes in δB induced by tiny changes of the parameters. For larger antidot diameter, i. e. narrow constrictions, the classical orbits get more and more similar to each other. This nicely explains the increased short-range variations of δB for smaller antidots.

Both the sinusoidal form of the experimental δG_{xx} and the Fourier analysis were consistent with the picture that just a few orbits contribute significantly to the trace sum. The analysis of the maxima spacings, however, shows that the idea to trace down the magnetoconductance features to the properties of one or two single orbits must be rejected. The observed behavior depends on the subtle interplay between changes in the classical stabilities and in the actions of a large number of similar orbits.

7.5.4 Variation of the antidot diameter

The second question formulated in Sec. 7.3.1 concerns the dislocations which occur in the positions of the conductance maxima when varying the antidot diameter. Fig. 7.15(a) shows the predictions of the semiclassical approach. The points represent the calculated maxima positions, the thin lines are just a guide for the eye. The semiclassical description clearly reproduces the dislocations (small boxes). This shows that the dislocations are no genuine quantum effect, but accessible by semiclassic methods.

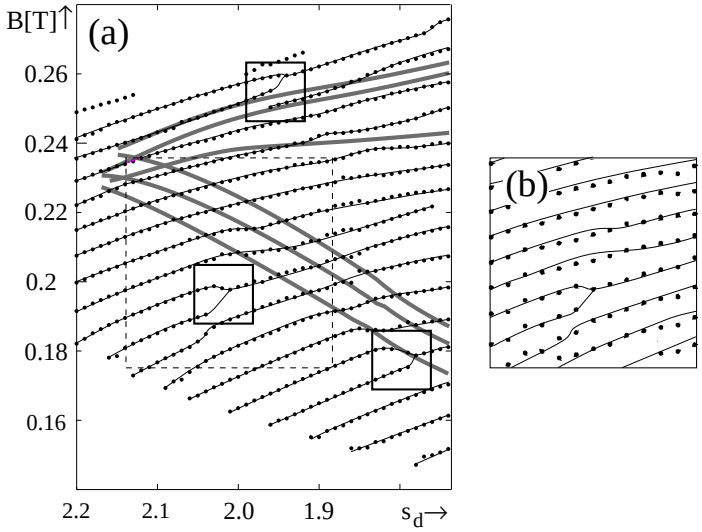

Figure 7.15: *(a) Result of the semiclassical analysis for the positions of the conductance maxima with varying magnetic field B and antidot diameter s_d (dots). Thin lines connecting the points are just to guide the eye. The corresponding experimental data is shown in Fig. 7.2. The gray-shaded lines correspond to loci of orbit bifurcations (see Sec. 7.6, p. 86). (b) Local behavior around a dislocation. Lines: semiclassical result of the dashed box in (a), points: experimental data around the dislocation marked with the dashed box in Fig. 7.2.*

Fig. 7.15(b) illustrates the local behavior around a dislocation. The lines correspond to the semiclassical result (dashed box in Fig. 7.2(a)), the points give the experimental data of Fig. 7.2(d). The values of B and s_d have been shifted slightly, but no rescaling was used. The excellent agreement shows that the local behavior at a bifurcation is not only qualitatively, but even quantitatively explained within the the semiclassical description.

7.6 Semiclassical interpretation

The last section confirmed that the semiclassical approach is able to explain all observed magnetoconductance features of the channel with central antidots. The semiclassical technique has two main advantages compared to quantum calculations. The first benefit, the reduced numerical effort, has already been exploited above. It was therefore possible to calculate the data on a fine grid, and even to adapt the system parameters. Such a task is in principle not impossible in a quantum approach, but frequently the numerical effort is prohibitive.

The second advantage of semiclassical descriptions is that they express quantum oscillations in terms of classical quantities. Since human intuition is strongly based on classical physics, the insight gained in the nature of these interference effects is enlarged by a semiclassical description. The resulting intuitive picture might also be helpful for the development of new devices, serving as a guiding line how to design a sample to achieve certain desired properties. This section exploits the close relation of the trace formula to the classical dynamics of the system to give an intuitive picture of the origin of the maxima dislocations.

The different periodic orbits of the system have different degrees of similarity. A reasonable way of splitting them in groups is to consider always those orbits together which are closely related, i. e., have bifurcations with each other in the parameter range observed. These orbit groups will be called *families*[12]. Fig. 7.6 shows the traces of the orbits belonging to such a family, illustrating their close internal relation.

To understand the nature of the effect leading to the dislocations, a model system with only the orbits of this family will be considered for the moment. In Fig. 7.16(c) the squares give the positions of the conductance maxima for this model system. This reduced system already shows all the characteristic features observed in the experiment (see Fig. 7.2). It especially exhibits the dislocations of the conductance maxima (boxes) which are so far reproduced, but unexplained. As illustrated in Fig. 7.6, the members of the family can be divided into three generations, depending on whether an orbit is offspring of the orbit 1, 2 or 3. These are, for obvious reasons, called grandparents, parents, and children generation. All members within a generation behave nearly identical, thus justifying the classification. In Fig. 7.16(a) and (b) the maxima of the contributions of the grandparent and the children generation to the conductance is shown. All generations[13] induce nearly equidistant maxima in B with a constant shift to larger B if the antidot diameter is reduced. This in complete agreement with the simple Aharonov-Bohm picture discussed in Sec. 7.3.1. The behavior of the individual generations is therefore readily interpreted in terms of their geometrical properties. This implies, that the contributions of the individual generation do not show dislocations. These must be due to the interplay of the different generations.

The children have a larger semiclassical amplitude than the grandparents. Therefore the maxima of the total G_{xx} (i. e. including all generations) follow the childrens' maxima where the latter exist. Otherwise, the maximum positions of the complete family agree with those of the grandparents. This is confirmed by Fig. 7.16(d). The parents' influence

[12] These families are not to be confused with the families of degenerate orbits occurring in systems with continuous symmetries.

[13] This holds also for the parents generation. It is is not shown separately, since its contribution is negligible throughout.

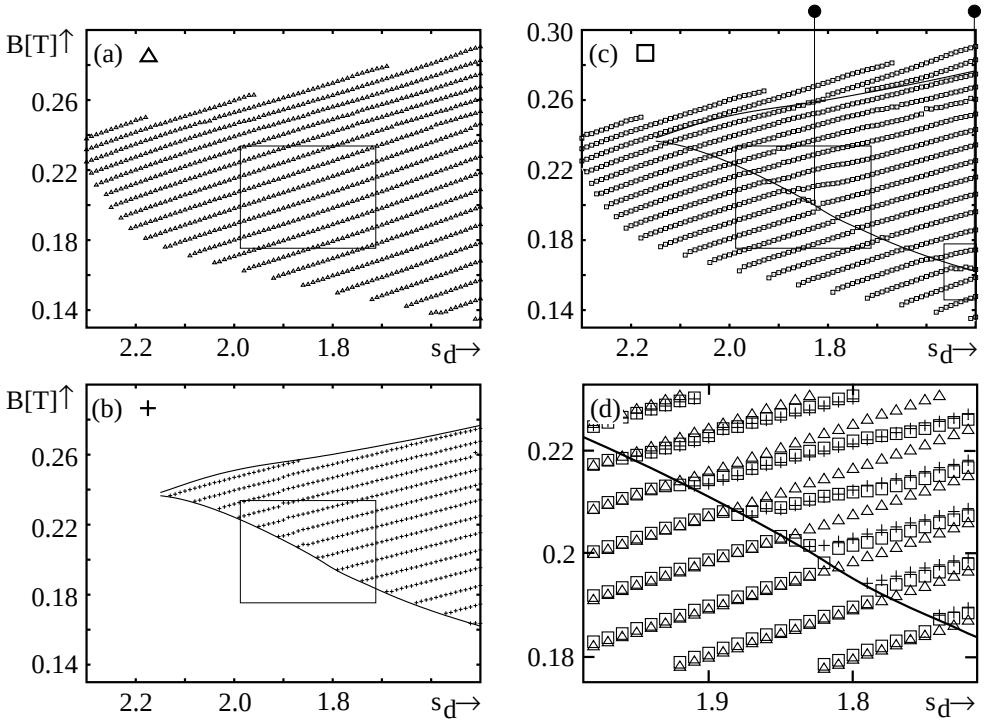

Figure 7.16: *The positions of the conductance maxima due to different orbit generations of the family shown in Fig. 7.6: (a) grandparents, (b) children, (c) all generations. The parents' contribution is not shown separately, since it is negligible. (d) Blow-up from (a)-(c). The maxima of the total δG_{xx} (squares) follow the maxima of the children (crosses) where these exist, and those of the grandparents (triangles) otherwise. Heavy lines indicate the loci of bifurcations in the (s_d, B) plane.*

was found to be negligible throughout. The geometric differences between grandparents and children orbits lead to different dependencies on the antidot diameter and the magnetic field strengths. Therefore the generations show different maxima spacings as well as different slopes of the maxima with varying s_d. Neither the slopes nor the spacings match along the generation boundaries. This is similar to growing two materials with different lattice constants onto each other. The resulting lattice defects are the equivalent of the dislocations observed.

From this interpretation, further predictions can be deduced: (*i*) Scaling the system does not affect the classical dynamics, so that the dislocations move along the (universal) bifurcation lines. (*ii*) Assuming a linear dependence of the action difference ΔS between children and grandparents on s_d, the dislocations are equally spaced in s_d. (*iii*) Scaling S with a factor κ,[14] the distances between dislocations scale according to $\Delta s_d \propto \kappa$. These predictions are checked in Fig. 7.17, where the maxima positions of the system of Fig. 7.16(d), scaled with a factor of 2 (a) and 3 (b), are shown. The dislocations move indeed on the bifurcation line. They occur approximately at the predicted values of s_d, which are marked by pins.

In the full calculation with over 60 orbits, the various families with their bifurcation structures (gray lines in Fig. 7.15(c)) are superimposed. Only those dislocations survive for which the above model scenario is locally dominating and no further orbits interfere. As a result, some of the dislocations disappear, some are slightly shifted in the (s_d, B)

[14] This corresponds to scaling the size with κ and the magnetic field with κ^{-1}.

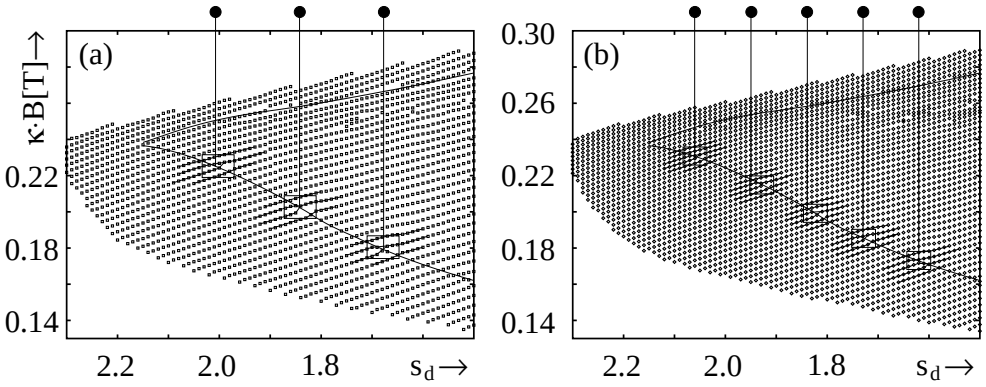

Figure 7.17: *The system of Fig. 7.16(d), scaled by a factor of $\kappa = 2$ (a) and $\kappa = 3$ (b). The thin lines are guide to the eye. The magnetic field is scaled with κ to simplify the comparison with Fig. 7.16. The bifurcation lines (and thus the region where the children exits) are indicated by thick lines. Dislocations are marked with boxes. The pins correspond to the prediction of the location of the dislocations given in the main text.*

plane. Therefore, no unique one-to-one relation between dislocations and bifurcations can be established. Nevertheless, the qualitative pattern remains the same.

This interpretation suggests that there are two orbit groups with different behaviors present, their interplay being responsible for the dislocations of the maxima positions observed. This is in complete agreement with the Fourier analysis of the experimental data shown in Fig. 7.10, which shows two distinct peaks. The Fourier transform of the semiclassical data for the individual orbits generations is given in Fig. 7.18. For large antidot diameter the parents (dashed) have dominant Fourier components, as they exist in a much larger region in B compared to the children (solid). For smaller antidots, the region where children orbits exist rapidly grows, and due to their large semiclassical amplitude they soon dominate the Fourier spectrum. In the intermediate regime, two separate peaks can be observed. This is the same behavior found in the Fourier analysis of the experimental data in Fig. 7.10, where a peak at $\delta B \approx 7$mT vanished for smaller antidots, and a new peak occurred. The Fourier analysis of the experimental data therefore supports the interpretation that the observed structure in the maxima positions of the conductance is due to the interplay between two orbit generations.

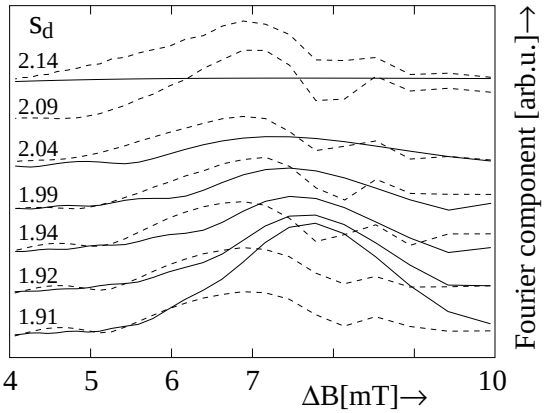

Figure 7.18: *The Fourier transform of the contributions of the individual orbit families. Solid: children, dashed: parents.*

7.7 Summary

In summary, the semiclassical description successfully reproduces all experimentally observed features of the magnetoconductance of a mesoscopic channel with antidots. It was additionally demonstrated that the low numerical demands of the semiclassical approximation make a fit of the experimental potential possible.

The variations in the maxima spacings could by reproduced in every respect. The semiclassical approach yields the correct value for ΔB, together with the average behavior with varying field and antidot diameter. Furthermore, the predictions of the amount of short-range variation of ΔB in dependence of B and s_d agree with the experimental findings. The semiclassical picture confirms that these variations are not due to experimental inaccuracies, but reflect system properties.

The dislocations of the conductance maxima as functions of magnetic field B and antidot diameter s_d have been shown to be related to bifurcations of the leading classical periodic orbits of the system. The dislocations are due to the fact that the bifurcations define the border lines between regimes of different predominant orbit generations, leading to different dependences of the conductance maxima on B and s_d. This induces the observed dislocations of the maximum positions, analogously to lattice defects at interfaces. As the classical dynamics are not affected by a rescaling of the system, the scaling behavior of the dislocations can be easily understood in the semiclassical approach.

These results disprove previous arguments claiming the channel system exhibits inherent quantum features. These arguments were based on the discussion of the semiclassical contributions of *individual* orbits. The semiclassical picture proposed here, in contrast, claims that the subtle interplay between many different orbits, i.e. the variations in all their stabilities and actions under the change of the system parameters, is responsible for the observed magnetoconductance features.

The way how bifurcations affect the quantum oscillations in the channel system is different from previously reported mechanisms. Using a numerical version of uniform approximations, the bifurcations of the system were shown to have no locally enhanced influence on the conductance. In super-deformed nuclei [10] or elliptic billiards [57], in contrast, period doubling orbit bifurcations influence the quantum shell structure due to their dominant order in $1/\hbar$. The influence of the bifurcations in the present system is also different from the one reported for the resonant tunneling diode [114]. There, the bifurcations lead to a doubling of the period, whereas in the system considered here the periods of all relevant orbits are approximately constant. Furthermore, in the resonant tunneling diode only a few orbits were found to be important, whereas the present system is dominated by a much larger number of orbits with nearly identical actions, periods and amplitudes.

Chapter 8

Conclusion

This work investigated the applicability of semiclassical approximations to mesoscopic systems. The different problems analyzed are grouped around three setups: two simple model systems and a more complicated structure realized in experiment. The theoretical studies, namely the calculation of the level density of the disk billiard and the conductivity tensor of the free 2DEG, analyzed the influence of various higher-order $\hbar$ contributions to the semiclassical description. It was shown that only a few of these corrections are relevant. The magnetoconductance of the experimental system – a mesoscopic channel with antidots – was successfully described within leading order of $\hbar$. All observed features were quantitatively and qualitatively reproduced, and an intuitive picture of their origin could be given.

Contents

Working on semiclassical techniques, i. e. approximations of the quantum mechanical formalism to leading order in $\hbar$, can have different foci. The interest can be directed towards the correct description of the properties of a specific system. This includes all questions relevant for (experimental) applications. Another motivation is to gain increased theoretical insight in semiclassical techniques. In this context, the limits of such an approximation are considered and formal problems of the approach are solved.

For the present work, these two aspects have been equally important. This conclusion will therefore summarize the main results twice. First, an overview of the findings for the specific systems is given (Sec. 8.1), before the results are collected according to theoretical criteria (Sec. 8.2 and 8.3). The dissertation closes with suggestions for further investigations.

8.1 The systems investigated

The semiclassical approximation was shown to be a well-adapted tool for all the mesoscopic systems considered. The approach was seen to be sufficiently accurate. Compared to the quantum mechanical calculations, the numerical effort is significantly reduced.
The semiclassical trace formula only depends of the properties of the classical dynamics of the system. This feature allows to give simple, intuitive pictures for the relevant processes. A particular focus was directed towards the explanation of the observed quantum interference effects in these classical terms.

8.1.1 The disk billiard

The level density of the disk billiard in homogeneous magnetic field was chosen as the first model system. It is simple enough to allow an analytic quantum mechanical solution, so that the shortcomings of the semiclassical approximation can be analyzed very accurately. It is, on the other hand, complex enough to exhibit the typical problems semiclassical approximations face. In varying magnetic fields, orbit bifurcations occur. Additionally, the system comprises orbits with symmetries of different dimensionality, so that different powers in $\hbar$ contribute to the trace sum. Finally, grazing or diffractive effects come into play. A detailed analysis resulted in a surprisingly small influence of most of these $\hbar$ corrections. The only relevant correction concerns the Maslov index. Using a simple one-dimensional approximation, it was replaced by a reflection phase. With this modification, the semiclassical trace formula gives excellent results for arbitrary field strengths, both for the shell structure and for full quantization. The shell structure could be explained within a simple picture including only the classical properties of three periodic orbits.

8.1.2 The free 2DEG

The free 2DEG was selected as a simple model system for the application of semiclassical transport theory. Both its longitudinal and its Hall conductivity were described semiclassically. It was shown that the Shubnikov-de-Haas oscillations in the longitudinal conductivity are an effect of leading order in $\hbar$. The integer quantum hall effect, in contrast, is almost exclusively due to a single contribution of *second* leading order, namely the period dependence of the cyclotron orbits on the magnetic field strength. The corresponding $\hbar$ correction could be derived for arbitrary systems.

8.1.3 The channel with antidots

The longitudinal magnetoconductance of a narrow channel with central antidots was chosen deliberately as a difficult problem for a semiclassical analysis. Previous results had found strong indications that the effects observed in this system, namely the dependence of the maxima spacings on the magnetic field and the dislocations observed when varying the antidot diameter, are genuine quantum effects, not accessible to a semiclassical calculation. Furthermore, the system shows features that disfavor a semiclassical description: The channel has many orbits with comparable length and action. They are related by a complicated structure of bifurcations, and ghost orbits are ubiquitous. Despite these problems and the related technical difficulties it was possible to give a complete semiclassical description of all observed effects. The local behavior at a dislocation could even be reproduced quantitatively, and the parameters of the model potential could be fit to the experimental situation. It was shown that the complex behavior of the system is not due to higher-order contributions in $\hbar$, but to a delicate interplay between the actions and amplitudes of many similar orbits. Within the semiclassical picture, the observed magnetoconductance features could be related to bifurcations in the leading classes of periodic orbits.

8.2 The relevance of $\hbar$ corrections

A central result of this work is that semiclassical approximations are valid in a much wider range than they are expected to. Even large individual higher-order contributions frequently lead to marginal corrections, since they average out to a great extent. Only two important sources of $\hbar$ corrections were identified.

8.2.1 Different powers in $\hbar$ in the trace formula

The first group of relevant $\hbar$ corrections are those that come naturally into play by the application of the semiclassical procedure itself. This happens for example in systems that include orbits symmetries with different dimensionality. The orbits with lower symmetry lead to contributions in higher than leading order in $\hbar$. These $\hbar$ corrections are neglected in the standard approach. For the disk billiard, however, the inclusion of the lower-symmetry bouncing orbits was shown to be necessary.[1]

The conductivity tensor is another property where the semiclassical approximation by itself includes higher-order terms in $\hbar$. In this case the leading-order term of the level density shows up as an $\hbar$ correction in the Hall conductivity. This correction is responsible for the plateaus in the hall voltage, i. e. the integer quantum hall effect. The corresponding formula for general systems could be derived.

8.2.2 Reflection phases

The Maslov index was identified as another source of potentially important $\hbar$ corrections. This additional phase occurs at classical turning points (or their higher-dimensional equivalents). It exhibits a spurious discontinuity in dependence of the steepness of the

[1] Similar results have been obtained for other systems as well [119].

effective potential. In a one-dimensional approximation this jump can be removed by replacing the Maslov index by a reflection phase. The phase depends explicitly on $\hbar$, which corresponds to $\hbar$ corrections to the trace formula. These corrections were shown to be important for the disk billiard in the strong field regime $R_c \lesssim R$. They correct the degeneracy of the Landau levels, which is overestimated by the standard approach. The mechanism can be interpreted as a proximity effect of the boundary.[2]

The generalization of the reflection phase to higher dimensions is still an open problem.

8.2.3 Bifurcations and grazing

Grazing corrections are related to finite integration limits in stationary-phase approximations. These effects can be expected to give corrections up to 50% to the level density of the disk billiard. A detailed analysis showed, however, that this correction is negligible there.

Bifurcations were seen to be important for problems including only a few orbits. This is intuitive, since bifurcations lead to divergencies in the standard Gutzwiller approach. If many orbits are included, the influence of the bifurcations (although their number might drastically increase) gets smaller. This has to be interpreted as a cancellation effect. This behavior was found for both the disk billiard and the channel system.

There are different mechanism relating bifurcations to experimentally observable effects. It was reported that their lower order in $\hbar$ may lead to local dominance of the bifurcations. Period doubling bifurcations are known to be responsible for period-doubling effects in resonant tunneling diodes. The mechanism in the channel was shown to be different. There, bifurcations mark the boundaries of phase space regions with different classical dynamics. The semiclassical description reflects the classical phase space structure in the quantum oscillation. Like that is was possible to directly relate one type of bifurcations of the cannel system to the dislocations observed in the maxima positions of the magnetoconductance.

8.3 Smoothing in higher order of $\hbar$

Finite temperature and impurity scattering lead to finite line widths and characteristic line shapes. Just as the semiclassical approximation itself, the implementation of those effects in the trace formula is only valid up to leading order in $\hbar$. This work presented generalizations applicable to the $\hbar$ corrections considered.

For both cases where this modified smoothing scheme was applied, namely the bifurcations and the grazing correction in the disk billiard, the magnitude of the smoothing correction was comparable to the $\hbar$ correction itself. For bifurcations in systems with many orbits it was shown that neglecting the $\hbar$ correction in the trace formula and just including the correct (numerical) smoothing already leads to surprisingly good results.

[2] Reflection phases can also be applied to problems including partial transmission and reflection, and therefore also to tunneling.

8.4 Suggestions for further investigations

The results of this work indicate that bifurcations have a considerable influence in systems with only a few dominating orbits. For those, a numerical inclusion of bifurcations of codimension 2 along the path presented here could be useful. A suitable prototype for these systems is the Hénon-Heiles potential, where three important orbits are involved in a period-tripling and subsequent tangent bifurcation. An appropriate starting point are the uniform formulas presented by Schomerus [71], with an adaption to the numerical limitations following appendix B.

For the disk billiard in strong magnetic fields, the correction of the Maslov index was shown to be important. This correction was included using a simple, one dimensional approximation, where the potential at the classical turning point was expanded to linear order. This approximation could be further improved implementing the analytical reflection phases worked out by Friedrich *et al.* [29]. This would be another step towards a generalization of the Maslov index.

The most rewarding field for future investigations, however, is the application of the semiclassical techniques to experiment. The fit of the model potential of the channel system was so successful, that a project to determine the experimental potential by semiclassical techniques seems reasonable. Such a project would exploit the substantially reduced numerical effort of semiclassical calculations, making an adaption of many parameters of the experimental potential numerically feasible. A good candidate for such an investigation is the conductance of the Aharonov-Bohm-ring measured by Pedersen *et al.* [124]. The long-range oscillations superimposed on the AB frequency stem from the interference of trapped orbits in the ring arms. Fitting the semiclassical findings to the experimental observations should, among other predictions, allow an estimate of the depletion width of the etch border.

Similar calculations should be possible for antidot superlattices. For the system with large antidot diameter presented by Eroms *et al.* [27], also the steepness of the effective potential could be accessible.

These investigations would add a new quality to semiclassical approximations. The semiclassical description would then not only reproduce the experimental findings and allow their interpretation in an intuitive picture. For these systems, it could additionally provide a tool to determine experimental parameters hardly accessible by other means.

Appendix A

Numerical evaluation of periodic orbits

This technical appendix describes numerical techniques to deal with classical periodic orbits. Efficient methods for finding those orbits, calculating the relevant properties for the trace formula, and following them through parameter space are presented.

Contents

A.1 Finding periodic orbits

The numerical determination of periodic orbits in an arbitrary potential includes three steps:

1. Integration of the classical equations of motion (EOM).
2. Calculation of the variation of the endpoint for small changes of the starting point.
3. Calculating an improved starting point.

Beginning with randomly distributed starting points, these steps are iterate until convergence.

A.1.1 Integrating the equations of motion

The equations of motion are readily integrated numerically. For a sufficient performance of this innermost step in the semiclassical calculation an efficient scheme with adaptive step-size control should be implemented. For smooth potentials, the algorithm presented by Bulirsch and Stoer [104, 107] is accepted to be one of the most powerful methods available.

A.1.2 The matrizant

Calculating the effect of a small change of the starting point by integrating trajectories at small, but finite distances suffers from severe numerical limitations. The numerical roundoff gets worse for larger $|\mathrm{Tr}(\widetilde{M})|$ and is intolerable already for moderately unstable orbits. Eckhardt and Wintgen [25] presented a method which is better adapted to the limitations of a numerical approach. It will be outlined in the following.

Denoting the phase space vector of the reference trajectory with $\boldsymbol{\gamma} = (\boldsymbol{q}, \boldsymbol{p})$ with the coordinates $\boldsymbol{q}$ and the canonical conjugate momenta $\boldsymbol{p}$, the EOM can be written as

$$\dot{\boldsymbol{\gamma}} = \underline{J}\,\frac{\partial H}{\partial \gamma} \quad \text{with} \quad \underline{J} := \begin{pmatrix} 0 & \mathbb{1} \\ -\mathbb{1} & 0 \end{pmatrix} . \tag{A.1}$$

Here and in the following, the dots signify derivatives with respect to time. The linearized time evolution of the difference vector to the reference orbit $\delta\boldsymbol{\gamma}$ is given by

$$\delta\boldsymbol{\gamma}(t) \;=\; \underline{\chi}(t)\,\delta\boldsymbol{\gamma}(0)\;, \tag{A.2}$$

with the *matrizant* $\underline{\chi}$. The time evolution of $\underline{\chi}$ can be shown to be

$$\dot{\underline{\chi}} \;=\; L\cdot\underline{\chi} \quad \text{with} \quad \underline{L}(t) \;=\; \underline{J}\;\left.\frac{\partial^2 H}{\partial \boldsymbol{\gamma}^2}\right|_{\boldsymbol{\gamma}(t)}\;, \tag{A.3}$$

and $\underline{\chi}(0) = \mathbb{1}$. For periodic orbits, the *monodromy matrix*[1] M is defined as $M = \underline{\chi}(T)$, where T is the period of the orbit.

[1] To be consistent with the standard notation in trace formulae, the monodromy matrix is denoted without underscore.

The matrizant is symplectic, i. e. $\underline{\chi}^\dagger \underline{J}\,\underline{\chi} = \underline{J}$, and two eigenvalues of $\underline{\chi}$ are equal to 1 (see Eq. (A.5) below). One of these trivial eigenvalues is associated with energy conservation, the other with the displacement along the trajectory. The corresponding eigenvectors can be eliminated analytically. This will be sketched in the following for two dimensional systems. From now on, $\boldsymbol{\gamma} = (x, y, u, v)$.

Introducing a local coordinate system by the unitary transformation $\underline{U}(t)$ according to

$$\delta\widehat{\boldsymbol{\gamma}} = \underline{U}(t)\,\delta\boldsymbol{\gamma} \quad \text{with} \quad \underline{U}(t) = \begin{pmatrix} \dot{x} & -\dot{u}/q^2 & -\dot{y} & -\dot{v}/q^2 \\ \dot{y} & -\dot{v}/q^2 & \dot{x} & \dot{u}/q^2 \\ \dot{u} & \dot{x}/q^2 & \dot{v} & -\dot{y}/q^2 \\ \dot{v} & \dot{y}/q^2 & -\dot{u} & \dot{x}/q^2 \end{pmatrix}, \tag{A.4}$$

where $q = |\dot{\boldsymbol{\gamma}}|$ leads to a transformed matrizant

$$\delta\widehat{\boldsymbol{\gamma}}(t) = \underline{\widehat{\chi}}(t)\,\delta\widehat{\boldsymbol{\gamma}}(0) \quad \text{with} \quad \underline{\widehat{\chi}}(t) = \underline{U}^{-1}(t)\,\underline{\chi}(t)\,\underline{U}(0) = \begin{pmatrix} 1 & * & * & * \\ 0 & 1 & 0 & 0 \\ 0 & * & & \\ 0 & * & \multicolumn{2}{c}{\underline{\widetilde{\chi}}(t)} \end{pmatrix}. \tag{A.5}$$

In this coordinate system the two eigenvalues of 1 can be seen explicitly. The time evolution of the reduced matrizant $\underline{\widetilde{\chi}}(t)$ is given by

$$\dot{\underline{\widetilde{\chi}}}(t) = \underline{l}(t)\,\underline{\widetilde{\chi}}(t) \quad \text{with} \quad \underline{l} = \underline{U}^{-1}(\underline{L}\,\underline{U} - \dot{\underline{U}})\,. \tag{A.6}$$

Denoting the partial derivatives of the Hamiltonian by subscripts, i. e. $H_x = \partial H/\partial x$, the matrix $\underline{l}$ is explicitly given by

$$\begin{aligned} \underline{l} &= \begin{pmatrix} l_{11} & l_{12} \\ l_{21} & l_{22} \end{pmatrix}, \quad \text{with} \qquad (A.7) \\ l_{11} &= \big[(-H_{xx} - H_{yy} + H_{uu} + H_{vv})(H_x H_u + H_y H_v) \\ &\quad +(-H_x^2 + H_y^2 + H_u^2 - H_v^2)(H_{yv} + H_{xu}) + 2(H_x H_y - H_u H_v)(H_{xv} + H_{yu})\big]/q^2 \\ l_{12} &= \big[(H_{xx} + H_{vv})(H_y^2 + H_u^2) + (H_{yy} + H_{uu})(H_x^2 + H_v^2) \\ &\quad -2(H_x H_u + H_y H_v)(H_{xu} + H_{yv}) - 2(H_x H_y - H_u H_v)(H_{xy} - H_{uv})\big]/q^4 \\ l_{21} &= \big[-(H_{xx} + H_{yy})(H_u^2 + H_v^2) - (H_{uu} + H_{vv})(H_x^2 + H_y^2) \\ &\quad +2(H_x H_v + H_y H_u)(H_{xv} + H_{yu}) + 2(H_x H_u - H_y H_v)(H_{xu} - H_{yv})\big] \\ l_{22} &= -l_{11}\,. \end{aligned}$$

These formulae have been derived by Eckhardt and Wintgen [25]. They shall now be applied to a particle in a homogeneous magnetic field and a velocity-independent external potential V. For this situation, it is convenient to express $\underline{l}$ in dependence of the real space coordinates and their time derivatives. This finally leads to

$$\begin{aligned} l_{11} &= \left(2 - w_c^2/2 - V_{xx} - V_{yy}\right)(\dot{x}V_x + \dot{y}V_y)/q^2 \qquad (A.8) \\ l_{12} &= \left(1 + (w_c/2)^2\right)/q^2 + \left[V_{xx}(\dot{x}^2 + \beta^2) + V_{yy}(\dot{y}^2 + \alpha^2) + 2V_{xy}(\dot{x}\dot{y} - \alpha\beta)\right]/q^4 \\ l_{21} &= -\left(V_{xx} + V_{yy} + w_c^2/2\right)\left(\dot{x}^2 + \dot{y}^2\right) - 2\left(\alpha^2 + \beta^2\right) \\ l_{22} &= -l_{11}\,. \end{aligned}$$

with $w_c = eB/m^\star$, $\alpha = (V_x - \dot{y}w_c/2)$ and $\beta = (V_y + \dot{x}w_c/2)$. Starting from the initial condition $\underline{\widetilde{\chi}}(0) = \mathbb{1}$, Eq. (A.6) can be integrated. The most effective approach is to solve the equations of motion for $\underline{\widetilde{\chi}}$ and the time evolution of the trajectory simultaneously. This leads to four equations for the phase-space motion and another four for $\underline{\widetilde{\chi}}$. Without reduction of the matrizant to two dimensions, a $(4 \times 4 + 4 =)$ 20-dimensional differential equation has to be solved. This integration is the innermost loop of the calculation, so that the analytical reduction of the monodromy matrix speeds up the the semiclassical approximation by a factor of about 2.

The matrizant gives the linearization of *arbitrary* deviations from $\boldsymbol{\gamma}(t)$. In the following section this information will be used in a numerical scheme to converge to periodic orbits.

A.1.3 Improving the initial condition

To identify an orbit with a unique starting point, an additional plane in phase space, the *Poincaré surface of section* $\mathcal{P}$, has to be defined. Starting with a random initial condition on $\mathcal{P}$, the trajectory and the reduced matrizant can be integrated as explained in the previous section. Having found another intersection with $\mathcal{P}$ close to the starting point, the reduced matrizant should be used to improve the initial condition.

For a simple notation, $\boldsymbol{\gamma}$ is the phase space vector (x, y, u, v) as given above, and the initial and final point are denoted by $\boldsymbol{\gamma}_i$ and $\boldsymbol{\gamma}_f$, respectively. The corresponding vectors in the local coordinate system are given by $\widehat{\boldsymbol{\gamma}}_i = \underline{U}^{-1}(0)\,\boldsymbol{\gamma}_i$ and $\widehat{\boldsymbol{\gamma}}_f = \underline{U}^{-1}(T)\,\boldsymbol{\gamma}_f$.[2] The second part of $\widehat{\boldsymbol{\gamma}} = (\widehat{\gamma}_1, \widehat{\gamma}_2, \widehat{\gamma}_3, \widehat{\gamma}_4)$, is denoted by $\widetilde{\boldsymbol{\gamma}} := (\widehat{\gamma}_3, \widehat{\gamma}_4)$. Starting at a distance $\delta\widetilde{\boldsymbol{\gamma}}$ to the initial point results, according to the definition of $\underline{\widetilde{\chi}}$ in Eq. (A.5), in a deviation $\Delta\widetilde{\boldsymbol{\gamma}} = \underline{\widetilde{\chi}}\,\delta\widetilde{\boldsymbol{\gamma}}$ from the final point. If the new starting point corresponds to a periodic orbit, i. e.

$$\begin{aligned} \widetilde{\boldsymbol{\gamma}}_i + \delta\widetilde{\boldsymbol{\gamma}} &\stackrel{!}{=} \widetilde{\boldsymbol{\gamma}}_f + \Delta\widetilde{\boldsymbol{\gamma}} \\ \Rightarrow \quad \delta\widetilde{\boldsymbol{\gamma}} &= (\mathbb{1} - \underline{\widetilde{\chi}})^{-1}\,(\widetilde{\boldsymbol{\gamma}}_f - \widetilde{\boldsymbol{\gamma}}_i)\,. \end{aligned} \tag{A.9}$$

All quantities on the r.h.s. of Eq. (A.9) are known explicitly, so that the necessary correction $\delta\widetilde{\boldsymbol{\gamma}} = (\widetilde{\gamma}_3, \widetilde{\gamma}_4)$ leading to a periodic can be calculated. Note that by the reduction to 2D no information is lost, since the two omitted basisvectors have eigenvalues 1. The correction $\delta\widetilde{\boldsymbol{\gamma}}$ can now be transformed back to the ordinary phase space coordinates via $\delta\boldsymbol{\gamma} = U(0)\,\delta\widehat{\boldsymbol{\gamma}}$, where $\delta\widehat{\boldsymbol{\gamma}} := (0, 0, \widetilde{\gamma}_3, \widetilde{\gamma}_4)$. This step introduces an additional error, since the local coordinate system of neither the initial point $U(0)$, nor of the final point $U(T)$ but of the *new* starting point gives the correct transformation. In practice, however, the difference is insignificant.[3] Apart from that small error, $\delta\widehat{\boldsymbol{\gamma}}$ is equivalent to the result of a calculation using the full 4D matrizant.

Taking $\boldsymbol{\gamma} = \boldsymbol{\gamma}_i + \delta\boldsymbol{\gamma}$ as the new starting point unfortunately

1. leaves the Poincaré surface of section.
   This is associated with the fact that the periodic orbit may have another period as the reference orbit. The initial correction therefore has to be extrapolated onto the Poincaré surface according to $\delta\widehat{\boldsymbol{\gamma}} + \delta t \cdot \dot{\boldsymbol{\gamma}} \in \mathcal{P}$.

[2] Please note that for non-closed orbits the local coordinate system for initial and final point are different.

[3] The best approximation feasible at this stage is a linear interpolation between the local coordinate systems. This does not improve the convergence.

2. violates energy conservation.
   The matrizant describes the linearization of deviations from the reference orbit, and thus is only energy conserving to linear order. To prevent a shift of energy, the starting condition has to be projected back on the energy surface.[4]

Including these two projection procedures, $\boldsymbol{\gamma} = \boldsymbol{\gamma}_i + \delta\boldsymbol{\gamma}_{\text{projected}}$ gives an improved initial condition.

A.1.4 Converging to a periodic orbit

In the linear regime of a periodic orbit, the scheme of the preceding section converges in a single step. If the initial condition is outside the linear regime, the procedure has to be iterated. Usually a few iteration steps (< 10) are sufficient to determine the initial condition within machine accuracy (i. e. $\approx 10^{-13}$). In closed systems nearly all starting conditions converge to a periodic orbit, so that periodic orbits are easily found. For open systems the trajectories have a finite probability to leave the system. This leads to an increased numerical effort, since several starts are needed to converge to a periodic orbit. For the channel the probability for a trajectory to leave the central antidot regime is so large that only a small fraction of initial conditions converges.

To converge to those unstable fixpoints whose incoming and outgoing manifold intersect on the Poincaré surface of section at an extremely small angle, it is sometimes useful to add only a fraction $0 < \kappa < 1$ of the calculated correction to the initial condition, i. e. $\boldsymbol{\gamma} = \boldsymbol{\gamma}_i + \kappa\delta\boldsymbol{\gamma}_{\text{projected}}$. This enlarges the radius of convergence for these special fixpoints, but also increases the number of iterations required.

Starting the above procedure with random points does not assure to find all periodic orbits in the system. The most relevant, however, are those with large amplitudes. These have a large radius of convergence, so that the probability of missing an important orbit is small. It can be further reduced by following the orbits through parameter space. Thereby one can conveniently check that no orbit is missed at a bifurcation. Furthermore, orbits can frequently be classified. For the channel system, the number of reflections in the constrictions together with the symmetry of the orbit gives such a classification. Missing orbits can readily be identified in such a scheme. All this establishes no proof, but combining these three methods can assure beyond reasonable doubt that the relevant orbits have been included.

A.2 Properties of the orbits

Once the above algorithm has converged, the properties of the newly determined periodic orbit have to be calculated. For the application of the trace formula the action S, the determinant of the monodromy matrix M, the period T_0, the Maslov index μ and the velocity-velocity correlation functions $\mathcal{C}_{ij}$ have to be evaluated. In systems with discrete symmetries, also the symmetry-related degeneracies have to be known.

[4] In practical applications it is often unnecessary to calculate the normal vector of the energy surface. It is generally sufficient to include the correction to the (absolutely) smaller component of the momentum (δu or δv) directly, and to determine the second momentum component from energy conservation. This simplification has hardly any influence on the convergence properties.

A.2.1 Period, action, stability and degeneracy

The period T_0 is automatically calculated when integrating the equations of motion. The action can be integrated straight-forward using

$$S = \int_0^{T_0} \boldsymbol{p}\, d\boldsymbol{q} = \int_0^{T_0} \boldsymbol{p}\dot{\boldsymbol{q}}\, dt\ , \tag{A.10}$$

with $\boldsymbol{p} = (x, y)$ and $\boldsymbol{q} = (u, v)$.

The stability of an orbit enters the trace formula via $\mathrm{Det}(\mathrm{M} - \mathbb{1})$. The monodromy matrix M is identical to the matrizant after one period, i. e. $M = \underline{\chi}(T_0)$. The determinant is neither affected by the unitary transformation $\underline{U}$, nor by the reduction to two dimensions, since the omitted eigenvalues are 1. Therefore

$$\mathrm{Det}(\underline{\chi} - 1) \ = \ \mathrm{Det}(\widehat{\underline{\chi}} - 1) \ = \ \mathrm{Det}(\widetilde{\underline{\chi}} - 1) \ = \ 2 - \mathrm{Tr}(\widetilde{\underline{\chi}})\ , \tag{A.11}$$

so that $\mathrm{Det}(\mathrm{M} - \mathbb{1})$ can be identified with $2 - \mathrm{Tr}(\widetilde{M})$. The stability matrix $\widetilde{M}$ is given by the reduced matrizant $\widetilde{\underline{\chi}}$ at $T = T_0$. The latter is already known from the convergence procedure.

The symmetry of an orbit can be determined numerically by calculating the intersections with suitable Poincaré surfaces of section. These have to be chosen according to the possible symmetries of the orbits, i. e. the symmetries of the system. Close to a bifurcation, however, the asymmetry of an orbit can be infinitesimal small, and thus covered by the numerical inaccuracies. Due to these limitations, the degeneracy cannot be determined numerically in the vicinity of a bifurcation. The degeneracy and the Maslov index of an orbit change only at bifurcation points. Following the orbits through parameter space (see appendix A.3), these quantities can conveniently be calculated sufficiently far from a bifurcation.

The channel considered in this work exhibits three discrete symmetries: with respect to reflection at the x-axis, the y-axis and the combination of these reflections, i. e. a rotation by π. A convenient Poincaré surface is given by $y = 0$. The orbits have anyway to be calculated for varying B and s_d in order to compare with the experimental findings. Therefore choosing B and s_d to be far from bifurcations does not lead to additional numerical effort.

A.2.2 Velocity-velocity correlation function

A nice idea[5] to reduce the numerical effort calculating $\mathcal{C}_{ij}$ is to express the velocity of the periodic orbit as a Fourier sum

$$v_i(t) = \bar{v}_i + \sum_{n=1}^{\infty} \left[a_{i,n}\, \sin(nwt) \ + \ b_{i,n}\, \cos(nwt)\right]\ , \tag{A.12}$$

where $w = 2\pi/T_0$, T_0 is the period of the orbit, and i stands for either x or y. Inserting this expression in Eq. (5.7), all integrations can be performed analytically. The final result reads

$$\mathcal{C}_{ij} = \frac{T_0}{2} \sum_{n=1}^{\infty} \frac{(a_{i,n}\, a_{j,n} + b_{i,n}\, b_{j,n})/\tau_s - (a_{i,n}\, b_{j,n} - a_{j,n}\, b_{i,n})nw}{(1/\tau_s)^2 + (nw)^2}\ . \tag{A.13}$$

[5] This idea of U. Rößler was communicated by R. Onderka.

The coefficients a_n and b_n can be calculated from the integrals

$$\begin{aligned} a_{i,n} &= \frac{2}{T_0}\int_0^{T_0} v_i(t)\sin(nwt)\;dt \quad \text{and} \\ b_{i,n} &= \frac{2}{T_0}\int_0^{T_0} v_i(t)\cos(nwt)\;dt\;. \end{aligned} \tag{A.14}$$

These integrations can again be performed simultaneously with the integration of the EOM.

A convenient method to check the convergence of the Fourier sum Eq. (A.12) is given by Parseval's theorem. For this special case it reads

$$\int_0^{T_0} |v_i(t)|^2 \;=\; \frac{2}{T}\sum_{n=1}^{\infty}\left[(a_{i,n})^2+(b_{i,n})^2\right]\;. \tag{A.15}$$

In a numerical integration, where Eq. (A.12) has to be truncated, this relation allows a numerical calculation of the truncation error.

In the case of the channel system, all orbits are similar to cyclotron orbits. This leads to rapidly decaying higher harmonics. Furthermore, the first term in Eq. (A.13) can be neglected for those trajectories. This simplifies the calculation of $\mathcal{C}_{ij}$ to

$$\begin{aligned} \mathcal{C}_{xx} &\approx \frac{T_0\tau_s}{2}\sum_{n=1}^{\infty}\frac{(a_{x,n})^2+(b_{x,n})^2}{1+(nw\tau_s)^2} \quad \text{and} \\ \mathcal{C}_{xy} &\approx \frac{T_0\tau_s}{2}\sum_{n=1}^{\infty}\frac{a_{y,n}\,b_{x,n}\;+\;a_{x,n}\,b_{y,n}}{1+(nw\tau_s)^2}\;nw\tau_s\;. \end{aligned} \tag{A.16}$$

For $w\tau_s > 1$, the higher Fourier components are additionally damped by the factor $1/(nw\tau_s)$. This is fulfilled for the channel with antidots considered in chapter 7. Therefore the inclusion of the leading 5 Fourier components was sufficient.

Note that the calculation of N Fourier components leads to $4N$ additional differential equations which have to be solved simultaneously to the EOM. It is therefore indicated to calculate only $\boldsymbol{\gamma}$ and $\widetilde{M}$ while converging to a periodic orbit, and to integrate the complete system of differential equations (including the action, the stability angle and the Fourier components) only once for each (converged) orbit.

A.2.3 Maslov index

The Maslov index is a geometrical winding number [22, 66]. This property will be used in the following for its numerical evaluation. The procedure presented here is similar to the one of Eckhardt and Wintgen [25], but it is numerically more convenient. It is much easier to implement than the general method presented by Creagh and Robbins [22, 66].[6] It is, however, restricted to two dimensional systems.

[6] Their approach is presented in a version accessible to numerical calculations in Ref. [100].

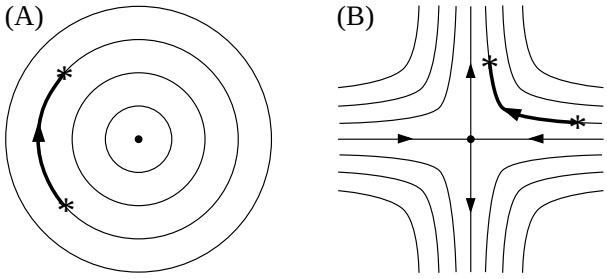

Figure A.1: *Local phase space portraits around a periodic orbit. (A) Stable, (B) unstable orbit.*

A periodic orbit is a fixpoint of the mapping of the Poincaré surface of section onto itself. The local linearization of the mapping is given by the reduced stability matrix[7]. Starting with a small deviation from the periodic orbit γ which corresponds to an eigenvector of $\widetilde{M}$, this deviation winds around γ. The total winding angle Θ is related to the Maslov index. This relation is different for the different types of fixpoints, i. e. periodic orbits. The local behavior around the fixpoint can easily be classified in dependence of the eigenvalues m_1, m_2 of the stability matrix $\widetilde{M}$:

stable orbits $\leftrightarrow |m_1| = |m_2| = 1$; Fig. A.1(A).
An orbit in the vicinity of a stable orbit remains on a ellipse around the fixpoint. All these ellipses map onto themselves. For stable orbits, the trace of the stability matrix is absolutely smaller than 2.

hyperbolically unstable orbits $\leftrightarrow m_1 = 1/m_2 > 1$; Fig. A.1(B).
Two lines in the Poincaré section map onto each other. Starting on one of these, the distance of the intersection points to the fixpoint exponentially grows ($m > 1$, outgoing manifold) or shrinks ($m < 1$, incoming manifold). Hyperbolically unstable orbits have $\mathrm{Tr}(\widetilde{M}) > 2$.

inverse hyperbolic orbits $\leftrightarrow m_1 = 1/m_2 < -1$
Equivalent to the hyperbolic case, but the intersection points change the side of the fixed point with each revolution. The trace of $\widetilde{M}$ of these orbits is smaller than -2.

For two dimensional unstable orbits the winding angle Θ is identical for all initial deviations, and a multiple of π (even multiple for the hyperbolic, and odd for the inverse hyperbolic case). This is obvious, since both the incoming manifold and the outgoing manifold map onto itself. The stability matrix is linear, so that this also holds for all linear combinations of these vectors, i. e. the whole surface of section.

For stable orbits, Θ is given by the winding angle of an eigenvector of $\widetilde{M}$. Now the winding angle is not a multiple of π, and it depends on the initial deviation. The common way to determine the winding angle is therefore to calculate first an eigenvector of $\widetilde{M}$, and to propagate this along the periodic orbit. This procedure can be simplified, so that a single integration yields Θ. This approach uses different informations about Θ, which are combined to uniquely define the winding angle.

The starting point is to write $\widetilde{M}$ as the product of a rotation and a positive definite symmetric matrix $\underline{T}$:

$$\widetilde{M} = \underline{T} \begin{pmatrix} \cos(\varphi) & \sin(\varphi) \\ -\sin(\varphi) & \cos(\varphi) \end{pmatrix} . \tag{A.17}$$

[7]Strictly speaking, the reduced (2D-) stability matrix is a mapping of the plane perpendicular to the orbit (at the initial point) and the energy surface onto itself. This distinction is, however, unimportant for the following discussion.

This is always possible, and the factorization is unique [95]. φ can easily be determined via

$$\varphi = \arctan\left(\frac{m_{12}-m_{21}}{m_{11}+m_{22}}\right) . \tag{A.18}$$

φ is a continuous function of t, and $\varphi|_{t=0} = 0$. To evaluate φ numerically, the stepsize of the differential equation solver has to be small enough so that subsequent φ differ by less than π. This condition is readily implemented in the adaptive stepsize control of the numerical integration. The correct branch $\varphi(t_n)$ can then be selected at every timestep with the knowledge of $\varphi(t_{n-1})$.

The integration of the EOM as described in Sec. A.1.4 calculates $\widetilde{\underline{\chi}}$ instead of $\widetilde{M}$. Since the local coordinate systems are identical at $t = 0$ and $t = T_0$, the winding angles in the local and the stationary system can only differ by integer multiples of 2π. The coordinate system Eq. (A.4) used above does not introduce those spurious windings [25]. Therefore, $\widetilde{\underline{\chi}}$ can be directly used to calculate φ.

Geometrically, φ describes the rotation of $\widetilde{M}$, and T a shearing. An arbitrary initial deviation is rotated by φ and sheared according to T. The shearing changes the direction of the vector by an angle α with $|\alpha| < \pi/2$. Furthermore, sign[tan(φ)]=sign[tan(Θ)]. The eigenvalues of $\widetilde{M}$ are given by $m_{1,2} = \exp(\pm i\Theta)$. This determines $|\Theta|$ modulo 2π. Combined, this information is sufficient to determine Θ uniquely. The description convenient for a numerical calculation reads

$$\begin{aligned}
\Theta &= 2\pi \cdot \mathrm{INT}\left[\frac{\varphi+\pi}{2\pi}\right] + \widetilde{\Theta}\,\mathrm{sign}\left[\mathrm{mod}_2\left(\frac{\varphi+\pi}{2\pi}\right)-1\right] , \quad \text{with} \\
\widetilde{\Theta} &= \left|\arctan\left(\frac{\sqrt{1-\left(\mathrm{Tr}(\widetilde{M})/2\right)^2}}{\mathrm{Tr}(\widetilde{M})/2}\right)\right| .
\end{aligned} \tag{A.19}$$

Here INT[x] stands for the largest integer smaller or equal to x, and mod_2 for the remainder in a division by 2.

The Maslov index is determined from the winding angle. For unstable orbits it is given by Θ in units of π

$$\mu = \Theta/\pi . \tag{A.20}$$

For stable orbits, μ is the nearest odd integer to the winding angle in units of π, i. e.

$$\mu = 1 + 2 \cdot \mathrm{NINT}\left[\frac{\Theta+\pi}{2\pi}\right] . \tag{A.21}$$

The winding angle scales with the repetition number of the orbit. The above formulas show, however, that the Maslov index only scales for unstable orbits with the repetition number. This makes the inclusion of higher repetitions of a stable orbit more complicated. Many authors therefore restrict themself to the generic case of completely chaotic systems, where all orbits are hyperbolically unstable. Having finally determined the Maslov index, all quantities needed for the evaluation of the semiclassical trace formula are known.

A.3 Following periodic orbits through parameter space

In order to calculate the semiclassical trace formula for different values of the external parameters (in the case of the channel system these are the magnetic field and the antidot diameter), it is desirable to have an algorithm which follows a specific orbit through parameter space. This can be achieved by iteratively changing marginally the parameter, followed by the convergence procedure described in Sec. A.1.4. This approach is frequently inapplicable, since (especially for very unstable orbits) the largest stepsize which still assures convergence is too small for any practical purpose. Extrapolating the initial conditions conditions to the new value of the parameter allows larger stepsizes. Note, however, that it is again necessary to ensure that the extrapolation remains on the surface of section and on the energy shell.
The choice of the extrapolation scheme is important for the performance of this approach. Linear interpolation is frequently not good enough, so that polynomial or rational function extrapolation is recommended. As pointed out in Ref. [104], extrapolations to too high orders tend to introduce spurious oscillations due to numerical inaccuracies of the data. In this work, rational function interpolation to 4th order was implemented. The starting condition in x and $\dot{x}$ was extrapolated to the new external parameter, y was fixed by the Poincaré surface of section, and $\dot{y}$ (the larger velocity component) was determined by energy conservation.

To reduce the computation time further, it is reasonable to introduce an adaptive stepsize control. The number of convergence steps needed can readily be used as a criterion for the next stepsize. The critical point is to ensure that, at the new value of the external parameter, the procedure does not converge to a different PO. For systems like the channel, where the initial conditions for many periodic orbits are close in phasespace, this requires special care. A convenient and reliable method is to check whether all orbit quantities vary smoothly. In this work, the following characteristic data of the orbits have been extrapolated to the new parameter value: Action S, stability $\mathrm{Tr}(\widetilde{M})$, period T_0 and winding angle Θ. The latter quantity is especially useful for systems with geometrically very similar orbits. The deviation of the extrapolation of these quantities to the orbit converged to was controlled, and too large deviations were rejected. In this case, a new extrapolation with reduced stepsize was started. It turned out that it is helpful to adapt the stepsize not only according to the number of iterations needed, but additionally to the extrapolated changes of the other orbit parameter. This applies especially in the vicinity of bifurcations.

This procedure works its way quickly through uninteresting terrain, slowing down where the starting conditions of the periodic orbits vary substantially. The storage requirements can be reduced by saving only those data points, where an *interpolation* of the neighboring points is worse than a tolerated error.

Furthermore it is convenient to include routines that can handle bifurcations. At the bifurcation the orbit is marginally stable, so that the convergence algorithm proposed above fails. This drawback can be overcome by first approaching the bifurcation point as close as possible. Then the initial conditions are extrapolated sufficiently far to the other side of the bifurcation, trying to converge to the orbit beyond the bifurcation. This procedure was implemented for period doubling bifurcations.

Appendix B

Numerical uniform approximation

The uniform approximation as presented by Schomerus and Sieber [70, 73] requires knowledge about the properties of the ghost orbits. This information is not available in a numerical calculation. Therefore it is desirable to develop a modified approach which only needs data that can be accessed numerically.

The derivation of Sieber and Schomerus starts from the normal form of the bifurcation. They express their parameters in terms of the quantities which enter the Gutzwiller trace formula. On the side of the bifurcations where all orbits are real, their formulas can directly be evaluated numerically. In the following, a technique for a numerical access to the complex side is presented. It consists of a fit of the parameters of the local form. The normal form is then extrapolated to the complex regime in a way that ensures the correct limiting behavior far from the bifurcation. This makes the numerical approach uniform in the sense that both the local behavior at the bifurcation and the Gutzwiller limit are reproduced correctly.

This procedure is derived for the two types of bifurcations occurring in the cannel system, namely the tangent (or isochronous) and the period doubling (or pitchfork) bifurcation.

B.1 Tangent bifurcation

The normal form of the tangent bifurcation implies the following local behavior of the action[1] S and the amplitudes A of the two orbits engaged in the bifurcation [70]:

$$\begin{aligned} S_{1,2} &= S_0 \mp \frac{2\varepsilon}{3}\sqrt{-\frac{\varepsilon}{3a}} - \frac{b\varepsilon^2}{9a^2}\,, \\ A_{1,2} &= \frac{1}{|12a\varepsilon|^{1/4}}\left(A_0 \mp \gamma\sqrt{-\frac{\varepsilon}{3a}}\right)\,. \end{aligned} \tag{B.1}$$

Considering the level density, A_0 is given by the period T_0 of the orbit; in case of the conductance, A_0 is the velocity-velocity correlation function (see Eqs. (2.14) and (5.4)). ε is the parameter which is varied across the bifurcation. It is zero at the bifurcation

[1] For a simple notation, the actions are given in units of $\hbar$ in this appendix.

itself and negative on the real side (i. e. the side of the bifurcation where the orbits exist classically). It will be convenient to define the quantities

$$\begin{aligned} \bar{A} &:= \frac{A_1 + A_2}{2A_0} \; ; \qquad \Delta A := \frac{A_1 - A_2}{2A_0} \; ; \\ \bar{S} &:= \frac{S_1 + S_2}{2} \; ; \qquad \Delta S := \frac{S_1 - S_2}{2} \; . \end{aligned} \tag{B.2}$$

Using that S_0 generically has a dominant linear dependence on ε, the local behavior at the bifurcation according to Eq. (B.1) can be written as

$$\begin{aligned} |\bar{A}|^{-4} &= \alpha_1 |\varepsilon| \; ; & |\Delta A|^4 &= \alpha_2 |\varepsilon| \; ; \\ \bar{S} &= \bar{S}_0 + \alpha_4 \varepsilon \; ; & |\Delta S|^{2/3} &= \alpha_3 |\varepsilon| \; . \end{aligned} \tag{B.3}$$

For ΔA the higher-order terms in ε stemming from a variation of γ are neglected here. Either of the first three relations can be used to define the mapping between ε and the physical quantity varied across the bifurcation (which is the magnetic field B in the present system). This mapping has to be extrapolated to the complex region. For the system considered in this work, the linear term of this mapping strongly dominates, so that higher-order contributions could be neglected. This approximation is equivalent to the ansatz

$$\varepsilon = \beta (B - B_{\mathrm{bif}}) \; . \tag{B.4}$$

The linear relations Eqs. (B.3) together with Eq. (B.4) allow to determine the parameters α_{1-4}, $\bar{S}_0$ and B_{bif} using straight-line fits.[2] This is numerically more convenient than using the original expressions Eqs. (B.1). Data points close to the bifurcations have a limited numerical accuracy, since it is difficult to converge to a marginally stable orbit (there the technique using the stability matrix fails due to vanishing first derivatives). Far from the bifurcation, the leading-order approximations of Eq. (B.1) no longer hold. So prior to the fit of the parameters of the local normal form, the fit region has to be adapted. Straight-line fits are numerically very stable and can be used both for the determination of the optimal fit region and for the fit of the parameter themselves. The upper as well as the lower limit of the fit-range were chosen for a minimal error in the slopes.

Eqs. (B.3) give only the absolute values for $\bar{A}, \Delta A$ and ΔS. The signs of these quantities can be omitted if the following factors are introduced:

$$\sigma_1 := \mathrm{sign}(\Delta S) \; ; \qquad \sigma_2 := \mathrm{sign}(\Delta A) \; . \tag{B.5}$$

These are readily calculated on the real side of the bifurcation.

The Maslov index of the bifurcation is given by the average of the Maslov indices of the two orbits involved

$$\mu = (\mu_1 + \mu_1)/2 \; . \tag{B.6}$$

[2] The parameters are actually over-determined by Eqs. (B.3), since B_{bif} can be extracted from either of the three first equations. This gives a convenient additional error control.

In these quantities the uniform approximation for the tangent bifurcation reads [70]

$$\delta = \sqrt{\frac{2\pi}{3}|\Delta S|} \times \Bigg[|\bar{A}| \left\{ J_{-1/3}(|\Delta S|) + J_{1/3}(|\Delta S|) \right\} \cos\left(\bar{S} - \mu\frac{\pi}{2}\right) \\ -\sigma_1\sigma_2 |\Delta A| \left\{ J_{-2/3}(|\Delta S|) - J_{2/3}(|\Delta S|) \right\} \cos\left(\bar{S} - (\mu-1)\frac{\pi}{2}\right) \Bigg] \tag{B.7}$$

on the real side, and

$$\delta = \sqrt{\frac{2}{\pi}|\Delta S|} \times \Bigg[|\bar{A}| K_{1/3}(|\Delta S|) \cos\left(\bar{S} - \mu\frac{\pi}{2}\right) \\ -\sigma |\Delta A| K_{2/3}(|\Delta S|) \cos\left(\bar{S} - (\mu-1)\frac{\pi}{2}\right) \Bigg] \tag{B.8}$$

on the complex side. All prefactors (including the degeneracy) have been absorbed in the amplitudes A_i, so that the formulas are valid both for the level density and the conductance and also for systems with continuous symmetries.

On the real side far from the bifurcation, the uniform approximation Eq. (B.7) can, as already pointed out, be implemented directly in a numerical calculation. In this region, $\bar{A}$, ΔA, $\bar{S}$ and ΔS can be determined from the properties of the classical orbits, using the definitions Eqs. (B.2). Close to the bifurcation the numerical evaluation of ΔA fails, since the amplitudes diverge at this point. There, however, Eqs. (B.3) (with the parameters adapted as described above) yield the correct local behavior. This local form also holds for the complex side of the bifurcation. Since ΔS increases like $\varepsilon^{3/2}$, the contribution on the complex side according to Eq. (B.8) goes to zero. This ensures that the numerical extrapolation reproduces the correct Gutzwiller limit on the complex side. The only difference to the analytic uniform approximation is the intermediate complex regime. There, however, the contributions are strongly suppressed, so that the deviation is small.

The crossover between the local normal form and the direct orbit data is preferably implemented by a a linear interpolation between these two descriptions. Choosing for this crossover approximately half the region used for the parameter fit above, the crossover is smooth. This is simply because the two methods are by construction well adapted in this regime.

The results are depicted for a typical tangent bifurcation of the channel system in Fig. B.1. The action is scaled by a factor of 10 for clarity. The solid lines in the insets show the local behavior of the quantities of Eqs. (B.3). The corresponding linear fit[3] is indicated by the dashed line. The main graph shows the Gutzwiller result (thin) and the numerical uniform approximation (heavy), which reproduces the Gutzwiller data far from the bifurcation. The spurious divergence is, indeed, removed, and decaying contributions from ghost orbits are included.

[3]The plotted range in B is approximately 5 times the optimal fit region, so that the nonlinearities can clearly be seen.

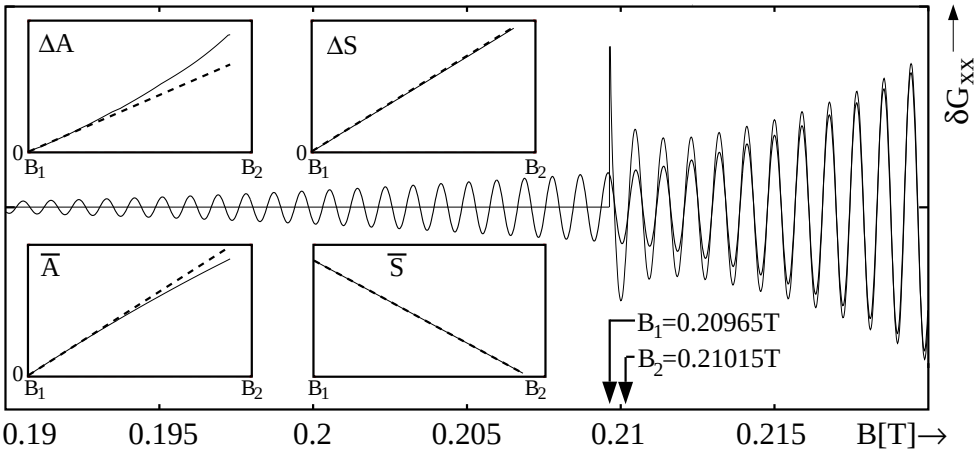

Figure B.1: *The tangent bifurcation of Fig. 4.4, with action scaled by a factor of 10. Thin: Gutzwiller result, heavy: numerical uniform result. The insets show the behavior of the quantities of Eqs. (B.3) (solid) and their linear fit (dashed).*

B.2 Pitchfork bifurcation

The normal form of the period-doubling bifurcation implies the following local behavior:

$$\begin{aligned} S_1 &= S_0 + \frac{\varepsilon^2}{4a}\left(1 + \frac{c\varepsilon}{2}\right) \\ \mathrm{Tr}_0 := \mathrm{Tr}(\mathrm{M}_0) &= 2 - 2\sigma\varepsilon \\ \mathrm{Tr}_1 := \mathrm{Tr}(\mathrm{M}_1) &= 2 + 4\sigma\varepsilon - 3c\sigma\varepsilon^2 \ . \end{aligned} \tag{B.9}$$

Here (and in the following) the subscript 0 denotes the central orbit, and the subscript 1 the two orbits[4] that split off at the bifurcation. In contrast to the tangent bifurcation discussed above, here the central orbit is real on both sides of the bifurcation. Therefore the mapping between ε (the parameter of the normal form driving the system through the bifurcation) and B (the physical parameter varied across the bifurcation) can be left implicit by substituting ε with $\sigma(1 - \mathrm{Tr}_0/2)$.

It is again necessary to carefully adapt the fit ranges, since both close to and far from the bifurcation the errors increase. Therefore the parameters are again determined using suitable linear relations. The absolute value of the parameter c is readily fitted by

$$\sqrt{6 - (2\mathrm{Tr}_0 + \mathrm{Tr}_1)} \ = \ \sqrt{|3c|}\,|1 - \mathrm{Tr}_0/2| \ . \tag{B.10}$$

It is convenient to define the factors σ, σ_1 and σ_2, which only contain sign informations. σ_2 is 1 on the real side (i. e. where both the central orbit and the satellites exist classically), and -1 on the complex side of the bifurcation. σ and σ_1 refer to properties of the real side of the bifurcation. σ_1 is given by the sign of $(S_1 - S_0)$, and $\sigma = \sigma_1$ if the central orbit is unstable, and $\sigma = -\sigma_1$ otherwise. The sign of c can be determined on the real side by

$$\mathrm{sign}(c) \ = \ \sigma\,\mathrm{sign}\left[6 - (2\mathrm{Tr}_0 + \mathrm{Tr}_1)\right] \ . \tag{B.11}$$

[4] This corresponds to the channel with antidots considered in this work. For generic systems without discrete symmetries, there is one satellite orbit with twice the period.

Using

$$\Delta S := \frac{S_1 - S_0}{2} = \frac{1}{8a}\left(1 - \frac{\mathrm{Tr}_0}{2}\right)^2 \left[1 + \frac{c\sigma}{2}\left(1 - \frac{\mathrm{Tr}_0}{2}\right)\right] , \tag{B.12}$$

the parameter a can be evaluated by another linear fit. The Maslov index μ in the uniform approximation is given by the Maslov index of the central orbit where it is unstable.[5] The uniform approximation for the period doubling bifurcation is most easily written down defining the amplitudes

$$A_i = \frac{k_i}{\sqrt{|\mathrm{Tr_i} - 2|}} , \tag{B.13}$$

(where the k_i contain all prefactors of the trace formula, including the degeneracy of the orbit) and their linear combinations

$$A^+ := \left(\frac{A_1}{2} + \frac{A_0}{\sqrt{2}}\right) \quad \text{and} \quad A^- := \left(\frac{A_1}{2} - \frac{A_0}{\sqrt{2}}\right) . \tag{B.14}$$

Using these quantities, the uniform approximation reads [70]

$$\begin{aligned} \delta \;=\; \sqrt{\frac{\pi}{2}|\Delta S|}\, \mathcal{R}e\Bigg[& \exp\left(i\left\{\bar{S} - \mu\frac{\pi}{2} - \sigma\frac{\pi}{4}\right\}\right) \times \\ & \Big\{ A^+ \left(\sigma_2 J_{1/4}(|\Delta S|)e^{i\sigma_1\pi/8} \;+\; J_{-1/4}(|\Delta S|)e^{-i\sigma_1\pi/8}\right) \\ & + A^- \left(\; J_{3/4}(|\Delta S|)e^{i\sigma_1 3\pi/8} + \sigma_2 J_{-3/4}(|\Delta S|)e^{-i\sigma_1 3\pi/8}\right)\Big\}\Bigg] . \end{aligned} \tag{B.15}$$

The numerical evaluation is similar to the case of the tangent bifurcation. On the side where all orbits are real, $A^+, A^-, \Delta S$ and $\bar{S}$ can be determined directly from the numerical orbit data. Near the bifurcation, where the amplitudes diverge and their near-cancellation causes numerical problems, $A^\pm$ can be approximated via

$$\begin{aligned} A^+ &= \frac{k_0}{2\sqrt{|1 - \mathrm{Tr}_0/2|}}\left(\frac{2}{\sqrt{|4 - 3c\sigma(1 - \mathrm{Tr}_0/2)|}} + 1\right) \\ A^- &= \frac{k_0}{2\sqrt{|1 - \mathrm{Tr}_0/2|}}\left(\frac{2}{\sqrt{|4 - 3c\sigma(1 - \mathrm{Tr}_0/2)|}} - 1\right) . \end{aligned} \tag{B.16}$$

Here it was used that $k_1 = 2k_0$ at the bifurcation. ΔS can directly be extrapolated with Eq. (B.12), and $\bar{S}$ via $\bar{S} := (S_0 + S_1)/2 = S_0 + \Delta S$. These formulae can also be used on the complex side in the vicinity of the bifurcation. To ensure the correct Gutzwiller limit on that side, the numerically determined properties of the central orbit should be used far from the bifurcation. $\bar{S}$ and ΔS can be calculated as above, and the ghost amplitude is extrapolated by

$$A_1 \;=\; \frac{2k_0}{\sqrt{|1 - \mathrm{Tr}_0/2|}}\,\frac{1}{\sqrt{|4 - 3c\sigma(1 - \mathrm{Tr}_0/2)|}} . \tag{B.17}$$

[5] The central orbit is unstable on the real side of the bifurcation if $\sigma\sigma_1 = 1$ and on the complex side otherwise.

These approximations are only valid for $c\sigma(1 - \mathrm{Tr}_0/2) \ll 4/3$. At $c\sigma(1 - \mathrm{Tr}_0/2) = 4/3$ the local expansions of ΔS and A_1 exhibit a spurious divergence. If on the complex side $c\sigma(1 - \mathrm{Tr}_0/2) > 0$, this leads to a spurious divergence of the numerical bifurcation treatment. The limit far from the bifurcations, however, is reproduced correctly[6]. In this work, the spurious divergence therefore was simply suppressed. Again, the error introduced is tolerable, since both the local behavior at the bifurcation and the Gutzwiller limit for isolated orbits is correctly reproduced. In the intermediate complex regime, where the inclusion of the ghost orbit in the numerical approach is not exact, its contribution is suppressed with $a|1 - \mathrm{Tr}_0/2|^{-5/2}$.

The result of the numerical treatment of a period doubling bifurcation for the channel system is plotted in Fig. 4.4(b,c) of Sec. 7.4.4.2. As for the tangent bifurcation, far from the bifurcation the Gutzwiller contributions are reproduced, and the divergence at the bifurcation is removed.

[6] For $\Delta S \to \infty$ the satellite terms in Eq. (B.15) exactly cancel.

Bibliography

A. Publication list

[1] J. Blaschke, Diploma thesis,
Untersuchungen zu Theorie der periodischen Orbitale für den Fall einer Kreisscheibe im homogenen Magnetfeld,
Universität Regensburg (1995), published under
`http://www.Joachim-Blaschke.de` .

[2] S. M. Reimann, M. Brack, A. G. Magner, J. Blaschke, and M. V. N. Murthy,
Circular quantum billiard with a singular magnetic flux line,
Phys. Rev. A **53**, 39 (1996).

[3] M. Brack, J. Blaschke, S. C. Creagh, A. G. Magner, P. Meier, and S. Reimann,
On the role of classical orbits in mesoscopic electronic systems,
Z. Phys. D **40**, 276 (1997).

[4] J. Blaschke and M. Brack,
Periodic orbit theory of a circular billiard in homogeneous magnetic fields,
Phys. Rev. A **56**, 182 (1997).

[5] J. Blaschke and M. Brack,
Quantum corrections to the semiclassical level density of the circular disk in homogeneous magnetic fields,
Physica E **1**, 288 (1997).

[6] J. Blaschke and M. Brack,
Classical orbit bifurcation and quantum interference in mesoscopic magnetoconductance,
preprint cond-mat/9906387 (1999).

[7] J. Blaschke, in preparation.

B. Articles and letters

[8] A. M. Ozorio de Almeida and J. H. Hannay, J. Phys. A **20**, 5873 (1987).

[9] T. Ando, J. Phys. Soc. Japan **37**, 1233 (1974).

[10] K. Arita, A. Sugita, and K. Matsuyanagi, Prog. Theor. Phys. (Japan) **100**, 1223 (1998), and earlier Refs. quoted therein.

[11] R. Balian and C. Bloch, Ann. Phys. (N.Y) **69**, 76 (1972); **85**, 514 (1974).

[12] H. U. Baranger and A. D. Stone, Phys. Rev. B **40**, 8169 (1989).

[13] M. V. Berry and M. Tabor, Proc. R. Soc. London, Ser. A. **349**, 101 (1976); **356**, 375 (1977).

[14] M. V. Berry and K. T. Mount, Rep. Prog. Phys. **35**, 315 (1972).

[15] E. N. Bogachek and G. A. Gogadze, Zh. Eksp. Teor. Fiz. **63**, 1839 (1973) [Sov. Phys. JETP **36**, 973 (1973)].

[16] E. B. Bogomolny, Nonlinearity **5**, 805 (1992).

[17] M. Brack and P. Quentin, Nucl. Phys. A **361**, 35 (1981).

[18] M. Brack and S. R. Jain, Phys. Rev. A **51**, 3462 (1995).

[19] M. Brack, S. M. Reimann, and M. Sieber, Phys. Rev. Lett **79**, 1817 (1997).

[20] M. L. Brillouin, J. phys. radium **6**, 353 (1926).

[21] M. Büttiker, Phys. Rev. Lett **57**, 1761 (1986).

[22] S. C. Creagh, J. M. Robbins, and R. G. Littlejohn, Phys. Rev. A **42**, 1907 (1990).

[23] S. C. Creagh and R. G. Littlejohn, Phys. Rev. A **44**, 836 (1990); J. Phys. A **25**, 1643 (1991).

[24] D. Darnhofer, M. Suhrke, and U. Rößler, Europhys. Lett. **35**, 591 (1993).

[25] B.Eckhardt and D. Wintgen, J. Phys. A **24**, 4335 (1991).

[26] W. Ekardt, Phys. Rev. Lett. **52**, 1925 (1984); Phys. Rev. B **29**, 1558 (1984).

[27] J. Eroms *et al.*, Physica B **256**, 409 (1998); Phys. Rev. B **59**, R7829 (1999).

[28] G. S. Ezra *et al.*, J. Phys. B **17**, L413 (1991); D. Wintgen, K. Richter, and G. Tanner, Chaos **2**, 19 (1992).

[29] H. Friedrich and J. Trost, Phys. Rev. Lett. **76**, 4869 (1996), Phys. Rev. A **54**, 1136 (1996), Phys. Rev. A **59**, 1683 (1999); J. Trost and H. Friedrich, Physics. Lett. A **228**, 127 (1997).

[30] P. Gaspard and D. Alonso, Phys. Rev. A **47**, R3468.

[31] F. Geerinckx, M. Peeters, and J. T. Devreese, J. Appl. Phys. **68**, 3435 (1990).

[32] O. Genzken and M. Brack, Phys. Rev. Lett. **67**, 3286 (1991).

[33] C. Gould *et al.*, Phys. Rev. B **51**, 11213 (1995).

[34] C. Gould *et al.*, Can. J. Phys. **74**, S207 (1996).

[35] C. Gould *et al.*, Phys. Rev. Lett. **77**, 5272 (1996).

[36] M. C. Gutzwiller, J. Math. Phys **8**, 1979 (1967).

[37] M. C. Gutzwiller, J. Math. Phys **10**, 1004 (1969).

[38] M. C. Gutzwiller, J. Math. Phys **11**, 1791 (1970).

[39] M. C. Gutzwiller, J. Math. Phys **12**, 343 (1971).

[40] M. C. Gutzwiller, J. Math. Phys **14**, 139 (1973).

[41] G. Hackenbroich and F. von Oppen, Europhys. Lett. **29**, 151 (1995).

[42] G. Hackenbroich and F. von Oppen, Z. Phys. B. **97**, 157 (1995).

[43] F. J. Harris, Proceedings of the IEEE **66**, 51 (1978).

[44] A. Isihara and K. Ebina, J. Phys. C **21**, L1079 (1988).

[45] J. B. Keller, Ann. of Phys. **4**, 180 (1958).

[46] J. B. Keller and S. I. Rubinov, Ann. of Phys. **9**,24 (1960).

[47] G. Kirczenow *et al.*, Phys. Rev. Lett. **72**, 2069 (1994).

[48] G. Kirczenow *et al.*, Phys. Rev. B **56**, 7503 (1997).

[49] S. Klama and U. Rößler, Ann. Phys. (Leipzig) **1**, 460 (1992).

[50] W. D. Knight *et al.*, Phys. Rev. Lett. **52**, 2141 (1984).

[51] H. A. Kramers, Zeits. f. Physik **39**, 828 (1926).

[52] B. Hüpper, J. Main, G. Wunner, Phys. Rev. Lett. **74**, 2650 (1995); Phys. Rev. A **53**, 744 (1996).

[53] M. Kus, F. Haake, and D. Delande, Phys. Rev. Lett. **71**, 2167 (1993).

[54] R. Landauer, IBM J. Res. Dev. **1**, 223 (1957); **32**, 306 (1988).

[55] A. Lorke and J. P. Kotthaus, Phys. Rev. B **44**, 4447 (1991).

[56] E. Madelung, Z. Phys. **40**, 322 (1926).

[57] A. G. Magner *et al.*, Prog. Theor. Phys. (Japan) (1999), submitted.

[58] B. Mehlig and K. Richter, Phys. Rev. Lett. **80**, 1936 (1998).

[59] P. Meier, M. Brack, and S. C. Creagh, Z. Phys. D **41**, 281 (1997).

[60] A. D. Mirlin and P. Wölfle, Phys. Rev. B **58**, 12986 (1998).

[61] H. Nishioka, K. Hansen, and B. R. Mottelson, Phys. Rev. B **42**, 9377 (1990).

[62] S. M. Reimann, M. Persson, P. E. Lindelof, and M. Brack, Z. Phys. B **101**, 377 (1996).

[63] K. Richter, Europhys. Lett. **29**, 7 (1995).

[64] K. Richter, D. Ullmo, and R. A. Jalabert, J. Math. Phys. **37**, 5087 (1996).

[65] K. Richter, D. Ullmo, and R. A. Jalabert, Phys. Rev. B **54**, R5219 (1996).

[66] J. Robbins, Chaos **2**, 145 (1992).

[67] A. Sachrajda, Physica E **1**, 248 (1997).

[68] S. D. Sarma and F. Stern, Phys. Rev. B **32**, 8442 (1988).

[69] H. Schomerus, Europhys. Lett. **38**, 423 (1997).

[70] H. Schomerus and M.Sieber, J. Phys. A **30**, 4537 (1997).

[71] H. Schomerus, J. Phys. A **31**, 4167 (1998).

[72] M. Sieber, J. Phys. A. **29**, 4715 (1996).

[73] M. Sieber and H. Schomerus, J. Phys. A. **31**, 165 (1998).

[74] A. M. Song *et al.*, Superlattices and Microstructures **25**, 269 (1999).

[75] P. Středa, J. Phys. C **15**, L717 (1982).

[76] V. M. Strutinsky, Nukleonik **20**, 679 (1975); A. M. Strutinsky and A. G. Magner, Elem. Part. & Nucl. (Atomizdat, Moscow) **7**, 365 (1976) [Sov. J. Part. Nucl. **7**, 138 (1976)].

[77] K. Tanaka, S. C. Creagh, and M. Brack, Phys. Rev. B **53**, 16050 (1996).

[78] K. Tanaka, Ann. Phys. **268**, 31 (1998).

[79] B. Tatievski, P. Stampfli, and K. H. Bennemann, Comput. Mater. Sci. **2**, 459 (1994); B. Tatievski, Diplomarbeit, Freie Universität Berlin, (1993) (unpublished).

[80] N. Trivedi and D. A. Browne, Phys. Rev. B **38**, 9581 (1988).

[81] D. Ullmo, K. Richter, and R. A. Jalabert, Phys. Rev. Lett. **74**, 383 (1995).

[82] D. Ullmo, K. Richter, and R. A. Jalabert, Phys. Rep. **276**, 1 (1996).

[83] D. Weiss *et al.*, Phys. Rev. Lett. **66**, 2790 (1991).

[84] D. Weiss *et al.*, Phys. Rev. Lett. **70**, 4118 (1993).

[85] G. Wentzel, Zeits. f. Physik **38**, 518 (1926).

[86] J. H. Van Vleck, Proc. Natl. Acad. Sci. USA **14**, 178 (1928).

C. Reviews

[87] T. Ando, A. B. Fowler, and F. Stern, Rev. Mod. Phys. **54**, 437 (1982).

[88] G. Bergmann, Phys. Rep. **107**, 1 (1984).

[89] M. Brack, Rev. Mod. Phys. **65**, 677 (1993).

[90] S. Chakravarty and A. Schmid, Phys. Rep. **140**, 193 (1986).

[91] T. Dittrich, Phys. Rep. **271**, 267 (1996).

[92] H. Friedrich and D. Wintgen, Phys. Rep. **183**, 37 (1992).

[93] B. Kramer and A. MacKinnon, Rep. Prog, Phys. **56**, 1469 (1993).

[94] P. A. Lee and T. V. Ramakrishnan, Rev. Mod. Phys **27**, 287 (1985).

[95] R. G. Littlejohn, Phys. Rep. **138**, 193 (1986).

[96] K. Richter, D. Ullmo, and R. A. Jalabert, Phys. Rep. **276**, 1 (1996).

D. Books

[97] A. A. Abrikosov *et al.*, *Methods of Quantum Field Theory in Statistical Physics*, Prentice-Hall, Englewood Clifs (1963).

[98] H. P. Baltes and E. R. Hilf, *Spectra of Finite Systems* (Bibliographisches Institut, Mannheim, 1972).

[99] C. W. J. Beenakker and H. van Houten, *Quantum transport in semiconductor nanostructures* (Solid state physics **44**), Academic press 1991.

[100] M. Brack and R. K. Bhaduri, *Semiclassical Physics*, (Frontiers in Physics, Vol. 96) Addison Wesley 1997.

[101] P. Citanović *et al.*, *Classical and quantum chaos: A Cyclist Treatise*, published under `http://www.nbi.dk/ChaosBook`.

[102] H. Geiger, *Quantenmechanik ohne Paradoxa: Meßprozeß und Chaos aus der Sicht der Bohmschen Quantenmechanik*, Dissertation, Universität Regensburg (1997); published by Mainz, Aachen 1997.

[103] R. Kubo, M. Toda and N. Hashitsume, *Statistical Physics II* (Springer, Berlin, 1985).

[104] W. H. Press *et al.*, *Numerical Recipes in Fortran : The Art of Scientific Computing; (Fortran Numerical Recipes, Vol 1 and 2)*, Cambridge University Press (1992).

[105] K. Richter, *Semiclassical Theory of Mesoscopic Quantum Systems*, Habilitation Thesis Universität Augsburg (1997), Springer, Berlin (in print).

[106] U. Smilansky in *Mesoscopic Quantum Physics*, edited by E. Akkermans*et al.*, Elsevier, New York (1995).

[107] J. Stoer and R. Bulirsch, *Introduction to numerical analysis*, Springer (New York, 1980).

E. Literature to specific topics

[108] For a possible solution to the chirality problem using a logarithmic extension of the Schrödinger equation see, e. g., I. Bialynicki-Birula and J. Mycielsky, Ann. Phys. **100**, 62 (1976), and the references cited therein.

[109] For another than the Kopenhagen interpretation of quantum mechanics see, e. g., D. Bohm and B. Hiley, Found. Phys. **14**, 255 (1984), and the references cited therein.

[110] For experimental evidence of coulomb ordering see, e. g., E. Buks, M. Heiblum, and H. Shtrikman, Phys. Rev. B **49**, 14790 (1994); P. Sobkowicz, Z. Wilamowski, and J. Knossut, Semicond. Sci. Technol. **7**, 1155 (1992).

[111] For resummation schemes for trace formulae see contributions in Chaos **2**, (1992).

[112] For the discussion on including finite temperature in transport linear response see, e. g., G. Czycholl and B. Kramer, Solid state Commun. **32**, 945 (1979); Y. Imry and N. S. Shrien, Phys. Ref. B **33**, 7992 (1986); D. J. Thouless and S. Kirkpatrick, J. Phys. C **14**, 235 (1981).

[113] For theoretical work on coulomb ordering see, e. g., A. L. Efros, Solid State Comm. **65**; T. Suski *et al.*, Phys. Rev. B **50**, 2723 (1994); M. Stopa, Phys. Rev. B **54**, 13767 (1996), Superlattices and Microstructures **21**, 493 (1997).

[114] For recent semiclassical approaches to the resonant tunneling diode see, e. g., E. E. Narimanov, A. D. Stone, and G. S. Boebinger, Phys. Rev. Lett. **80**, 4024 (1998); D. S. Sarga and T. S. Monteiro, Phys. Rev. E **57**, 5252 (1998); T. S. Monteiro *et al.*, Phys. Rev. B **56**, 3913 (1997); E. B. Bogomolny and D. C. Rouben, Europhys. Lett. **43**, 111 (1998); and the references cited therein.

[115] For an explanation of the stable classical chirality using a coupling to the radiation field see P. Pfeifer, *Chiral molecules – a superselection rule induced by the radiation field*, dissertation Zürich (1980).

[116] For works related with the consistent interpretation of the quantum measurement process see, e. g. H. Primas: *The measurement process in the individual interpretation of quantum mechanics* in *Quantum theory without reduction*, Adam Hilder, Bristol (1990); R. Omnès, Rev. Mod. Phys. **64**, 339 (1992).

[117] For an overwiew on nuclear shapes and shell see, e. g., I. Ragnarsson, S. G. Nilsson, and R. K. Sheline, Phys. Rep. **45**, 1 (1978).

F. Miscellaneous

[118] M. Brack *et al.*, in preparation.

[119] See, e. g., the example of the triangular billiard in Sect. 6.1.2. of Ref. [100].

[120] B. Mehlig and K. Richter, in preparation (1998).

[121] P. Meier, Diploma thesis, Universität Regensburg (1995) (unpublished).

[122] P. Meier, Dissertation, Universität Regensburg (1999) (unpublished).

[123] F. von Oppen, Dissertation, University of Washington (1993) (unpublished).

[124] S. Pedersen *et al.*, cond-mat/9905033 (1999).

[125] D. Weiss, private communication.

An Euch,

Der Arbeitsgruppe. Es hat nicht nur Spaß gemacht, mit Euch zu arbeiten, sondern auch mit Euch nicht nur zu arbeiten!

Matthias, meinem Doktorvater. Für Forderung und Förderung. Und für seine Begeisterung, die mich immer wieder angesteckt hat.

Stephan. Für seine Neugierde und seine ansteckend klare Art zu denken. Außerdem soll er gefälligst Professor werden ...

Meinen Eltern.

Fritz, Tom und Marc, die mir bei meinen Kämpfen gegen die Windmühlen der EDV immer wieder in den Sattel geholfen haben.

Didi, Caren, Anna und Joscha. Bonsoir, mes amis ...

Anja. Für körperliche, geistige und seelische Rückendeckung.

ein dickes

Floh und Burkhard von der Chaostruppe. Für physikalische und ausserphysikalische Begleitung.

K. Richter, S. Creagh, H. Schomerus, M. Sieber, K. Tanaka, J. Eroms, S. Jobst, O. Steffens, U. Rößler und M. Suhrke, die sich Zeit genommen haben, meine Fragen zu beantworten.

J. Eroms and S. Pedersen for handing out experimental data.

G. Kirczenow for the quantum data of the channel.

Anja, Didi und Stephan für die Durchsicht des Manuskriptes.

A. Sachrajda, C. Gould and P. J. Kelly from the Institute of Microstructural sciences, Ottawa. Not only for providing me with the experimental data of the channel system, but also for their continued interest in this work and for their patience explaining experimental details to a theoretist.

Heather, Sven, Merideth and Monika. I apologize for torturing you with all this physics (not to mention my very special interpretation of English grammar).

Dankeschön!

This work was very much stimulated by the discussion with other workers in the field. In addition to the contacts mentioned on the last page, many informal conversations had been helpful for the research presented here. Especially the conferences and workshops which I had the possibility to attend and where I could present parts of this work, gave rise to plenty of these valuable opportunities. In this context, I greatfully acknowledge the financial support of the Universität Regensburg and the grant CHRX-CT94-0612 of the European Community. I am additionally indebted to the Niels Bohr Institute, Copenhagen, the Université Paris Sud and the Max Planck Institut "Physik komplexer Systeme", Dresden for their kind invitations.

ANNOUNCEMENT

Part of the work started out in the context of this thesis did not reach maturity. Some of these projects were just too low on the priority list to get finished within the limited time of my Ph.D. Among these, there is quite some pioneering work on the Aharonov-Bohm ring experiment mentioned above [124], including a first numerical estimation of the depletion width. Another project aimed for a semiclassical calculation of the potential steepness of an antidot lattice. For this project, I already performed analytical calculations for the shortest orbits of the corresponding billiard system. The next step would be to include finite slopes within semiclassical perturbation theory. Comparing the results to measured data might allow a statement on the smoothness of the physical potential. This analysis should also be applicable to the experiment on antidot lattices with large antidots performed in the group of D. Weiss [27]. Furthermore, I worked on classical conductivities of inhomogeneous system. Special focus was directed on rectangular antidot lattices. First numerical and analytical results indicate that there is interesting physics to reveal, namely that there might be an classical effect leading to anisotropic conductivities in these systems.

I really liked these projects, and I really like to see them finished. If someone else is attracted to any of these problems, he is seriously invited to contact me:

`mail@joachim-blaschke.de`

I will be happy to communicate my preliminary findings as a starting point for further investigations to anyone who is interested in the related questions.

. . . and trust me on the sunscreen.